TRANSPORT AND OPTICAL CHARACTERISTICS OF GRAPHENE-BASED HYBRID STRUCTURE AND TWO-DIMENSIONAL LAYERED GALLIUM SELENIDE

JIE Wenjing

Ph.D

The Hong Kong Polytechnic University

2015

The Hong Kong Polytechnic University
Department of Applied Physics

Transport and Optical Characteristics of Graphene-Based Hybrid Structure and Two-Dimensional Layered Gallium Selenide

JIE Wenjing

A thesis submitted in partial fulfillment of the requirements for
the degree of Doctor of Philosophy

October 2014

CERTIFICATE OF ORIGINALITY

I hereby declare that this thesis is my own work and that, to the best of my knowledge and belief, it reproduces no material previously published or written, nor material that has been accepted for the award of any other degree or diploma, except where due acknowledgement has been made in the text.

____(Signed)

__________________JIE Wenjing_____________________ (Name of student)

Abstract

Due to its unique two-dimensional (2D) structure and fascinating properties, graphene has revealed potential applications in many aspects since it was first discovered by a micro-mechanical exfoliation method. Beyond graphene, a big family of 2D materials has been discovered subsequently. Their potential has been developed from basic electronic and optoelectronic devices to a wide range of applications. Among them, 2D GaSe, as a recently discovered 2D material, has received lifted attention and been studied extensively in the matter of fabrication techniques and potential applications. Therefore, it is important to investigate the fundamental properties of these 2D materials for further understanding and future applications of them.

In this thesis, firstly, a non-volatile memory can be fabricated by integrating graphene with ferroelectric [$Pb(Mg_{1/3}Nb_{2/3})O_3$]-[$PbTiO_3$] (PMN-PT) based on a field effect transistor (FET) structure. The fabricated FET exhibited p-type characteristics with a large memory window. By pre-poling the PMN-PT substrate, a reduction in p-doping of the FET can be achieved. On the other hand, it should be noted the fact that ferroelectric materials are capable of producing controllable biaxial strain due to the piezoelectric effects. Such tunable strain can result in a blue shift in 2D band of graphene. And more interesting, a continuous 2D band shift can be detected during the retention of a bias voltage. Secondly, graphene/Si Schottky junction solar cells have drawn much attention and been investigated extensively due to their potential applications. In comparison with Si, GaAs has the merits of high electron mobility and direct band gap. Herein, n-type GaAs has been integrated with graphene sheets to fabricate Schottky junction solar cells. The Schottky junction shows photovoltaic behaviors with a power conversion efficiency of 1.95 %. Thirdly, nonlinear optics in GaSe bulk crystals has been studied for decades, such property in its 2D counterpart is unknown and of much significance. We report a strong layer- and power-dependent second harmonic generation (SHG) at few-layer GaSe sheets. Two-photon excited fluorescence has also been observed in GaSe nanosheets. Our free energy calculations on GaSe bulk and layers based on first-principles methods support the observed nonlinear optical phenomena in the atomically thin layers.

In conclutions, the electronic and optoelectric characteristics of graphene have been investigated by integrating graphene with functional materials of ferroelectric and semeconductor, followed by a study of the nonlinear optical properties of 2D GaSe flakes. These fundamental studies will aid further research of 2D materials and show promise for their future applications in nanoelectronics and nanophotonics.

List of Publications

1. **Wenjing Jie**, Xi Chen, Dian Li, Lu Xie, Yeung Yu Hui, Shu Ping Lau, Xiaodong Cui, Jianhua Hao, "Layer-Dependent Nonlinear Optical Properties and Stability of Non-Centrosymmetric Modification in Few-Layer GaSe Sheets", ***Angew. Chem. Int. Ed.***, **2015**, 54 (4), 1185-1189**.**
2. **Wenjing Jie**, Jianhua Hao, "Graphene-based hybrid structures combined with functional materials of ferroelectrics and semiconductors", ***Nanoscale***, **2014**, 6 (12), 6346-6362.
3. **Wenjing Jie**, Fengang Zheng, Jianhua Hao, "Graphene/gallium arsenide-based Schottky junction solar cells", ***Appl. Phys. Lett***., **2013**,103, 233111.
4. **Wenjing Jie**, Yeung Yu Hui, Ngai Yui Chan, Yang Zhang, Shu Ping Lau, Jianhua Hao, "Ferroelectric polarization effects on transport of graphene/PMN-PT field effect transistors", ***J. Phys. Chem. C***, **2013**, 117, 13747–52.
5. **Wenjing Jie**, Yeung Yu Hui, Yang Zhang, Shu Ping Lau, Jianhua Hao, "Effects of controllable biaxial strain on the Raman spectra of CVD-grown monolayer graphene", ***Appl. Phys. Lett.***, **2013**, 102, 223112.
6. Yuda Zhao, Zhaojun Liu, Tieyu Sun, Ling Zhang, **Wenjing Jie**, Xinsheng Wang, Yizhu Xie, Yuen Hong Tsang, Hui Long, Yang Chai, "Mass Transport Mechanism of Cu Species at the Metal/Dielectric Interfaces with a Graphene

Barrier", ***ACS Nano***, **2014**, 8 (12), 12601-12611.

7. Li Chen, Man Chung Wong, Gongxun Bai, **Wenjing Jie**, Jianhua Hao, "White and green light emissions of flexible polymer composites under electric field and multiple strains", ***Nano Energy***, online, **DOI**:10.1016/j.nanoen.2014.11.039.
8. Yeung Yu Hui, Xiaofei Liu, **Wenjing Jie**, Ngai Yui Chan, Jianhua Hao, Yu-Te Hsu, Lain-Jong Li, Wanlin Guo, Shu Ping Lau. "Exceptional tunability of band energy in a compressively strained trilayer MoS2 sheet" ***ACS Nano***, **2013**, 7, 7126–7131.
9. Yuda Zhao, Yizhu Xie, Yeung Yu Hui, Libin Tang, **Wenjing Jie**, Yifan Jiang, Ling Xu, Shu Ping Lau, Yang Chai. "Highly impermeable and transparent graphene as an ultra-thin protection barrier for Ag thin films" ***J. Mater. Chem. C***, **2013**, 1 (32), 4956-4961.

Acknowledgements

Firstly, I would like to express my sincere appreciation to my supervisor, Dr. Jianhua Hao. He always guides me with his profound knowledge and supports me with his great patience. He is always positive and enthusiastic to the science and research and helps me to achieve my doctorial study and make this thesis a reality.

I am grateful to Prof. Shu Ping Lau. His valuable suggestion and kind guidance are very important for me throughout this thesis work. Also, I would like to express my gratitude to Prof. Xiaodong Cui from HKU for his generous assistance in my research work. It is an honor for me to get help from Prof. Dai Jiyan, Dr. Jikang Yuan, Dr. Feng Yan, Dr. Xuming Zhang. These kind assistance and valuable suggestions have been of great help to me.

I am grateful to the stuffs who supported me in my works. I would like to thank Mr. Man Nin Yeung, Dr. Hardy Lu and Dr. Albert Choy for their assistance in facility utilization in our department. Thanks to all guys who have helped me during last three years. I would like to give my thanks to my colleagues Mr. Yeung Yu Hui for his help in FET measurement, Dr. Zhenhua Sun for his help in graphene transfer, Dr. Zhike Liu for his suggestion in solar cells fabrication and measurement, Mr. Gongxun Bai for his assistance in PL measurement, Mr. Zhibin Yang for his help in photolithograghy, Dr. Bolei Chen for his help in AFM & MFM, Mr. Ning Wang for his help in Sputtering and Mr. Xiao Wu for his assistance in PE measurement. I am also so honored to get so much help and assistance from Dr. Yang Zhang, Dr. Fengang Zheng, Mr. Ming-Kiu Tsang, Mr. Shuoguo Yuan, Mr. Yuda Zhao, Mr. Ngai Yui Chan, Dr. Jinhua Li, Dr. Lili Tao and Mr. Simon Luk. I would also like to thank Mr. Lu Xie, Ms. Xi Chen, Mr. Dian Li from HKU and Mr. Chi Fai Chan from CityU for their cooperation in our collaborative works.

Besides, I want to give my sincere thanks to Ms. Meng Zhang, Ms. Mei Lin, Ms. Li Chen, Ms. Min Guo, Ms. Yan Chen. I am really appreciated your kind help, company and encouragement during last three years in Hong Kong.

Finally from my heart, I would like to express my appreciation and love to my parents and my elder sister, who always support me. Also, I am so grateful to my husband, Dr. Xianhua Wei. It is impossible for me to complete my research works and finish this thesis smoothly without their encouragement and support.

Table of Content

List of Figures

List of Tables

Chapter 1 **Introduction**

1.1 **Background**

Two-dimensional (2D) material is a thin sheet in which one dimension is restricted in size. 2D materials are expected to possess unique physical, chemical, optical and mechanical properties due to the special structure with high surface-bulk ratio. Consequently, 2D materials are attractive from both scientific and technological viewpoints by considering their exceptional structure and fascinating properties. Graphene is a single carbon layer that consists of hexagonally arranged, sp^2-hybridized carbon atoms with a honeycomb lattice structure. Graphene was discovered via a mechanically exfoliated method by A. K. Geim et al at Manchester University in 2004.[1] Graphene is not an integral part of a carbon material, but is freely suspended or dispersed in some organic solutions, or adhered on a flat substrate which provide mechanical support to graphene.[2] There are two interpenetrating carbon atoms per unit cell, A and B, shown in red and green in the schematic of the real-space graphene lattice (Figure 1.1a).[3] The distance between the nearest neighbour carbon-carbon atoms is 1.42 Å, while the lattice parameter is the second-nearest distance. Beside such unique lattice structure, the electric structure is also special for graphene. The conduction band (red) and the valence band (blue) meet at Dirac points at the corners of the Brillouin zone (shown in orange) in momentum space, as shown in Figure 1.1b. The charge-neutrality level in undoped graphene lies at the Dirac points, corresponding to the Fermi level of graphene. Therefore, band gap of undoped graphene is zero.

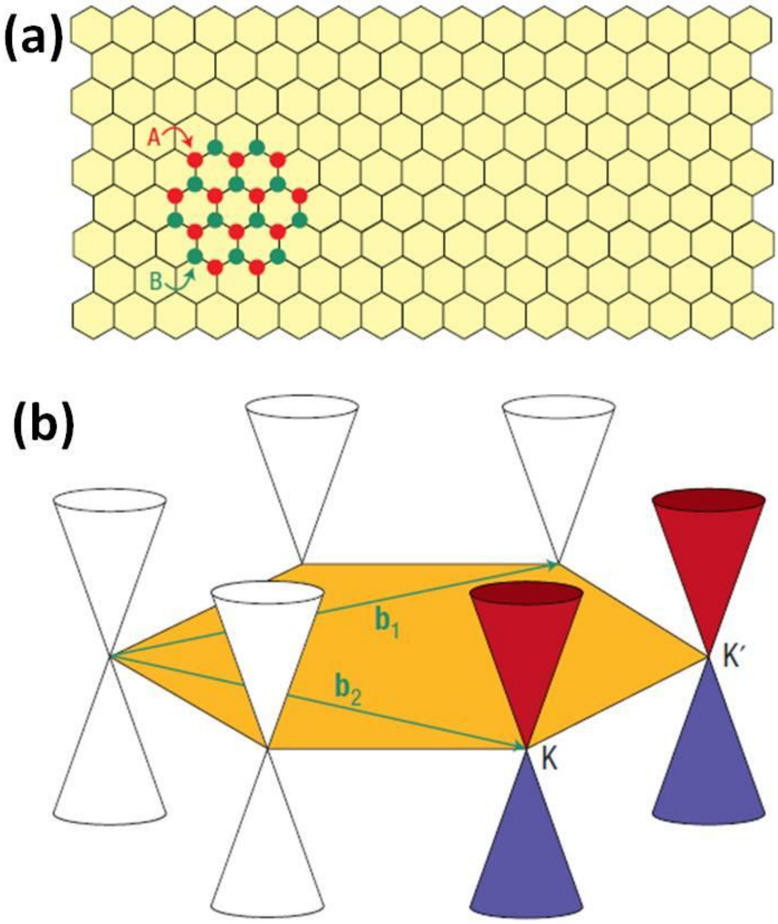

Figure 1.1 (a) Schematic of real-space graphene with honeycomb lattice structure. (b) Unique electronic structure of graphene in momentum space. The vertical axis is corresponding to energy , while the horizontal axes stand for momentum in the x and y directions.[3]

With its unique 2D-layered lattice structure and zero-bandgap electronic structure, graphene possesses novel features, especially in electronic properties. The electron energy is a linear function of momentum in single-layer graphene, whereas it is proportional to the square of the momentum in all other quasi-2D materials, including semiconductor heterostructures and bilayer graphene. This means that the electrons all move with a constant speed independent of their momentum, and behave as if they do not have any mass. The density of states vanishes even at Dirac points. Moreover, graphene's quality clearly reveals itself in a pronounced ambipolar electric field effect such that charge carriers can be tuned continuously between electrons and holes in concentrations as high as 10^{13} cm^{-2} and their mobilities can exceed 15,000 $\mathrm{cm}^2\mathrm{V}^{-1}\mathrm{s}^{-1}$, which is the ballistic transport on the sub-micrometre scale (currently up to about 0.3 μm at 300 K). The room-temperature quantum Hall effect is another extreme electronic quality which can be observed in graphene. Besides, graphene also exhibits outstanding electrical, thermal, optical, and mechanical properties.[4,5] Single-layer graphene has a large theoretical specific surface area (~2630 $\mathrm{m}^2\mathrm{g}^{-1}$),[6] and low electrical conductivity,[7,8] good impermeability (gas and liquid),[9,10] excellent thermal conductivity (~5000 $\mathrm{W}^{-1}\mathrm{K}^{-1}$),[11] low absorption in white light spectrum (~2.3%),[12] and high Young's modulus (~1.0 TPa).[13]

With its fascinating properties, graphene has accordingly been explored in a wide range of applications, such as optoelectronics, memories, sensors, supercapacitors, and so on.[14,15] In particular, field effect transistors (FETs) by integrating graphene and another insulator have been rapidly developed and show potential applications in future. Graphene-based FET (GFET) is promising to substitute silicon metal–oxide–semiconductor FET (MOSFET) in post-silicon nanoelectronics, due to its real 2D structure and extra high electron and hole mobility by considering its application in high speed FETs.[16,17] The first and also extensively-studied GFET is based on graphene/SiO_2 heterostructure which was proposed in 2004 along with the observation of graphene.[1] Utilizing the amazing properties of its one-atomic-layer thickness and ultra-high mobility (in excess of 10^5 $cm^2\ V^{-1}\ s^{-1}$ for exfoliated graphene on SiO_2 and greater than 3,700 $cm^2\ V^{-1}\ s^{-1}$ for large-area graphene grown on nickel and transferred to a substrate at room temperature) even at high carrier concentration, GFETs have drawn various attentions from all over the world. Besides, the high conductivity is also a remarkable advantage of graphene who is also flexible and transparent, making graphene a good candidate to substitute indium tin oxide (ITO) as transparent electrodes from the view points of many applications in optics, electronics and optoelectronics.

Beyond graphene, a large variety of graphene-like 2D materials can be exfoliated from their layered bulk materials like graphite. Graphene seems to be just the tip of the iceberg for 2D materials and the subsequent discovery of alternative 2D materials beyond graphene shows a big 2D family.[18,19] Indeed, the use of simple micro-mechanical cleavage technique proposed by Novoselov et al. has been expanded from graphene to other 2D layered materials, as shown in Figure 1.2.[19] Several cleaved samples of NbSe2, graphite, $Bi_2Sr_2CaCu_2O_x$, and MoS_2, corresponding to Figure 1.2 a, b, c and d, respectively, illustrate only one-atomic-layer thickness but nearly macroscopic laterally. A big family of transition metal dichalcogenides (TMDCs), consisting of hexagonal layers of transition metal atoms (M, typically Mo, W, Nb, Re, Ni, or V) and sandwiched between two layers of chalcogen atoms (X, typically S, Se, or Te)) with a MX_2 stoichiometry, show more and more 2D layered materials after that. Among them, molybdenum disulfide (MoS_2), is a typical example with exotic properties. The band gap of MoS_2 shifts from the indirect gap of 1.29 eV to direct gap of over 1.90 eV when decreasing the thickness of MoS_2 from bulk to single layer.[20] Although the mobility and stability of MoS_2 is not comparable to graphene, a desirable band gap in MoS_2 and other TMDCs still attract much attention from the view of science and technology. Following a roadmap of graphene, 2D layered MoS_2 has been integrated with versatile functional materials and shows much potential for the future applications in many aspects. Beside MoS_2, hexagonal GaS and GaSe have layered structures with each layer consisting of S–Ga–Ga–S and Se–Ga–Ga–Se sheets, and indirect bandgaps of 3.05 eV and 2.1 eV, respectively.[21] Both of the new 2D materials have been employed in Si integrated devices, such as FETs and photodetectors.[22–25]

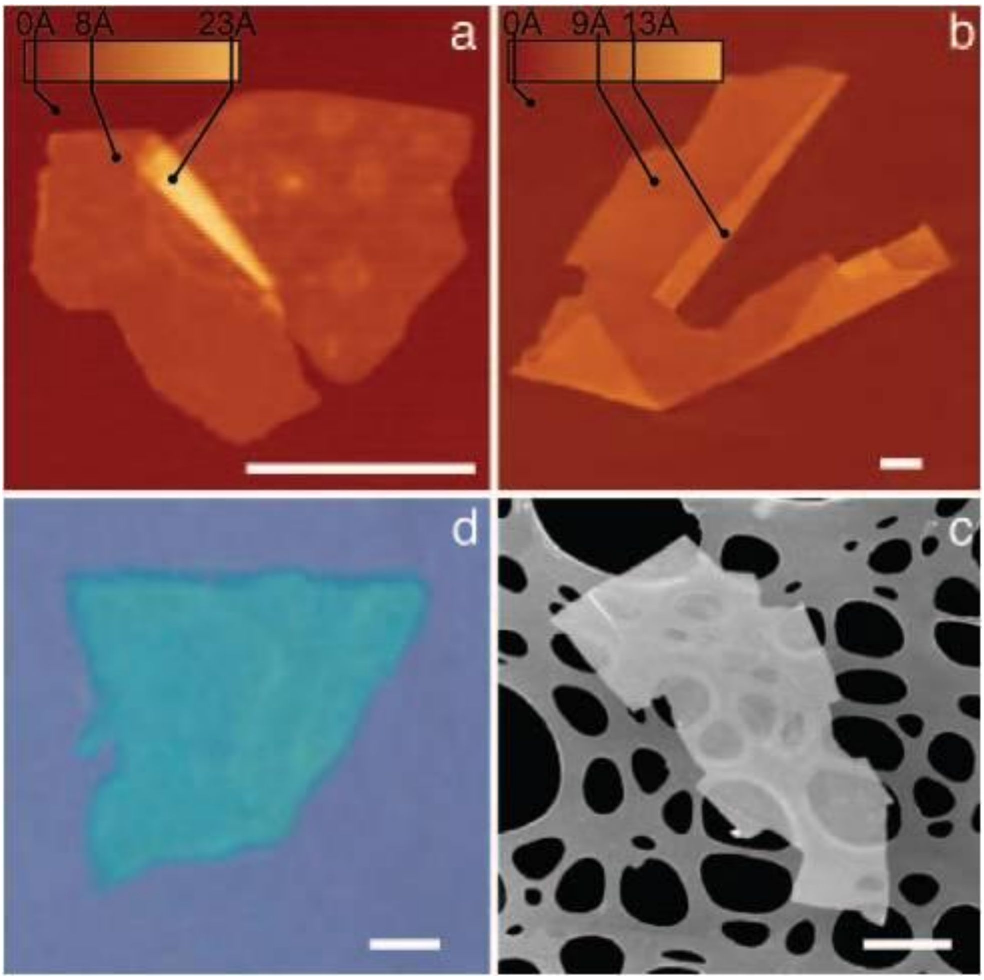

Figure 1.2 Single-layer 2D crystals. (a) $NbSe_2$, (b) graphite, (c) $Bi_2Sr_2CaCu_2O_x$, and (d) MoS_2 visualized by AFM (a and b), by scanning electron microscopy (c), and in an optical microscope (d). All scale bars: 1 μm.[19]

In addition to 2D semiconductors, it was reported that individual atomic planes of insulator of hexagonal boron nitride (*h*-BN) could be isolated from its bulk materials.[19] Anyway, after the success of exfoliation of semi-metal graphene, a wide range of 2D materials ranging from semiconductors to insulators have been discovered and show potential in future nanoelctronic and nanophotonic applications.

1.2 Significance of Research

Recently, ferroelectric materials have been employed in GFETs by using ferroelectric materials as gate insulator for memory applications.[26,27] The switchable polarization (effectively resulting in stored charge) can be utilized as the means of storing information, which offers ferroelectrics the opportunity to be as promising nonvolatile alternatives.[28,29] Thus, it is very significant to study the fascinating characteristics of graphene/ferroelectric FETs (GFeFETs).[30,31] However, large-area graphene is a gapless semi-metal, which becomes one of the major challenges when using graphene-based devices in practical applications.[17] Accordingly, various efforts have been devoted to access a tunable band gap in graphene.[32,33] Strain engineering is proposed to induce a gap in graphene, but typically large strain in excess of 20% is needed.[34,35] Nevertheless, strain engineering on graphene is very essential to study the fundamental properties of graphene. Interestingly, it should be noted the fact that ferroelectric materials also possess piezoelectric properties due to the non-central structure. For instance, $[Pb(Mg_{1/3}Nb_{2/3})O_3]$-$[PbTiO_3]$ (PMN-PT) not only exhibits attractive ferroelectric characteristics, but also possesses outstanding converse piezoelectric response. It should be noted that the strain provided by piezolelectrc effect is biaxial, that is the strain is homogeneous in x and y directions. Thus, it is feasible also essential to investigate controllable biaxial strain effects on graphene by coupling piezoelectric effect to graphene, considering a large range of studies on strain engineering are focusing on the uniaxial strain on graphene by stretching or bending the underlying flexible substrates.

Secondly, graphene and some semiconductors can form metal/semiconductor (M/S) Schottky junction in which graphene serves as active layer of metal.[36,37] Among these M/S junction, Si has been widely employed to act as the semiconductor,[38] and more importantly, the photovoltaic effects have been achieved based on the graphene/semiconductor Schottky junctions.[39] The presented technique can provide the possibility to combine large-area graphene with other semiconductors, such as GaAs.[40,41] In comparison with Si, GaAs has the merits of high electron mobility and direct band gap, allowing GaAs-based devices to function at high frequencies and be efficient in light emitting devices. Moreover, theoretical simulation shows that graphene/GaAs has a potential of exhibiting superior photovoltaic behaviors to that of graphene/Si junctions.[42] The hybrid systems of graphene and GaAs (or GaAs nanowires) exhibit the potential applications of photodetector.[43,44] Taking into account of the superb properties of high electron mobility and direct band gap, graphene/GaAs hybrid structure shows potential in solar cell applications.

Thirdly, stimulated by the success of graphene, simple micro-mechanical cleavage technique has been expanded to other layered materials.[19] Among the recent advances for potential applications of graphene and beyond graphene,[14,45–47] 2D gallium selenide (GaSe), a layered III-VI semiconductor, has been receiving lifted attention from electronic and photonic applications, such as FETs and photodetectors.[21,23,25] Note that one of the most important properties of bulk GaSe is the nonlinear optical property due to the absence of the inversion symmetric center.[48,49] Nonlinear optics has been widely used in many important applications such as integrated optics, optical information, optical communications and imaging techniques.[50,51] In comparison with their bulk counterparts, the nonlinear optical properties have not been explored in their 2D form. Thus, it is essential and interesting to study the nonlinear optical properties of 2D layered GaSe.

1.3 Structure of Thesis

The chapters of this thesis are organized as follows:

Chapter 1: Introduction. In this chapter, the unique structure and fascinating properties of graphene are first introduced, followed by the 2D materials beyond graphene. Then, the significance of this research is presented for better understanding of this research. In the meantime, the structure of this thesis is described for reading guidance.

Chapter 2: Overview of graphene-based hybrid structure and 2D layered GaSe. The first section gives the background of GFETs and GFeFETs. Then the strain effects and the vibritional properties of graphene are discussed. The second section devotes to the basic principles, research status and potential applications of graphene-based Schottky junction solar cells combined with Si and GaAs. Last but not least, the crystal structure and intrinsic properties of bulk and 2D GaSe as well as the recent progress in nonlinear behaviors of single-layer 2D materials.

Chapter 3: Experimental techniques. This chapter describes the important experimental methods which were used in works described in this thesis, including the preparation and transfer methods of graphene and GaSe nanosheets, the structural characterization techniques, the electrical characterization systems, as well as the optical characterization systems.

Chapter 4: Fabrication and Characterization of Graphene/PMN-PT Hybrid Structure. This chapter demonstrates hybrid structure of graphene and PMN-PT, ranging from the fabrication, characterization to transport and vibrational properties. Especially, the effects of ferroelectric polarization on the electric properties of graphene are summarized. Then, the vibrational properties of graphene under piezoelectric biaxial strain are discussed.

Chapter 5: Graphene/GaAs -based Schottky junction solar cells. This chapter is the experimental study of graphene/GaAs Schottky junction solar cells. The working principles of the Schottky junction are addressed and the photovoltaic effects of the junction-based solar cells are investigated.

Chapter 6: Nonlinear optical properties of 2D layered GaSe sheets. In this chapter, the second harmonic generation and two-photon excited fluorescence of the GaSe nanosheets have been studied. Besides, first-principles calculations are performed to support the unique nonlinear optical properties.

Chapter 7: Conclusion and Future Prospect. In this chapter, the results in this thesis are summarized and concluded. Meanwhile, future prospect of the research of 2D materials is described.

Chapter 2 **Overview of Graphene-Based Hybrid Structure and 2D GaSe**

In this chapter, the relevant research status, background, significance and the basic principles will be introduced for a comprehensive understanding of the thesis. Some basic information about graphene-based transistors and graphene/ferroelectric transistors are described. Based on the hybrid structure of graphene/ferroelectric, the strain effects and vibrational properties of graphene are discussed. This is followed by the analysis and discussion of graphene-based Schottky junction solar cells. Then research status of 2D GaSe and the nonlinear behaviors of single-layer 2D materials are presented.

2.1 Graphene/ferroelectric hybrid structure

2.1.1 Graphene-based transistors

Generally speaking, a FET consists of a channel region connecting source and drain electrodes, a gate and a barrier separating the gate from the channel. Typically, the operation of a transistor relies on tuning the channel conductivity. The current between the drain and the source can be accordingly controlled by a bias voltage applied between the gate and source electrodes. After its discovery, graphene has been integrated into GFET devives. There are three types of GFETs: back-gated; dual back- and top-gated; top-gated FETs, as schematically shown in Figure 2.1a, b, and c, respectively.[52] A typical back-gated GFET is fabricated by forming two electrodes of source and drain on the top of the graphene layer, with a potential applied to the highly-doped silicon bottom electrode of the device to modulate the energy levels of graphene (Figure 2.1a). A top-gated GFET can be formed by depositing an insulator layer (for example, Al_2O_3, as shown in Figure 2.1c) on graphene to serve as the gate insulator with SiC substrate to provide mechanical support to the graphene layer. While, a dual back- and top-gated GFET, showing the localized gate capacitor fabricated on top of the channel, as shown in Figure 2.1b. Electron and hole densities are tuned by a gate voltage, which raises or lowers the Fermi energy of graphene, shown schematically in Figure 2.1d. At the charge neutrality (Dirac) point, K and K ́, the resistivity (conductivity) reaches a maximum (minimum), and the conductivity increases above or below this energy point. This zero-bandgap material has an insufficient maximum resistance (i.e., no distinctive off-state). GFETs are ambipolar, i.e., switching from n- to p-type behavior above and below the charge neutrality point, forming a symmetric “V” shape in source-drain current (I_{ds}) vs. gate voltage (V_g) plots (Figure 2.1e).

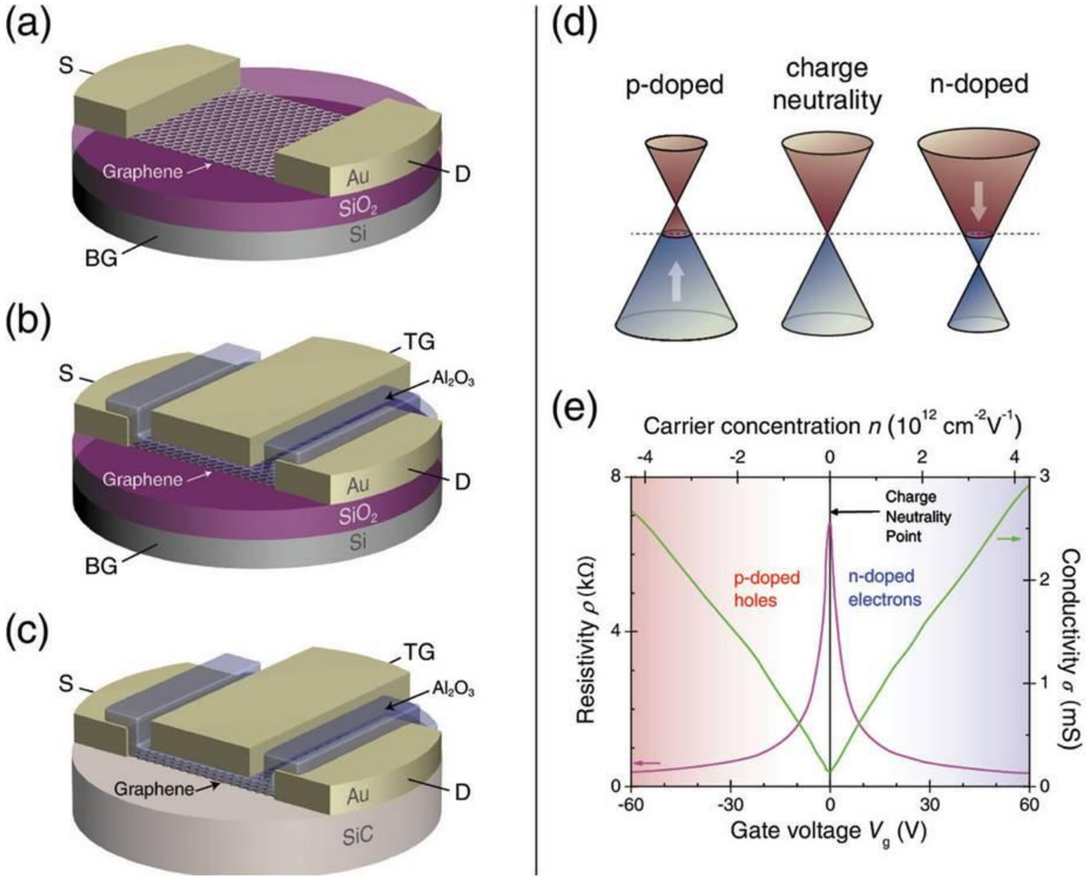

Figure 2.1 Schematics of graphene-based FETs (a) back-gated; (b) dual back- and tope-gated; (c) top-gated. (d) Schematic of band structure of charge neutrality of graphene, and the shift above and below the Dirac point. (e) Typical resistivity (purple curve) and conductivity (green curve) of graphene as a function of gate voltage. [52]

2.1.2 Graphene/ferroelectric transistors

Non-volatile memory can get back stored information even when not powered. Examples of non-volatile memory include read-only memory, flash memory, ferroelectric random-access memory (F-RAM), and so on. However, most forms of non-volatile memories have limitations that make them unsuitable for use as primary storage. Typically, non-volatile memory either costs more or has a poorer performance than volatile random access memory. F-RAM contains a thin ferroelectric film of lead zirconate titanate [Pb(Zr,Ti)O_3] (PZT). F-RAM retains its data memory when power is shut off or interrupted, due to the PZT crystal maintaining polarity. Based on these, ferroelectric materials have been employed into GFETs, aiming to realize non-volatile memory by utilizing the hybrid structure of graphene and ferroelectric.

The nonvolatility of ferroelectric gated GFETs relies on the residual polarization of ferroelectric materials when the external electric field is removed. The residual polarization can achieve a high doping concentration for the graphene layer at zero bias. Figure 2.2 shows the schematic of GFET with organic ferroelectric polymer of poly(vinylidene-fluoride-trifluoroethylene) P(VDF-TrFE) as top gate dielectric. The device state of non-volatile memory is determined by the writing voltage (V_{writing}) rather than the initial state, as shown in Figure 2.3. To be more specific, when the V_{writing} is negative, the FET shows high-resistance state “1”, regardless of the initial state of the FET.[26,29] In contrast, a positive V_{writing} with the same magnitude can set the unit cell into low-resistance state “0”. The graphene/ferroelectric hybrid structure can achieve the bit writing of “0” from “0” and “1”, respectively. So, the writing state is independent on the initial states and is only determined by the V_{writing}. And such states can be retained due to the non-volatile ferroelectric polarization. Generally, the ferroelectric materials integrated in FETs mainly include PZT thin films and organic ferroelectric P(VDF-TrFE), while graphene sheets prepared by chemical vapor deposition (CVD) and mechanical exfoliation are used in non-volatile memories.

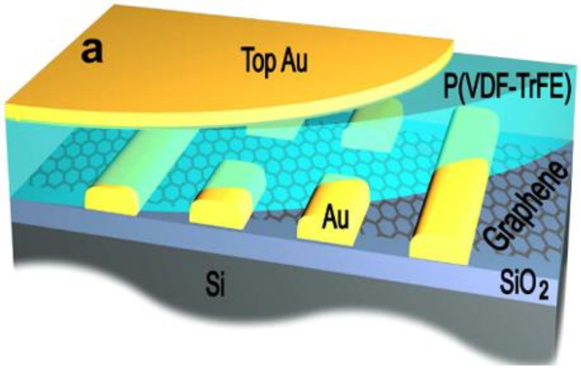

Figure 2.2 Schematics of graphene-based FETs with ferroelectric P(VDF-TrFE) as the top gate dielectric while SiO_2 as back gate insulator.[29]

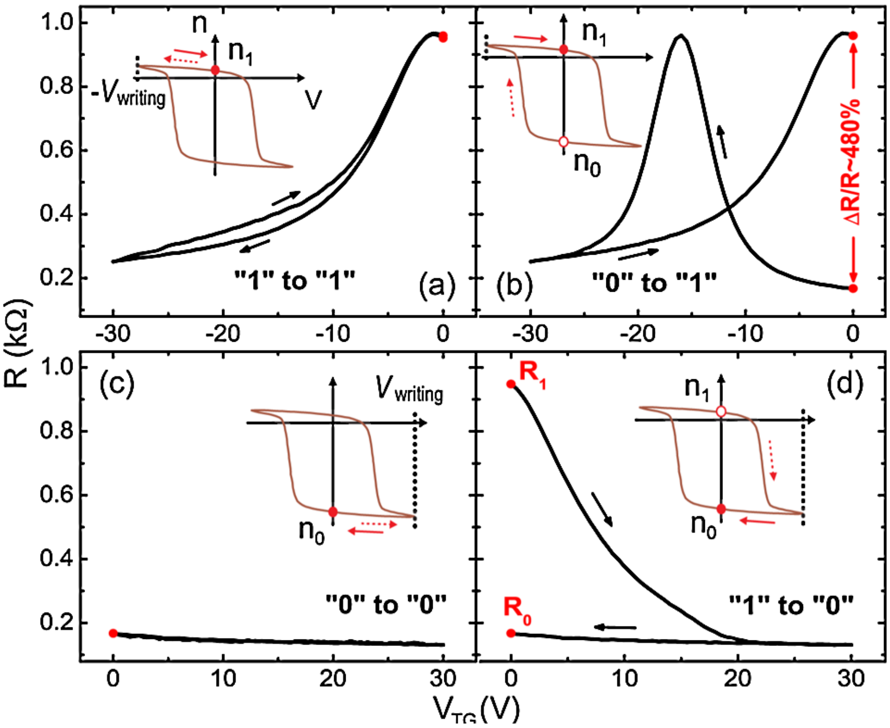

Figure 2.3 Writing process of non-volatile memory based on graphene/ferroelectric hybrid system. Symmetrical bit writing (a) from “1” to “1”; (b) from “0” to “1” by using the negative writing voltage ($-V_{\text{writing}}$); (c) from “0” to “0”; (d) from “1” to “0” by using the positive writing voltage (V_{writing}).[29]

The non-volatile memory based on graphene/ferroelectric hybrid system was ever made by Özyilmaz et al. The organic ferroelectric of P(VDF-TrFE) polymer was utilized as a top gate to functionalize the GFeFETs, while normal SiO_2 served as both bottom gate and substrate, providing independent background gating and mechanical support, respectively.[26,29] By using the SiO_2 as bottom gate, an independent bottom gate voltage (V_{BG}) could be generated to provide a well-defined and constant reference to the ferroelectric polymer, and also the doping level and carrier density of graphene could be modified by the bias voltage. At relatively high bias voltage applied to P(VDF-TrFE), the ferroelectric polarization can be switched in the unit cell. Furthermore, Song et al carefully compared mechanically exfoliated and CVD-grown graphene sheets on PZT thin films on $Pt/Ti/SiO_2/Si$ substrates.[28] For exfoliated graphene, the GFeFET exhibits large memory window which is nearly equivalent to the hysteresis of the PZT thin film. Compared to the exfoliated one, the main difference for CVD-grown graphene is the initial doping level due to the etchant solution during the process of removing the underlying Cu sheets.[53] Such effects give rise to the distinct hysteresis behaviours compared to exfoliated graphene[27,54]

2.1.3 Piezoelectric strain on graphene

From the point of view of symmetry, ferroelectric materials are found to be of non-centrosymmetric crystal structure, belonging to crystal classes lacking inversion center. Thus, ferroelectric materials can exhibit a wide range of technologically significant physical properties, such as piezoelectricity and pyroelectricity.[55] In theory, piezoelectricity results from the linear interaction between electrical and mechanical systems in non-centrosymmetric crystals. That is an external electric field can give rise to an internal structure deformation or an external mechanical deformation can induce an internal polarization charge. Besides, it is viable to provide biaxial strain to graphene by exerting an external electric field to the underlying piezoelectric material. Due to the converse piezoelectric response, a biaxial strain can be generated by the piezoelectric material, and such strain can be delivered to the above graphene layer. For example, PMN-PT single crystals are excellent piezoelectric materials which are capable of possessing high electromechanical coupling coefficients and high electrically induced strains.[56] These excellent piezoelectric properties of PMN-PT, which are superior to those traditionally used PZT ceramics, provide opportunity of them to be widely used as an actuator.[57,58] It should be noted that the strain provided by the piezoelectric crystal is biaxial strain in nature, and the structure deformation in x axis is always kept same to that in y axis. In fact, Ding *et al*. ever applied biaxial strain caused by PMN-PT to mechanically exfoliated graphene.[59] Tunable strain effects on graphene are studied by applying perpendicular electric field to the piezoelectric substrate of PMN-PT. The position of feature peaks for graphene (D, G, 2D and 2D’) can be tuned under biaxial strain, showing reproducible shifts. The Grüneisen parameters can be calculated according to the shift of feature peaks. Therefore, such novel graphene/piezoelectric hybrid system provides one an opportunity to investigate controllable biaxial strain effect on graphene. Such piezoelectric strain could induce a blue shift of Raman feature peaks of graphene under compressive strain, while a red shift under tensile strain. Nevertheless, previous investigations of biaxial strain focused mainly on the mechanically exfoliated graphene (i.e. single-crystal graphene). Generally, CVD-synthesized graphene sheets are polycrystalline and also large-area, which is of great interest for industrial applications. However, the vibrational properties of CVD-grown graphene under biaxial strain are still lacking until now.

The effect of strain on graphene has been theoretically studied by first-principle calculations[60] or experimentally measured by Raman spectroscopy.[61,62] Raman spectroscopy is considered an integral part of research for graphene and other 2D layered materials. It is used to determine the number and orientation of layers, the quality and types of edge, and the effects of perturbations, such as electric and magnetic fields, strain, doping, disorder and functional groups. The Raman spectra of graphene can be interpreted by phonon dispersion. In graphene, there are six phonon dispersion modes by considering 2 atoms per unit cell. In the six modes, there are three acoustic (A) and three optical (O) phonon modes. For both acoustic and optical phonon modes, one is an out-of-plane (Z) phonon mode and the other two are in-plane modes, one longitudinal (L) and the other one transverse (T). Thus, starting from the highest energy at the Γ point in the Brillouin zone the various phonon modes are labeled as LO, TO, ZO, LA, TA and ZA.

V

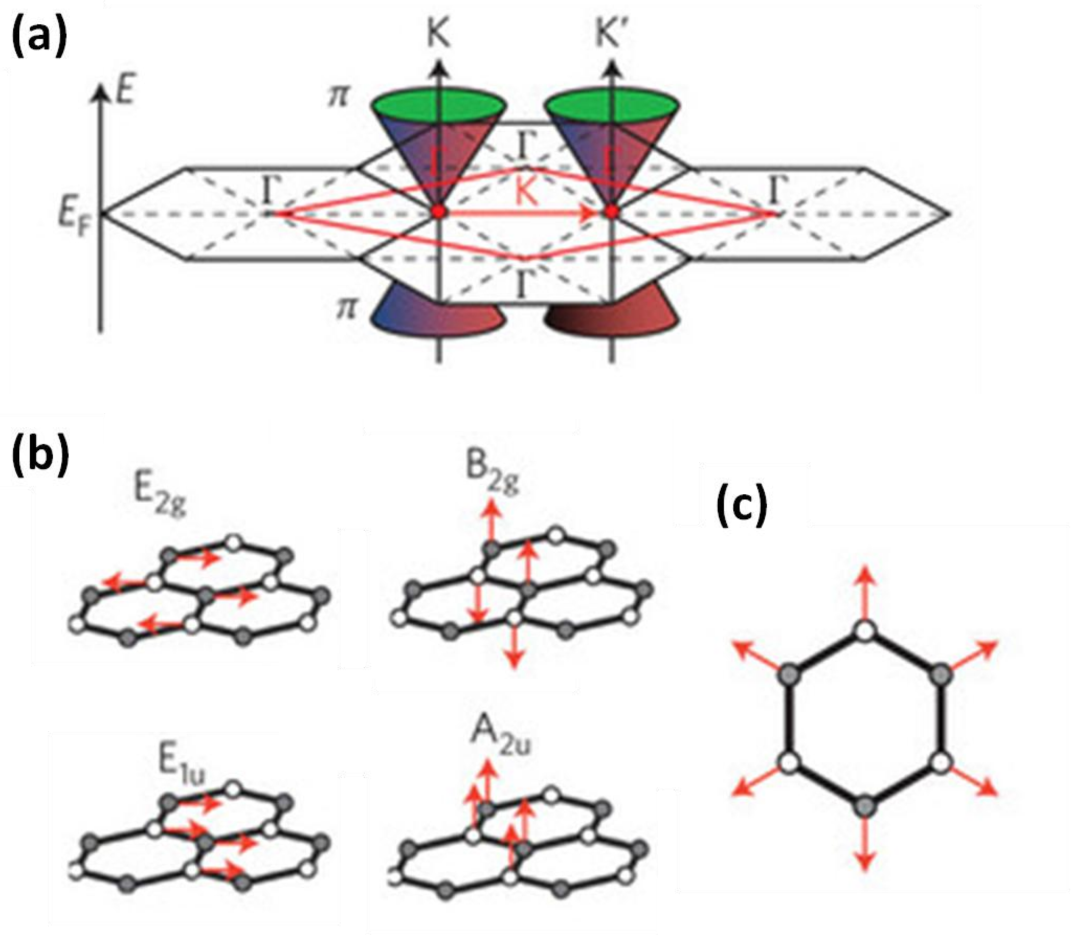

Figure 2.4 (a) Electronic Brillouin zones of graphene (black hexagons), the first-phonon Brillouin zone (red rhombus) and schematic of electronic dispersion. The phonon wave vectors connecting electronic states in different valleys are labelled in red. (b) Γ-point phonon-displacement pattern for graphene. Empty and filled circles represent in-equivalent carbon atoms. Red arrows show atom displacements. (c) Atom displacements (red arrows) for the A_{1g} mode at K point.

Figure 2.4a plots the electronic Brillouin zone of graphene, the first-phonon Brillouin zone and shows a schematic of the electronic dispersion. The optical phonons in the zone-center (Γ) and zone edge (K and K’) region are of particular interest, since they are accessible by Raman spectroscopy. Graphene has two atoms per unit cell, thus six normal modes (two being doubly degenerate) at the Brillouin zone centre Γ. A_{2u}, B_{2g}, E_{1u} and E_{2g}, as shown in Figure 2.4b. The E_{2g} phonons are Raman active, whereas the B_{2g} phonon is neither Raman nor infrared active. Both E_{1u} and E_{2g} are infrared-active. So, in graphene at the Brillouin zone centre Γ only the E_{2g} phonons are Raman active. The vibrations correspond to the rigid relative displacement of the two carbon atoms' sub-lattices. This phonon mode is Raman active and responsible for the Raman G mode in graphene, corresponding to the high-frequency E_{2g} phonon at Γ. The D peak is due to the breathing modes of six-atom rings and requires a defect for its activation, as shown in Figure 2.4c. It comes from TO phonons around the Brillouin zone corner K, it is active by double resonance, and is strongly dispersive with excitation energy, due to a Kohn anomaly at K. Double resonance can also happen as an intra-valley process, that is, connecting two points belonging to the same cone around K (or K´). This gives the so-called D´ peak. The 2D peak is the D-peak overtone, and the 2D´ peak is the D´ overtone. Because the 2D and 2D´ peaks originate from a process where momentum conservation is satisfied by two phonons with opposite wave vectors, no defects are required for their activation, and are thus always present. Note that, although being an in-plane mode, the 2D peak is sensitive to layer number because the resonant Raman mechanism that gives rise to it is closely linked to the details of the electronic band structure, the latter changing with layers, and the layers relative orientation.

2.2 Graphene/semiconductor hybrid structure

2.2.1 Graphene Schottky junction solar cells

A solar cell device can convert light to electricity with a value of power conversion efficiency (PCE) which is an important parameter to determine the behaviors of the device.[63] At early research stage in this field, graphene applied to solar cells has only been used as an alternative transparent electrode to ITO due to its some advantages, such as superior flexibility, higher transparency and better conductivity, no matter in inorganic silicon or organic polymer cells.[64,65] In fact, beyond the single role of transparent conductor, graphene can fulfill multiple functions in solar cells, such as photoactive layer, channel for charge transport, and catalyst.[66–68]

Graphene, as a semi-metal, can somewhat serve as a metal active layer to form M/S Schottky contact with some semiconductors, such as Si, SiC, GaAs, GaN and graphene oxide etc,[69,70] if the work function difference between graphene and the semiconductor is large enough, and the carrier density of the later is moderate.[71] Such M/S diodes based on the graphene/semiconductor hybrid systems may find many promising applications, such as photodetectors[72,73], solar cells,[39] light-emitting diodes (LEDs),[74] and so on. Comparatively, most reports about LEDs involved in graphene only made use of transparent and conductive characteristics of graphene instead of hetero-interface.[75–77] It is well-known that the Fermi energy level of semiconductors can be tuned by impurity doping. On the other hand, the work function of graphene can be modulated by various methods, such as electric field, doping, layer number, etc. Based on the difference of the work-function between graphene and semiconductor, the graphene/semiconductor hybrid devices can be developed. In principle, any semiconductor with electron affinity lower than the work function of graphene can create an M/S diode. As a consequence, a build-in potential is generated in the semiconductor adjacent to the Schottky junction interface due to the different work function between them. Under the illumination, the photon-generated carriers can be separated and then transferred to the electrodes, yielding photovoltaic effects from such junction devices.

2.2.2 Graphene/Si Schottky junction solar cells

Li et al reported graphene/Si Schottky junction solar cells by employing several layers of CVD-grown graphene sheets (GS), as schematically shown in Figure 2.5a. In their investigated junction solar cells, graphene was used as not only a transparent electrode for light illumination, but also an active layer for electron–hole separation and hole transport.[39,78] The photovoltaic response of the graphene/Si junction solar cell is presented in Figure 2.5b. Under air mass 1.5 (AM 1.5) illumination, light current density–voltage (*J*–*V*) data demonstrated down-shift curves with the open-circuit voltage (V_{oc}) of 0.42 ~ 0.48 V, the short-circuit (J_{sc}) of 4 ~ 6.5 mA cm^{-2}, and a fill factor (*FF*) of 45 ~56%, resulting in an overall solar energy PCE of 1.0 ~1.7%. In the junction solar cells, the graphene layer not only serves as the transparent electrodes for light illumination, but also the active layer for carrier separation and hole transform, as shown in the bottom-left inset of Figure 2.5a.

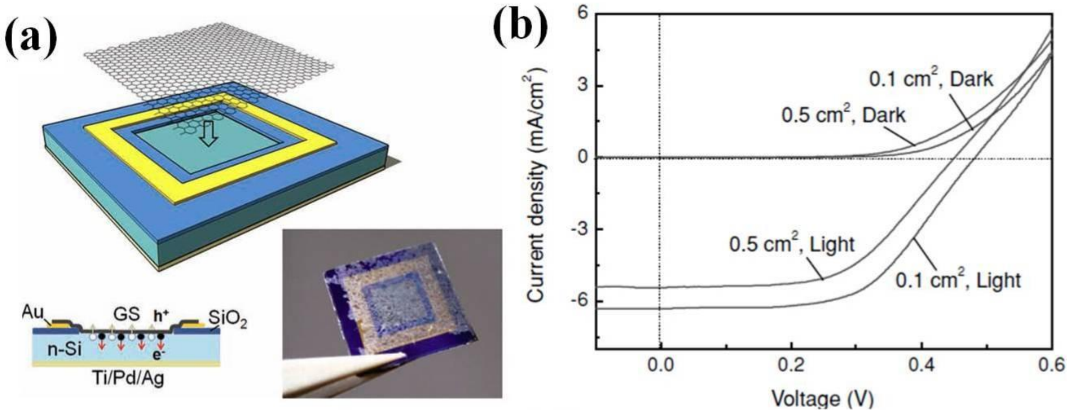

Figure 2.5 (a) Schematic of the graphene/Si junction solar cells. The cross-sectional view of the junction is shown in bottom-left inset, photogenerated holes (h^+) and electrons (e^-) are driven into the graphene and Si, respectively. Bottom-right inset shows real image of the Schottky junction solar cell. (b) Dark and Light *J*–*V* curves of the graphene/Si Schottky junction solar cells illuminated with AM 1.5.[39]

As above introduced, single-junction graphene-based photovoltaic devices have attracted much attention due to their simplifying fabrication process and potential widespread applications.[79,80] However, the conversion efficiency of pristine graphene-based cells is still not comparable to traditional Si or GaAs junction solar cells.[81] As a result, many efforts have been put on to improve the performance of graphene-based Schottky junction solar cells. For example, chemical or substitutional doping to graphene layer can reduce graphene's sheet resistance or achieve p-type modification, and therefore increase the built-in potential. These would be beneficial to the reduction of the ohmic losses and the enhancement of the electron-hole pairs separation generated by absorbed photons. Different p-doping methods have been developed like chemically treatment with HNO_3[82] or $AuCl_3$ solution,[83] and thionyl chloride ($SoCl_2$) vapor,[84] direct incorporation of boron in CVD process.[85] Note that doping with bis(trifluoromethanesulfonyl)-amide [($(CF_3SO_2)_2NH$)] (TFSA) can result in an about 3~5 times increase in PCE of the graphene/n-Si Schottky junction solar cell jumping from 1.9 to 8.6%.[86] The improved light harvesting in chemically doped graphene/n-Si Schottky junction solar devices has been attributed to the reduction of graphene's sheet resistance and an increase in the built-in potential. The method is considered as a practical, simple and scalable routine since device fabrication involves simple planar thin-film geometries, conventional graphene production techniques and uncomplicated spin-casting of organic layers. However, the stability of the organic overlayers has not been reported. In addition, the layer number of graphene should be carefully tuned to compromise the electrical and optical properties, including work function, sheet resistance and film transmittance.[87] Moreover, some antireflection techniques are effective ways to reduce the optical losses, such as the introduction of a pillar-array periodic patterned structure to Si.[88] A PCE of graphene/Si junction solar cell was reported to be 14.5% through spin-coating the antireflection layer of TiO_2

onto graphene/Si.[89] The detailed performance parameters of graphene-based Schottky junction solar cells with various methods to enhance the device performance are summarised in Table 2.1.

Table 2.1 Performance parameters of graphene/Si Schottky junction solar cells. Some methods are used to improve the performance of the solar cells.

Semiconductor	Methods to improve performance	V_{oc} (V)	J_{sc} (mA/cm^2)	PCE	Ref.
Si	Pristine	0.48	6.5	1.65	39
Si NW	$SoCl_2$ doping	0.503	11.24	2.86	84
Si	Boron doping and HNO_3 modification	0.57	21	3.4	85
Si	Si-pillar-array and HNO_3 doping	0.515	22.7	7.72	88
Si	TFSA doping	0.54	25.3	8.6	86
Si	Multilayer graphene and HNO_3 doping	0.55	16.91	9.63	80
Si	TiO_2 coating and HNO_3 doping	0.62	32.5	14.5	89

2.2.3 Graphene/GaAs Schottky junction solar cells

In comparison with currently widely studied Si in graphene-based junction solar cells, there is rare work on graphene/GaAs solar cells. By considering the merits of direct band gap and high electron mobility (8000 cm^{2}V^{-1}s^{-1} at 300 K) which is about 6 times of that of Si (1350 cm^{2}V^{-1}s^{-1} at 300 K), GaAs should be one of the best candidates for high performance solar cells. Currently, the most widely studied solar cells are based on silicon with the efficiency of about 25% obtained from single p-n junction of crystalline Si, while GaAs-based solar cells show higher efficiency of more than 28%.[90] Previously, several types of heterostructures of perovskite oxide thin films and GaAs have been studied by our group.[91–93] Very recently, we combined CVD-grown graphene sheets with GaAs wafer to fabricate the Schottky junction solar cell based on graphene/GaAs. Single- and bi-layer graphene sheets were transferred onto n-type GaAs substrate with about 200-nm SiO_2 as insulating layer to form a graphene/GaAs Schottky barrier. Among them, bilayer graphene/GaAs junction shows better photovoltaic behaviors with the V_{oc} of 0.65 V, J_{sc} of 10.03 mA/cm^2, yielding the PCE of 1.95 %.[94] Such performance parameters of the device are comparable to above mentioned graphene/Si junction-based devices. By considering the high-performance of optoelectronic capabilities of radiation-resistant GaAs wafer, this work exhibits that the developed graphene/GaAs system may be an attractive system for future photovoltaic applications. Very recently, Li et al reported high performance solar cells with graphene/GaAs structure.[95] Similar to the methods to enhance the photovoltaic behaviors used in graphene/Si junction solar cells, TFSA doping and anti-reflection coating (ARC) techniques have been employed to graphene/GaAs junction solar cells. PCE of 10.4% have been achieved by TFSA doping. Furthermore, through anti-reflection technique, the PCE value has been further improved up to 15.5%, which is higher than that of graphene/Si solar cell. The *J*−*V* curves of the junction solar cells with different modification are shown in Figure 2.4a. Furthermore, calculation points out PCE of 25.8% can be reached by reasonably optimizing the open circuit voltage, junction ideality factor, resistance of graphene and metal/graphene contact, as shown in Figure 2.4b. This further means that graphene/GaAs heterostructure solar cells have great potential for practical applications.

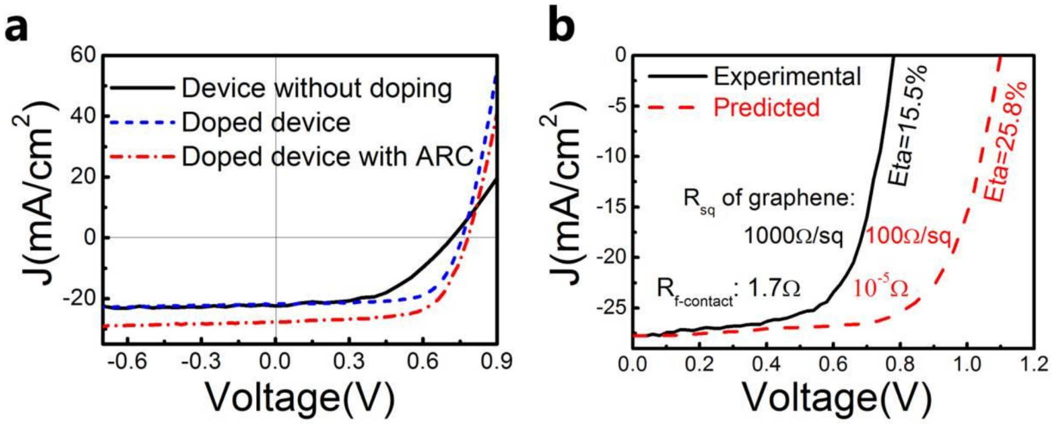

Figure 2.6 (a) Experimental *J*−*V* curves of graphene/GaAs solar cells with as-grown graphene, with TFSA doping and with both doping and anti-reflection coating. (b) Experimental and calculation predicted *J*−*V* curves of the best graphene/GaAs solar cells.[95]

Table 2.2 Performance parameters of graphene-based Schottky junction solar cells combined with different semiconductors.

Semiconductor	Methods to improve performance	V_{oc} (V)	J_{sc} (mA/cm^2)	PCE	Ref.
GaAs	Pristine	0.65	10.03	1.95	94
GdSe NB	Pristine	0.51	5.75	1.25	96
CdS NW	Integrating 5-nm Au electrode	0.15	NA	1.65	97

GaAs	TFSA doping and anti-reflection coating	0.76	22.5	15.5	95

Besides, The Schottky junction solar cells can be fabricated by combining graphene with other semiconductor nanostructures like CdS nanowire (NW) and CdSe nanobelt (NB).[96,97] These nanojunctions shows comparable photovoltaic behaviors to pristine Si or GaAs Schottky junction solar cells. The performance parameters of graphene-based Schottky junction solar cells with different semiconductors are summarized and exhibited in Table 2.1.

2.3 Nonlinear optical properties

2.3.1 Introduction

Nonlinear optics (NLO) is the behavior of light in materials lacking inversion symmetric center. In these materials, dielectric polarization responds nonlinearly to the electric field of the light. The nonlinear phenomenon can only be observed when the light is of high intensity, typically high energy pulse laser. Second harmonic generation (SHG), also called frequency doubling, is a nonlinear optical process, in which photons with the same frequency interacting with a nonlinear material to generate new photons with twice the energy, and therefore twice the frequency and half the wavelength of the initial photons.

2.3.2 Nonlinear optical properties in GaSe

GaSe is a well-known crystal which can produce second harmonic response in NLO. GaSe is a highly anisotropic semiconductor, which consists of layers of covalently bonded stacks with top and bottom layers of Se and two layers of Ga ions in the middle, i.e., in the sequence of Se-Ga-Ga-Se, with a lattice constant of 0.374 nm and the basic layer thickness of about 0.9 nm. Bulk GaSe has an indirect band gap of about 2.0 eV and a direct band gap of only 25 meV higher. The electron can easily transfer between the two energy levels with a small amount of thermal energy. In addition, GaSe crystals possess wide transparency range from 0.65 to 18 μm, relatively high birefringence and high threshold damage value for different laser lines.[98] Note that one of the most important properties of bulk GaSe is the nonlinear optical property.[48,49] GaSe has been used in laser equipment as a far-infrared conversion material.

For GaSe crystals, there are several different modifications which differ in the stacking sequence, and the three most important classifications are so-called β-GaSe, ε-GaSe, and γ-GaSe.[99] The unit cells of these three deformations are schematically shown in Figure 2.5. Among them, γ-GaSe has a 3R stacking sequence, belonging to noncentrosymmetric space group of C^4_{6v}, as shown in the right of Figure 2.5. Both β-GaSe and ε-GaSe are hexagonal symmetric with a 2H stacking, and they will be used in our experiments in later section. β-GaSe has two basic layers per unit cell and belongs to space group of D^4_{6h}. It is centrosymmetric, which has the same crystal symmetry with MoS_2 and WS_2. On the other hand, the *ε*-GaSe is noncentrosymmetric due to the stacking sequence and belongs to space group of D^1_{3h}. Among different modifications, *ε*-GaSe ranks the most efficient nonlinear material with high nonlinear coefficient (d_{eff}) of 54 pm/V.

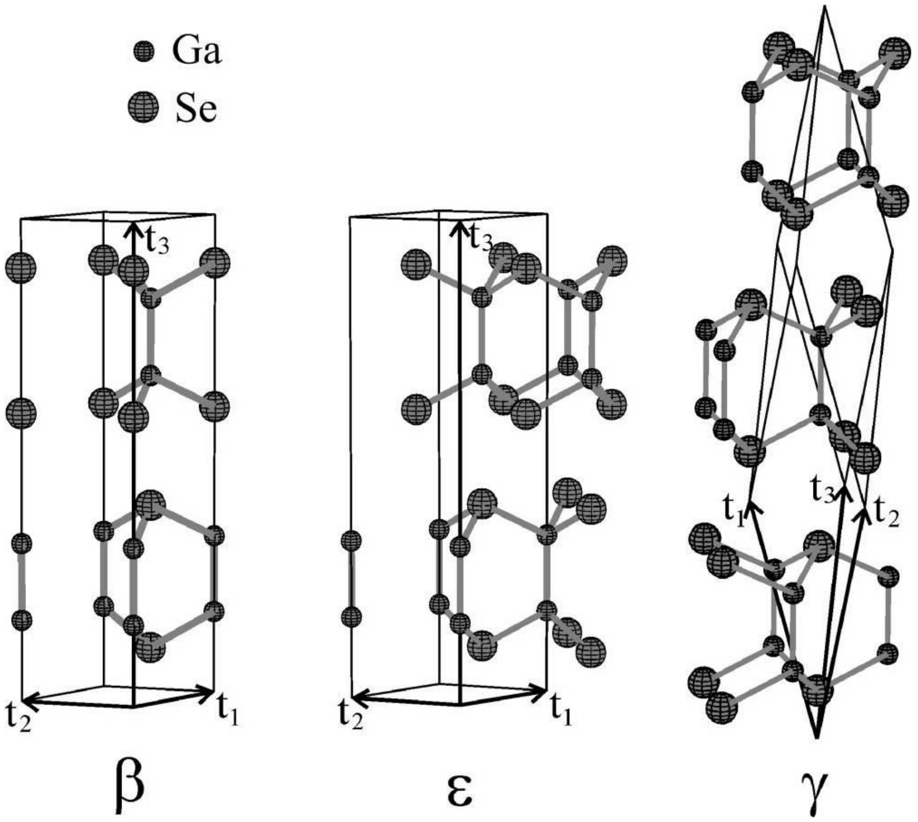

Figure 2.7 Unit cells for different modifications of GaSe: *β*-GaSe (left), *ε*-GaSe (middle), and *γ*-GaSe (right).[99]

In comparison with their bulk counterparts, 2D GaSe layers are expected to have a tunable band gap, high photoresponsivity, and high sensitivity due to the large surface-to-volume ratio and the distinct quantum confinement on their optical and electronic properties. Single-layer GaSe was first reported by Late et al in 2012 via mechanical exfoliated method.[21] After that, GaSe layers were transferred onto SiO_2/Si substrates for the fabrication of FETs and high-performance photodetectors.[23,25] The transport properties of GaSe were characterized based on the GaSe FET which shows p-type properties with an on-off ratio of about 105 and a mobility of $0.6 cm^2V^{-1}s^{-1}$at room temperature. On the basis of the GaSe transistor, a photodetector was fabricated, showing a fast response of 0.02 s, high responsivity of 2.8 AW^{-1} and high external quantum efficiency of 1367% at 254 nm.

Beyond mechanically exfoliated GaSe, several methods have been developed to grow GaSe layer, such as vapor phase mass transport, van der Waals epitaxy and pulse laser deposition methods. GaSe atomic layers were successfully synthesized directly on SiO_2/Si substrate by a vapor phase mass transport method.[98] Few-layer high quality GaSe sheets as large as tens of micrometers have been synthesized by this method. By utilizing the synthesized large-area GaSe layers, a photodetector was prepared, showing an evident electrical photoresponse and a low dark current. The on−off ratio is in the order of 10^3. In addition, GaSe layers have been fabricated on mica substrate using a van der Waals epitaxy method.[99] Single- and few-layer GaSe nanosheets with the lateral size of up to tens of micrometers were prepared. The 2D GaSe crystal-based photodetectors were demonstrated on both mechanically rigid SiO_2/Si and flexible mica substrates. Efficient photoresponse was observed in 2D GaSe crystal devices on transparent flexible mica substrates, regardless of repeated bending with different radii. The controlled growth of 2D GaSe crystals with efficient photoresponsivity opens up opportunities for both fundamental aspects and new applications in photodetectors. Besides, pulse laser deposition method was employed to grow GaSe nanosheets using a bulk GaSe target. The prepared GaSe nanosheets show p-type semiconducting characteristics with mobilities reaching as high as 0.1 $cm^2V^{-1}s^{-1}$at room temperature. By using the synthesized GaSe sheets, some optoelectronic devices have been developed, showing strong photoresponse. Pulsed laser deposition appears to provide a versatile and rapid approach to stoichiometrically transfer and deposit functional networks of 2D nanosheets with digital thickness control and uniformity for a variety of applications.[102]

The widely-developed GaSe layers via mechanical exfoliation, chemical or physical growth methods offer more opportunities for potential applications in optoelectronic devices. However, the nonlinear optical properties, one of the most important behaviors of bulk GaSe, have not been investigated until now in 2D form.

2.3.3 Nonlinear optical properties in other 2D materials

In atomically layered materials, the individual layers will generally exhibit different symmetry from the corresponding bulk crystals. Few-layer materials of different layer thickness can moreover have distinct symmetries from one another, even when their thickness differs by only one atomic layer. Since symmetry plays a critical role in defining the material properties, such differences in symmetry lead to significant differences in material properties. Bulk TMDCs, like bilayer MoS_2 and WS_2, are stacked in 2H order, with pairs of layers forming a unit and belong to the same centrosymmetric D_{6h}^{4} space group. As a consequence, bulk TMDCs are not capable of producing SHG. However, single-layer MoS_2 and h-BN are noncentrosymmetric materials, while their bilayers and bulk counterparts are expected to exhibit inversion symmetry. The broken inversion symmetry in TMDCs of single-layer implies the possibility of second harmonic generation. In contrast, bilayer TMDCs, like bilayer MoS_2 and WS_2, were reported to show negligible second order optical nonlinearity due to the restoration of inversion symmetry.

Figure 2.6a and b show the optical and AFM image of the MoS_2 flake. Mono-, bi- and tri-layer (1L, 2L and 3L) MoS_2 can be obtained by mechanical exfoliation method. The SHG image is shown in Figure 2.6c. The most intense second harmonic emission comes from the monolayer part, while SHG degrades in trlayer and even vanishes in bilayer one. Second harmonic intensity profile shown in Figure 2.6d indicates the parity-dependent SHG. Similar behaviors of the enhanced second harmonic response in odd-layered TMDCs nanosheets also have been reported by other groups.[103–106] Abnormally, SHG can be detected in artificially stacked TMDCs bilayers with an arbitrary stacking angle and *h*-BN bilayers with broken inversion symmetry.[107,108]

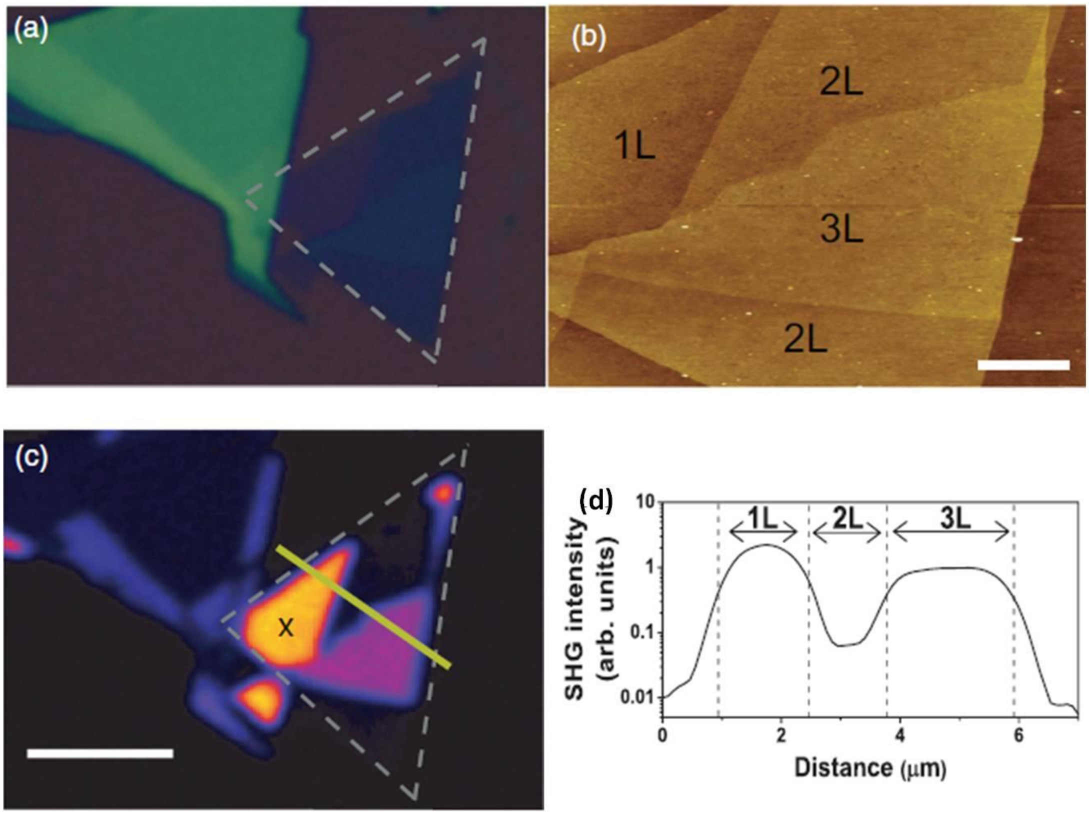

Figure 2.8 (a) Optical image of exfoliated MoS_2. (b) Atomic force microscopy identification of mono-, bi- and tri-layer (1L, 2L and 3L) MoS_2. (c) SHG image of the same flake. (d) Second harmonic intensity profile got from the yellow line at part (c).[104]

Chapter 3 **Experimental Techniques**

The important experimental techniques employed in our experiments will be introduced in this chapter, including the preparation and transfer methods of graphene and GaSe nanosheets, the structural characterization techniques of atomic force microscopy and x-ray diffraction, the electrical characterizations of FETs and solar cells measurement systems, as well as the optical characterizations of micro Raman spectroscopy, confocal laser scanning microscopy and nonlinear optics measurement system.

3.1 Fabrication of graphene and 2D layered GaSe sheets

3.1.1 Growth of graphene by CVD method and transfer process

As of now, several methods have been developed to grow or synthesize graphene sheets. The widely-used ways to produce graphene include mechanical exfoliation, the desorption of Si from SiC single-crystal surfaces,[109] surface precipitation process of carbon in some transition metals,[110] chemical reduction of graphene oxide to produce covalently functionalized single-layer graphene,[111] chemical exfoliation,[112,113] and so on. The first graphene sheet was obtained by mechanical exfoliation of highly oriented pyrolytic graphite with a Scotch tape. Micro-scale graphene flakes can be cleaved and adhered to the subsequent target substrate.[114] The exfoliated graphene possesses superior properties. However, the size of such graphene sheets is limited and it is difficult to achieve wafer-scale graphene by mechanically exfoliated method. Consequently, several alternative methods have been developed to grow graphene, such as epitaxial growth and CVD. High-quality large-area graphene can be fabricated on single-crystal SiC by epitaxial growth method. While CVD method has been employed to grow large-area graphene sheets on metal surfaces, like Ni and Cu.[115,116] CVD-grown graphene are typically polycrystalline consisting of many domain boundaries and graphene wrinkles[116] However, CVD-grown graphene can be easily transferred onto target substrates by etching away the underlying metal foils. This gives CVD-grown graphene a chance to be widely used in many integrated devices.

Graphene is prepared by CVD method on Cu foils in our experiments. Firstly, put 25-μm thick Cu foil in quartz tube, anneal the Cu foil to 1000 ℃ for 30 min with the flow of $H_2(g)/Ar(g)$ at a flow rate of 10:50 SCCM (standard center cubic per minute). Then, introduce $CH_4(g)$ at 1000 ℃ for 10 min. After the reaction process, the quartz tube is pulled out from the hot zone of the furnace and cooled naturally with the flow of $H_2(g)/Ar(g)$. After that, monolayer graphene can be obtained on the copper foil. The reaction time and flow rate of purging gas can be varied to control the thickness of graphene.

Typically, graphene grown on metal foils must be transferred onto insulating substrates for device fabrication and electronic characterization. Up to this date, various methods have been demonstrated to transfer the as-grown graphene on metal substrates onto target insulating substrates. The typical way is to chemically etch the underlying metal sheets away to obtain a free standing graphene membrane. This membrane can then be scooped on a target substrate. Besides, Kim et al reported a dry-transfer method using a soft substrate of PDMS stamp to transfer pre-patterned graphene with various size and shape.[115] Bae et al proposed a roll-to-roll transfer method which could transfer 30-inch graphene films from copper sheet onto plastic substrate with a polymer support.[117] A bubbling method was employed to transfer graphene sheets grown on Pt substrate to an arbitrary substrate.[118] This approach is essentially nondestructive not only to graphene, but also to Pt substrate.

In our experiments, a general technique is used to transfer CVD-graphene onto a target substrate, as illustrated in Figure 3.1. The transfer process is firstly performed by spin-coating a thin polymeric layer, such as polymethyl methacrylate (PMMA), on top of the graphene. This polymer provides a mechanical support to graphene before the transfer. The underlying Cu foil can then be etched away by solution of iron chloride ($FeCl_3$). Typically, it takes several hours for the Cu foil to be completely dissolved. After that, the floating membrane of graphene with a support from the above polymer can be scooped on a target substrate. After drying, a good adhesion can be formed between graphene and the target substrate. Then, the polymer can be dissolved with acetone. At last, graphene layer is left on the target substrate.

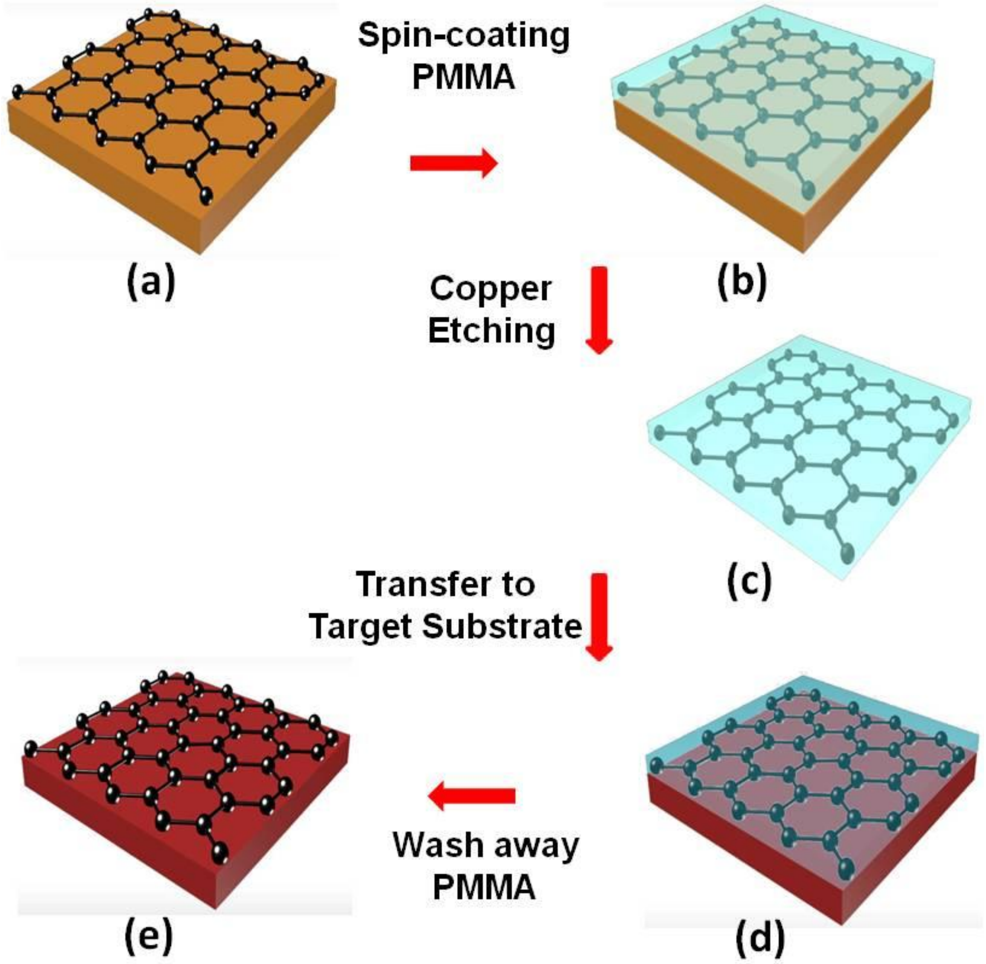

Figure 3.1 A typical method to transfer graphene from Cu foils to the target substrate. (a) Graphene on Cu foils. (b) PMMA coated graphene on Cu foils. (c) PMMA supported graphene after etching the Cu foils. (e) Transfer PMMA/graphene onto the target substrate. (e) Graphene on target substrate after the above PMMA layer is dissolved.

3.1.2 Preparation of GaSe nanosheets by mechanical exfoliation

The growth method of graphene has been expanded to other 2D layered materials. For example, many 2D layers have been obtained from their bulk materials by mechanical exfoliation which is a convenient way to obtain micro-scale nanosheets with high quality. In our experiments, few-layer GaSe sheets are prepared by using Scotch tape from a piece of 2H-stacking GaSe crystal. Then the nanosheets on the adhesive tape are transferred onto a target substrate, typically, 300-nm SiO_2 coated Si substrate. The high-quality GaSe crystal is purchased from 2D Semiconductors. GaSe has a layered structure with weak interlayer coupling of Van der Waals force, which is easy to be cleaved from its bulk crystal. A small piece of GaSe crystal is put on a clean adhesive tape. Then, refold the tape and press firmly, then the tape is gently unfolded, leaving two mirrored areas of GaSe crystals on the tape. This process should be repeated for several times until a large portion is no longer shiny, but dark grey. After conducting these processes, some micro-scale GaSe flakes can be obtained on the adhesive tape. Then, put this area onto SiO_2 wafer and press firmly to the tape, followed by gently removing the tape. Then some GaSe sheets with different layer number can be obtained on the SiO_2 wafer.

These GaSe layers can be observed by using an optical microscope. 300-nm thick SiO_2 is ideal as a substrate because it allows GaSe nanosheets to be visible with the naked eye under white light, and more importantly, contrast between these nanosheets with different thickness is relatively high, as shown in Figure 3.2. The green color ones are typically of multilayer. The metal color flakes are generally above 20-layer. Further characterization is needed to determine the layer number by atomic force microscopy, which will be introduced in the next section. The left part of the green sheet in Figure 3.2a is about 5-layer, while the right part is about 7-layer. In Figure 3.2b, the thinnest green part on the left of the nanosheet is about 3-layer. In the vicinity of 3-layer GaSe, 5- and 7-layer nanosheets can be obtained.

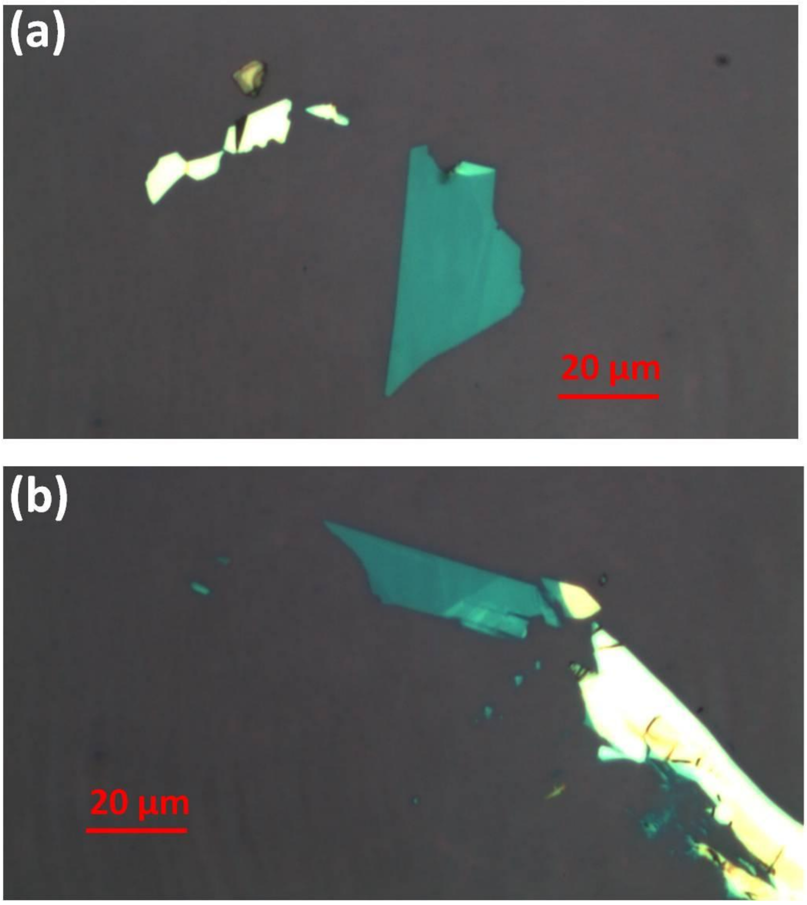

Figure 3.2 Optical image of mechanically exfoliated GaSe sheets (a) 5- and 7-layer; (b) 3-, 5- and 7-layer on SiO_2 substrates.

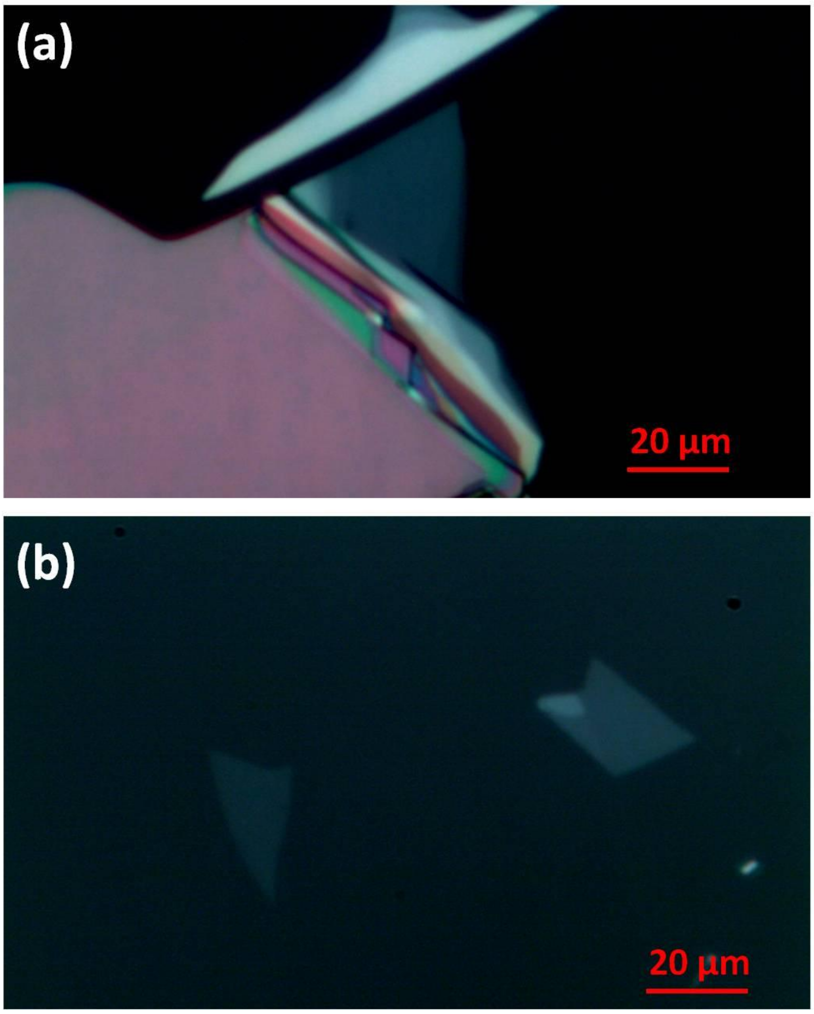

Figure 3.3 Optical image of mechanically exfoliated GaSe sheets (a) 3-layer; (b) 3- and 5-layer on transparent glass substrates.

In our experiments, it is also essential to prepare GaSe layers on transparent glass substrate. However, it is more difficult to find GaSe layers on transparent substrates compared to those on SiO_2/Si substrates. It is also unlikely to determine their layer numbers only by the optical microscope. But, the optical contrast still can provide us some thickness information. For GaSe on glass, the representative optical images are shown in Figure 3.3. The GaSe thin layers exhibit light grey colors. The thinner the layers are, the lighter the colors are. As shown in Figure 3.3a, the grey nanosheet in the center is about 5-layer, while the pink and yellow flakes are relatively thick, more than 20-layer. In Figure 3.3b, there are two nanosheets with thickness of few-layer: the left one is about 3-layer, while the right one is about 5-layer.

3.2 Structural Characterizations

3.2.1 Atomic force microscopy

Atomic force microscopy (AFM) is performed by monitoring the attractive and repulsive forces between a probe (tip) and a sample surface. The schematic of AFM setup is shown in Figure 3.4. Traditionally, the sample is mounted on a piezo crystal and can be moved in the x, y, and z directions using a single piezotube. The tip is attached to a cantilever which moves up or down in response to forces of attraction or repulsion with the sample surface. A photodetector is employed to detect the movement of the cantilever using a laser spot reflected from the top surface of the cantilever. When the tip is brought into proximity of a sample surface, a deflection of the cantilever can be induced by the forces between the tip and the sample. Typically, the deflection is measured by a feedback mechanism which is generally employed to adjust the tip-to-sample distance to maintain a certain force between them.

The AFM can be operated in a number of modes. In general, possible imaging modes are divided into static (also called contact) mode and dynamic (non-contact or "tapping") mode. Contact AFM can introduce damage to samples and obtain distort image data. Non-contact mode generally provides low resolution image and can also be hampered by the contamination. However, tapping AFM is developed to achieve high resolution surface image without damage to the samples. Thus, the soft and fragile samples can be imaged successfully by tapping mode. In our experiments, tapping mode is used to obtain high resolution image without destruction to the samples.

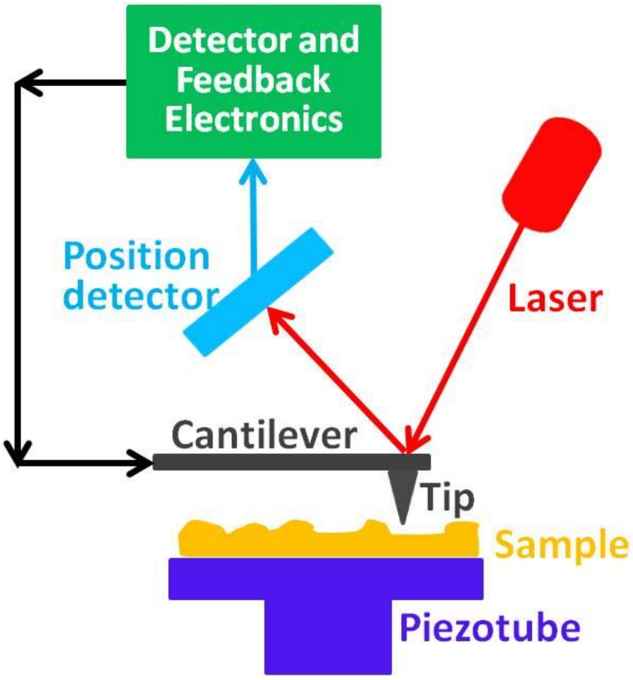

Figure 3.4 Schematic of the setup of atomic force microscopy.

3.2.2 X-ray diffraction

X-ray diffraction (XRD) is a powerful analytical technique to investigate the internal structure of crystals. This technique utilizes the interaction between X-ray and the crystalline samples to obtain a diffraction pattern which is distinct, like a fingerprint of the sample. When an X-ray beam hits an atom, the electrons around the atom start to oscillate with the same frequency as the incoming beam. If the combining waves are out of phase, there is no resultant energy leaving the solid sample. Accordingly, no diffraction peak shows up. However, in crystalline materials, the atoms are arranged in a regular pattern in a long distance. Some parallel planes can be formed inside the crystalline materials. Constructive interference will be induced in some directions. We model X-ray reflections from a series of parallel planes inside the crystal, as shown in Figure 3.5.

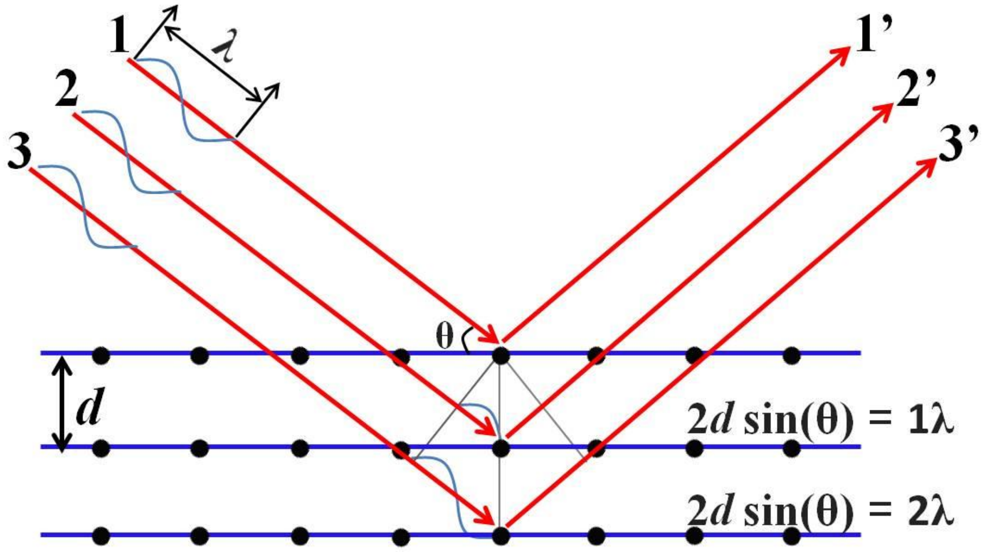

Figure 3.5 Schematics of the work principle of X-ray diffraction.

The X-ray with wavelength of λ hits atoms in the crystal. The two parallel incident X-rays make an angle (*θ*) with these parallel planes. If the reflective waves are in phase, the reflected beam will reach a maximum of intensity. This may happen under the condition of the difference between the two paths of the parallel X-ray must be an integral number of wavelength (λ). We can express this relationship mathematically in Bragg's law:

$$2d \sin(\theta) = n\,\lambda \tag{3.1}$$

where n is an integer and d is the distance between two nearest parallel planes. When the difference in path length meets the Bragg's law, a diffraction peak will arise at 2θ when scanning by θ-2θ mode. Based on this, we can get the diffraction pattern. According to the pattern, we can directly determine the crystal structure of the sample when compared with the standard diffraction pattern. Besides, we can calculate the distance between the two parallel planes and determine the crystal direction.

3.3 Electrical characterizations

3.3.1 Four-probe measurement system

In our experiments, the measurements of transport properties of graphene and GFETs are performed by using a home-made four-probe measurement station. The setup of this system is schematically shown in Figure 3.6. For FETs, there are three electrodes of source, drain and gate, which should be connected to the measurement system. In this system, Keithley sourcemeters not only serve as the power source to provide voltage, but also act as the meter to measure the current. To be more specific, the Keithley 2400 and 2410 sourcemeters are used to provide source-drain voltage and the gate voltage, respectively. At the same time, both sourcemeters can be employed to measure the currents through drain and source as well as gate and source. In addition, a microscope is used in this system to help find nano- and micro-scale samples or/and devices. By employing this system, we can obtain the source-drain current as a function of the gate voltage as well as the output characteristic properties of GFETs. Besides, this system can be used to measure temperature-dependent resistance for samples with four-probe configuration with the temperature ranging from 15 to 300 K using a cryogenic system (Janis CCS 150SH, Wilmington, MA).

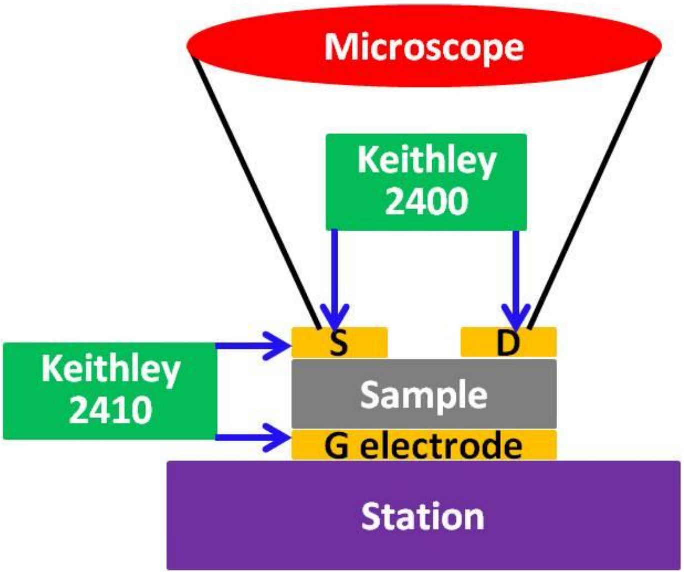

Figure 3.6 Setup of four-probe measurement system.

3.3.2 Solar cell characterization system

Solar cells are optoelectronic devices that absorb photons from sunlight and then release electrons, resulting in an electric current to flow when the cell is connected to a load. A solar cell can convert sunlight directly into electricity. Thus, a solar cell characterization system needs a light source and an electrical measurement system.

The key point is to develop a system for the characterization of the solar cells under standard test conditions (so-called STC, i.e., light illumination of air mass 1.5 (AM 1.5), normalized to 1000 W/m^2 and 25 ℃. A variety of measurements are used to characterize a solar cell’s performance, including its current–voltage curves in dark and in light, open-circuit voltage, short-circuit current density and its power conversion efficiency. In our experiments, the photovoltaic effects of the devices are tested by employing a solar simulator (Thermo Oriel 91192-1000) under conditions of AM 1.5 illumination to serve as a light source. The setup of this system is shown in Figure 3.7. The current–voltage data is recorded by Keithley 2400 sourcemeter. Besides, a probe station is integrated to this system to manipulate small solar cell devices and contact the devices to the measurement system. All the electrical measurements are performed in air ambient at room temperature.

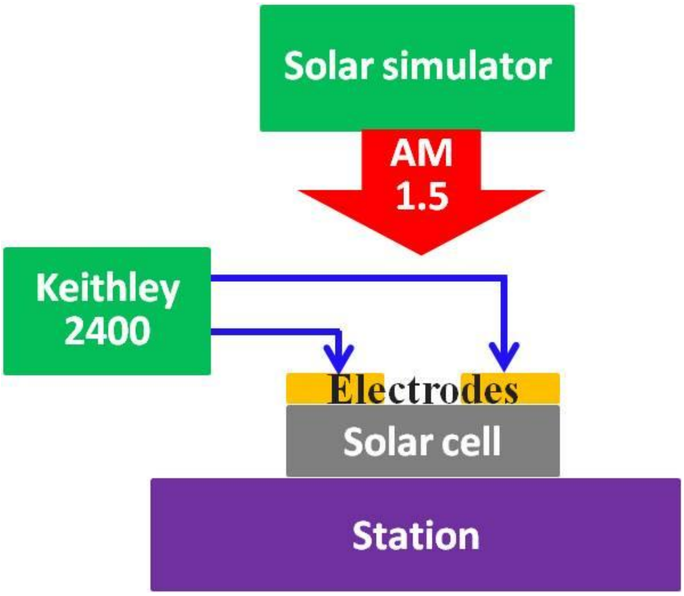

Figure 3.7 Setup of solar cell measurement system.

3.4 Optical Characterizations

3.4.1 Raman spectroscopy

Raman spectroscopy is considered an integral part of research for graphene and other 2D layered materials. It is used to determine the number and orientation of layers, the quality and types of edge, and the effects of perturbations, such as electric and magnetic fields, strain, doping, disorder and functional groups. Raman spectroscopy utilizes the process of Raman scattering to identify the materials by analyzing the shift in wavelength of light scattered by the target material. There are two primary scattering types when light strikes the target material, i.e., Rayleigh and Raman scattering, as schematically shown in Figure 3.8.

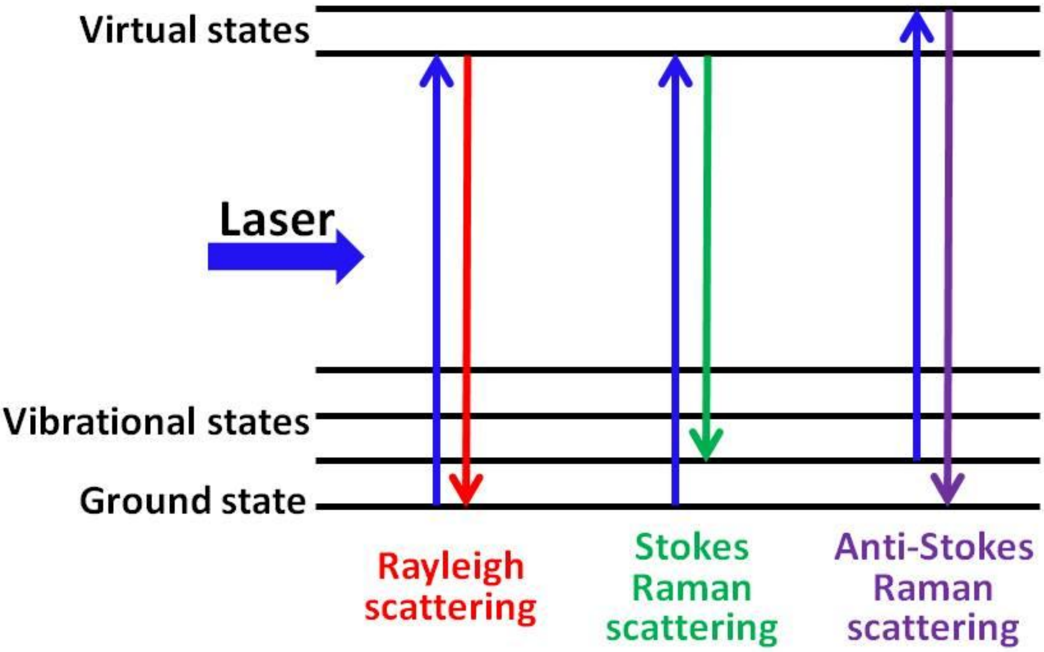

Figure 3.8 Three forms of scattering: Rayleigh scattering, Stokes and anti-Stokes Raman scattering.

In Rayleigh scattering, a target molecule or atom jumps from the ground energy state to a virtual energy state after absorbs a photon from the incident light. Then, the molecule comes back down to its original energy state, releasing another photon with the same energy as the absorbed incident photon. Therefore, Rayleigh scattering is an elastic process. On the other hand, in Raman scattering, when the molecule drops from its virtual energy state, it does not drop to its original energy state, but to a state above or below its original energy state, so called Stokes or anti-Stokes Raman scattering, respectively. Because the energy of the photons is not conserved, Raman scattering is an in-elastic scattering. Rayleigh scattering occurs much more often than both Raman scattering, and Stokes scattering happens marginally more frequently than anti-Stokes. The shift in photon energy of Stokes and anti-Stokes shifts will be the same. Thus, Stokes scattering is usually used in Raman spectroscopy due to its marginally higher frequency of occurrence compared to anti-Stokes scattering.

In Raman scattering, the energy removed from or transferred to the photon is related to specific phonons, i.e., lattice vibrations of the material. Thus, only certain changes in photon energy are possible. These frequency shifts are distinct for different materials, implying that measurements of the shift in frequencies can be used to identify the material. However, not all modes appear in the Raman spectrum, only those that do involve changes in the polarizability of the target molecule or atom.

3.4.2 Confocal laser scanning microscopy

Confocal laser scanning microscopy (CLSM) can be used to obtain high-resolution optical images with depth selectivity. Three-dimensional optical image can be constructed via acquiring signal point-by-point with a computer. One of the essential features of confocal microscopy is to acquire in-focus images from selected depths. The setup of CLSM is schematically shown in Figure 3.9. In a confocal microscope, laser lines with tunable wavelength and power can be chosen as the light source. A laser through a light source aperture and then is focused into or on the surface of a specimen with a small focal volume. The objective lens can re-collect all the emission light, including scattered, reflected and transmitted light as well as any fluorescent light. Some portion of the light is separated by a beam splitter. This is a filter device that separates the excitation from the emitted light in the fluorescence beam path of the microscope. Some fluorescent wavelengths can be selectively passed, while the original excitation wavelength will be blocked. Objective lenses are designed for specific immersion media such as water, oil, air or glycerol and should only be used with the appropriate medium. For multi-fluorescence image acquisition, only lenses that are apochromatically corrected should be used. The numerical aperture (NA) of an objective lens is a measure of its ability to collect light and resolve fine object details. The higher the NA is, the better the resolution of an objective is. After passing a pinhole, the light intensity is detected by a photodetector, such as a photomultiplier tube. The corresponding signals are recorded by a computer. The out-of-focus light is obstructed, as schematically shown by the dotted grey blue line in the setup image. Most of the returning light is blocked by the pinhole, which gives rise to sharper images and permits one to obtain images of planes with selective depths. Information from different focal planes can be collected through raising or lowering the microscope stage or objective lens. Consequently, the computer can generate a three-dimensional image by assembling a stack of these two-dimensional images from successive focal planes.

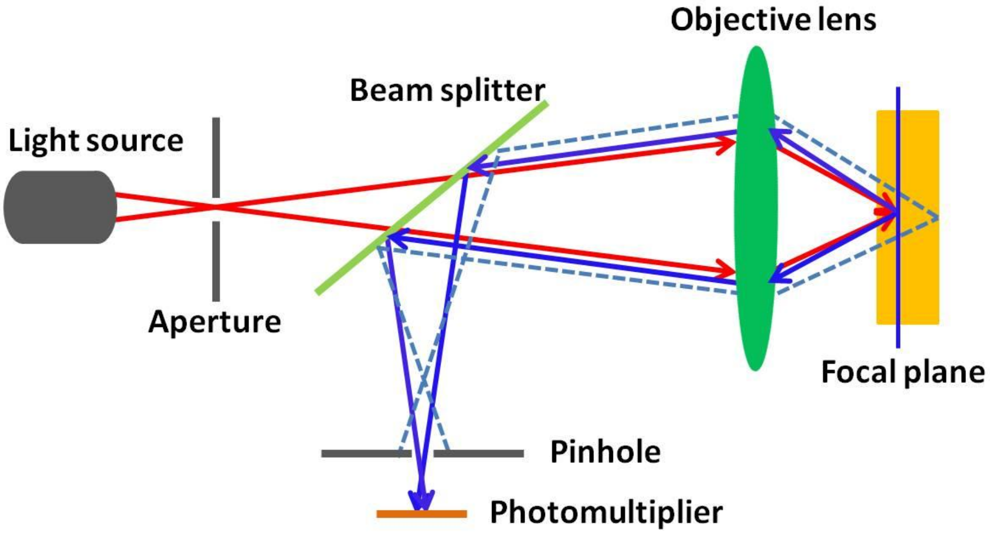

Figure 3.9 Setup of confocal laser scanning microscopy.

3.4.3 Nonlinear optics measurement system

SHG is detected by a home-made femtosecond (fs) pulse laser system. Generally speaking, SHG can be detected by pulse laser with high power intensity. Figure 3.10 shows the experimental setup of this measurement system. The fundamental pulse with an angular central wavelength of 800 nm and pulse length of 150 fs is obtained from a Ti:sapphire laser. The laser power also can be tuned by an optical attenuator. A beam splitter is used to split the fundamental laser in two. One half of the incident light is reflected to excite the sample and the other half is transmitted to be measured by a power meter to determine the laser power. The pulse laser can be tightly focused to a spot size of 1μm by a microscope objective lens. The SHG information is collected by reflection. A set of color filters is used to block the fundamental and other unwanted light. The collected signal is detected by a spectrometer.

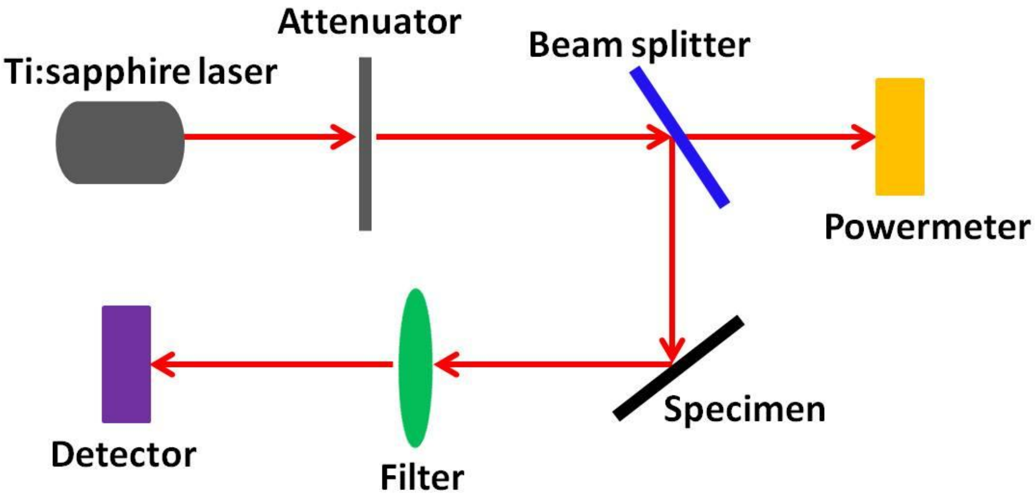

Figure 3.10 Experimental setup of the nonlinear optics measurement system.

Chapter 4 Transport and Vibrational Properties of Graphene on PMN-PT

4.1 Introduction

Ferroelectric materials have been employed in GFETs by using ferroelectric materials as gate dielectrics for memory applications.[119] The switchable polarization (effectively resulting in stored charge) can be utilized as the means of storing information, which offers ferroelectrics the opportunity to be as promising nonvolatile alternatives. However, fascinating characteristics of GFeFETs have been typically ascribed to extrinsic charging effects such as surrounding molecules charge injection into interfacial states, and/or trapped charge redistribution at the interface.[27,28] And n-type graphene FETs in air ambient conditions is still desirable. Accordingly, various efforts have been devoted to access an n-type graphene.[120,121] Very recently, graphene FETs by PZT gating exhibited a complete conversion of a p-type graphene into n-type through ferroelectric polarization reversal.[122] However, such complete reversal from p- to n-type graphene FETs is obtained in vacuum conditions. Furthermore, it is reported that large-area graphene can reach a high carrier doping level by organic ferroelectric PVDF-TrFE poling, yielding a low sheet resistance in air ambient conditions.[123,124] This makes graphene show potential for the use in conductive and flexible electrodes to substitute traditional transparent ITO. Although some approaches have been proposed to reduce resistance of graphene, such as chemical doping,[125] such methods can generally induce the degradation of conductivity of chemical-doped graphene[126,127] by the adsorption of moisture and introducing other chemical molecules.[128,129] In comparison to this chemical approach to reduce the resistance of graphene, coupling with ferroelectric can rule out the possibility of chemical doping. The graphene hybrid systems with flexible PVDF-TrFE[29,124] or PZT thin film[130] have ever been investigated, while little studies have been reported about other ferroelectric materials. For instance, PMN-PT not only exhibits outstanding converse piezoelectric response, but also possesses attractive ferroelectric characteristics, suggesting the possibility of practical use for memory devices.[56,57] Therefore, it is interesting to investigate the effects of electric field on the transport properties of graphene and the expected nonvolatile behaviors of the corresponding GFETs by the ferroelectric gating of PMN-PT.

Large-area single-layer graphene is a gapless semi-metal, which becomes one of the major challenges when using graphene-based devices in practical applications.[17] Accordingly, various efforts have been devoted to access a tunable band gap in graphene, such as reducing large area graphene in one dimension to form graphene nano-ribbons, applying large bias voltage to bilayer graphene and by strain engineering.[32,33] Among them, strain engineering is proposed to induce a gap in graphene. Typically, large strain in excess of 20% is needed.[34,35] Nevertheless, strain engineering on graphene is very essential to study the fundamental properties of graphene. It is very convenient to provide uniaxial strain to graphene by stretching or bending the underlying flexible substrate where graphene is transferred. The flexible substrates generally are polymers, including polydimethylsiloxane (PDMS),[131] PMMA[132] and polyethylene terephthalate (PET),[133,134] and so on. Such uniaxial strain is typically, for example, not equal in x and y directions, giving rise to the shift of the relative positions of the Dirac cones, and further inducing significant influence on the double-resonance process of graphene. Thus, the uniaxial strain is not suitable for investigating the fundamental properties of graphene, such as Grüneisen parameters.[61,62] Beyond uniaxial strain, another type of homogeneous strain named biaxial strain can induce equal deformation in in x and y directions. Therefore, it is very interesting to study the strain effects on graphene experimentally by introducing biaxial strain into graphene in a controllable manner.

It has been proven to be feasible to utilize biaxial strain to study the basic vibrational properties of graphene.[135,136] Indeed, Besides, Zabel *et al*. and Lee *et al*. used graphene balloons on SiO_2 substrate to study Raman spectroscopy of graphene under biaxial strain and then to calculate Grüneisen parameters and Young modulus, respectively.[135,136] Besides, it is viable to provide biaxial strain to graphene by exerting an external electric field to the underlying piezoelectric material.[59]

The ferroelectric PMN-PT is also an excellent material which is capable of providing large strain due to its giant electromechanical or converse piezoelectric response.[137,138] In our recent study, both light and ultrasound emissions have been observed in a single system of ZnS: Mn/PMN-PT.[139] The substrate-induced strain as well as the piezoelectric potential can dramatically change the interface charge and affect the electrical properties of the as-prepared materials. Such piezoelectric strain is different from the above mentioned uniaxial strain produced by stretching or bending the polymer. It was reported that biaxial strain can induce more remarkable changes in band structure compared to unixial one. For example, the dramatic increase in band gap and the enhanced PL for trilayer MoS_2 under compressive biaxial stran.[140] Additionally, previous studies of biaxial strain are mainly focused on the mechanically exfoliated graphene. CVD-synthesized graphene are usually large-area and continuous, which will be of great interest for industrial scale applications. Therefore, it is worth investigating biaxial strain effects on CVD-grown graphene tuned by the external voltage applied to the PMN-PT crystal in reversible and real-time manners.

In this chapter, the graphene layer prepared by CVD method has been directly transferred onto PMN-PT substrates to fabricate graphene/PMN-PT hybrid structure. This provides us an opportunity to study the transport properties of graphene based on GFeFETs. Considering the transport properties of graphene are also temperature-dependent, the temperature response of this hybrid system has been analyzed.[141] Simultaneously, it is worth noting the fact that PMN-PT crystal possesses piezoelectric properties. Based on the above mentioned hybrid structure, the PMN-PT single crystal also acts as the piezoelectric actuator to exert biaxial strain on the graphene. This strategy provides a unique approach to investigate dynamical vibrational properties of the graphene *via* piezoelectric-induced biaxial strain.[142]

4.2 Experimental

4.2.1 Fabrication of hybrid structure of graphene/PMN-PT

Chemical-vapor-deposited SLG on copper foils were transferred onto PMN-PT substrates. Before transfer process, oxygen plasma treatment was employed to enhance the hydrophilicity of PMN-PT surface, allowing the graphene and underlying PMN-PT substrate to form good adhesion. The source and drain electrodes (150 nm Au) of graphene/PMN-PT FETs were formed using the predefined shielding mask followed by a thermal evaporation process on the top surface of graphene, while gate electrode was prepared by Au coating on the backside of the PMN-PT substrate. The schematic of the graphene FET by 0.5 mm-thick PMN-PT gating is shown in Figure 4.1. The channel length and width of the device was 100 μm and 2 mm, respectively. For comparison, we also transferred the graphene onto silicon wafers coated with 300-nm thick SiO_2 instead of PMN-PT.

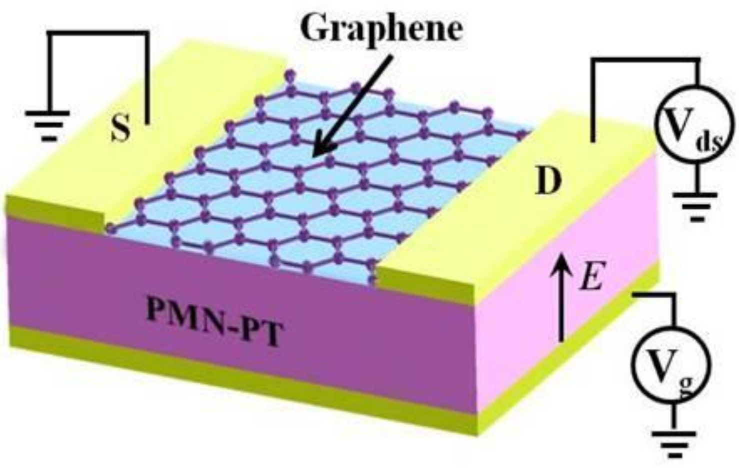

Figure 4.1 Schematic of GFET by using PMN-PT as the ferroelectric gating.

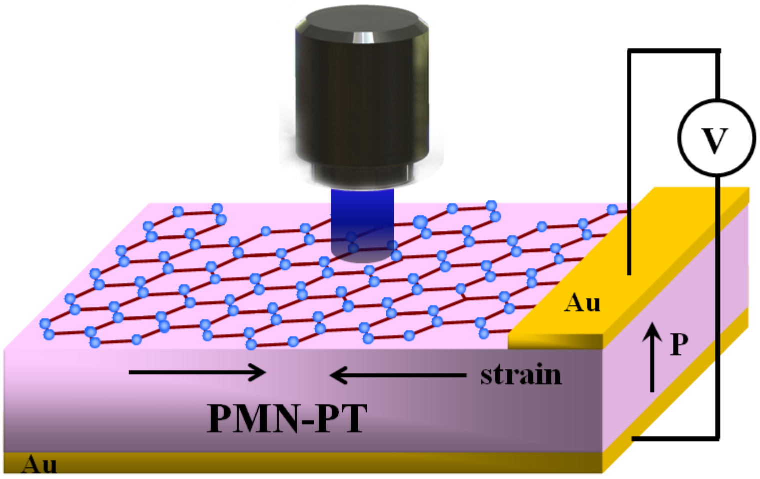

Figure 4.2 Schematic of hybrid structure of graphene/PMN-PT by using PMN-PT as a piezoelectric actuator.

Based on above mentioned hybrid structure, note that the resistance of graphene is about several kΩ, which is much smaller than that of the underlying PMN-PT. Hence, the large-area continuous graphene layer could serve as a top electrode to form the parallel plate capacitor when a bias voltage was applied to the PMN-PT. Then, the backside of the PMN-PT substrate was coated with Au to form bottom electrode. Thus, a parallel plate capacitor of graphene/PMN-PT/Au was fabricated in order to provide electric field to the piezoelectric PMN-PT. Subsequently, 150 nm-thick Au top electrodes were deposited directly on the graphene sheet by thermal evaporation for the connection between the hybrid structure and the power source. The schematic of the hybrid structure is shown in Figure 4.2 with PMN-PT as piezoelectric actuator. When a bias voltage is applied on the parallel plate capacitor, a biaxial strain can be induced by the piezoelectric PMN-PT and such strain can be used to investigate the vibrational properties of the above graphene layer.

4.2.2 **Characterization**

Atomic force microscopy (AFM, DI Nanocope 8) was employed to perform the surface morphology characterization for the graphene. The AFM images in 2D and 3D modes reveal the surface morphology of graphene on PMN-PT substrate, as shown in Figure 4.3a and b, respectively. The value of root mean square (RMS) roughness for graphene is about 0.435 nm. There are no cracks or slipping for graphene in the AFM image, indicating a flat and continuous graphene layer has been transferred onto PMN-PT substrate.

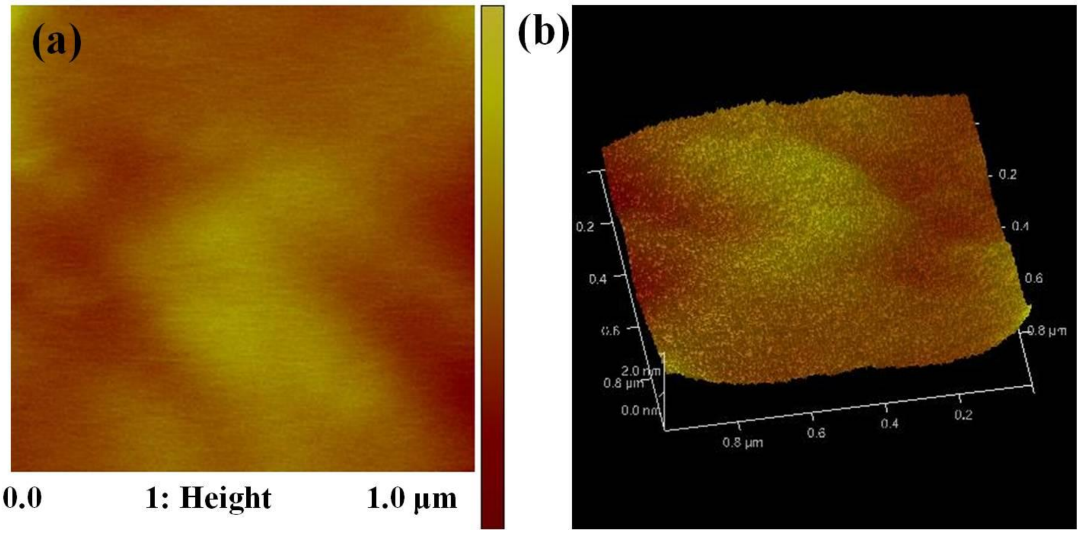

Figure 4.3 AFM image of graphene on PMN-PT substrate in (a) 2D and (b) 3D mode, respectively.

Graphene layer was detected by Raman spectroscopy (HORIBA, HR800) with the excitation wavelength of 488 nm. A 100x objective lens with NA of 0.9 was used in the measurement. The Raman mapping image over a 6 µm × 6 µm area for graphene feature peaks after transferred onto the PMN-PT substrate is shown in Figure 4.4. The most intense features of G and 2D peaks from the graphene layer can be clearly observed. The intensity at 2D peak is found to be approximately 2 times of that of G peak, indicating that the graphene is single-layer. No defect-related D peak can be detected. This confirms the high quality of the transferred graphene and the absence of significant defects in the graphene.[143] Both the AFM and Raman mapping image of graphene indicate that a uniform and continuous graphene sheet has been transferred onto the PMN-PT substrate with high quality.

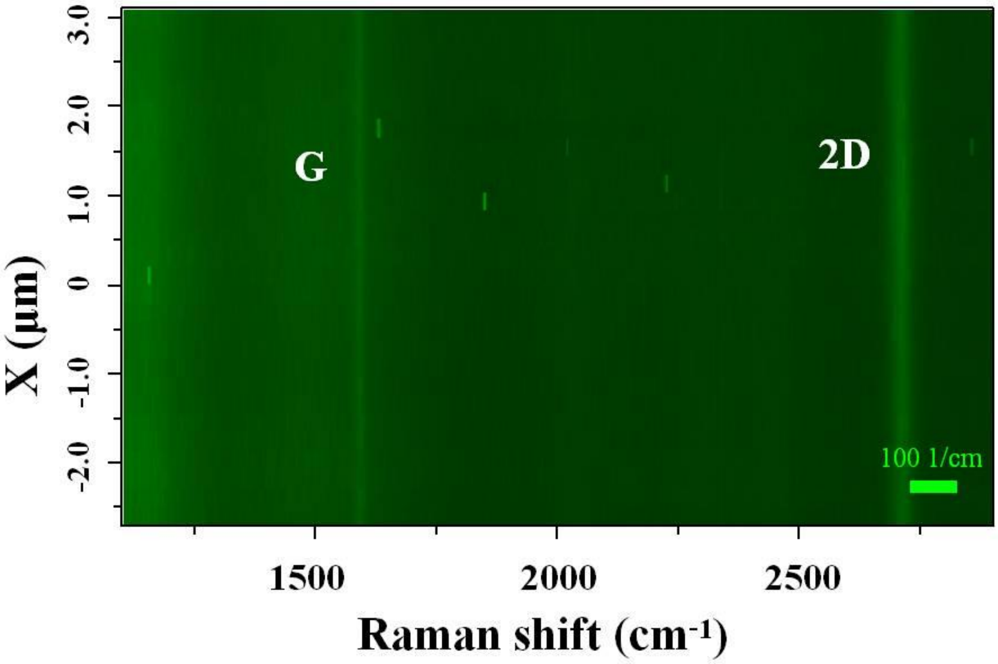

Figure 4.4 Raman mapping image of graphene feature peaks in the FET channel over a 6 μm × 6 μm area.

Four-probe measurement system was empolyed to measure the transport properties of graphene in air ambient conditions at room temperature. In this system, the Keithley 2400 and 2410 sourcemeters were used to provide source-drain voltage and the gate voltage, respectively. Temperature-dependent resistance for the sample with four-probe configuration was measured within 15-300 K using a cryogenic system (Janis CCS 150SH, Wilmington, MA). Figure 4.5 shows the real image of the graphene/PMN-PT FET devices performed by optical microscope. Wire bonding technique was employed to connect the source and drain electrodes to the printed circuit board (PCB) which can be conveniently connected to the measurement systems. Additionally, the polarization hysteresis loop was measured under an ac electric field with 10 Hz using a conventional Sawyer–Tower circuit.

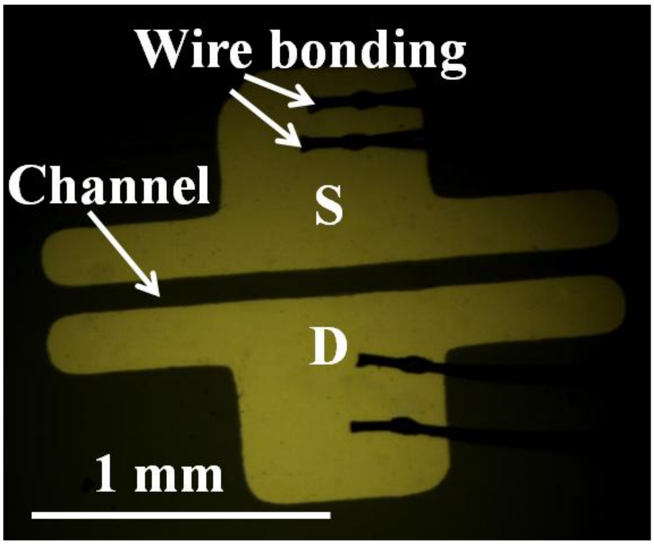

Figure 4.5 The optical image of graphene/PMN-PT FET device in top view.

High resolution X-ray diffractometer (Rigaku, SmartLab, 9 kW) equipped with a Ge (220) 2 bounce monochromator was used to get 2θ scanning patterns of the single-crystal PMN-PT. During the XRD and Raman measurements, a Keithley 2410 sourcemeter was introduced to provide gate voltage for the graphene/PMN-PT hybrid. All the above measurements were performed in air ambient at room temperature.

4.3 Transport properties of graphene/PMN-PT FETs

Next, the transport properties of the GFET by PMN-PT gating are introduced. Firstly, the drain current (I_{ds}) is analyzed as a function of the source-drain voltage (V_{ds}) as well as the gate voltage (V_g). The output characteristics (Figure 4.6) indicate a completely linear behavior with the V_g changed from –100 to 100 V, which is commonly observed for metal/zero-gap-graphene junction, suggesting a good ohmic contact between the Au electrode and the graphene sheet.

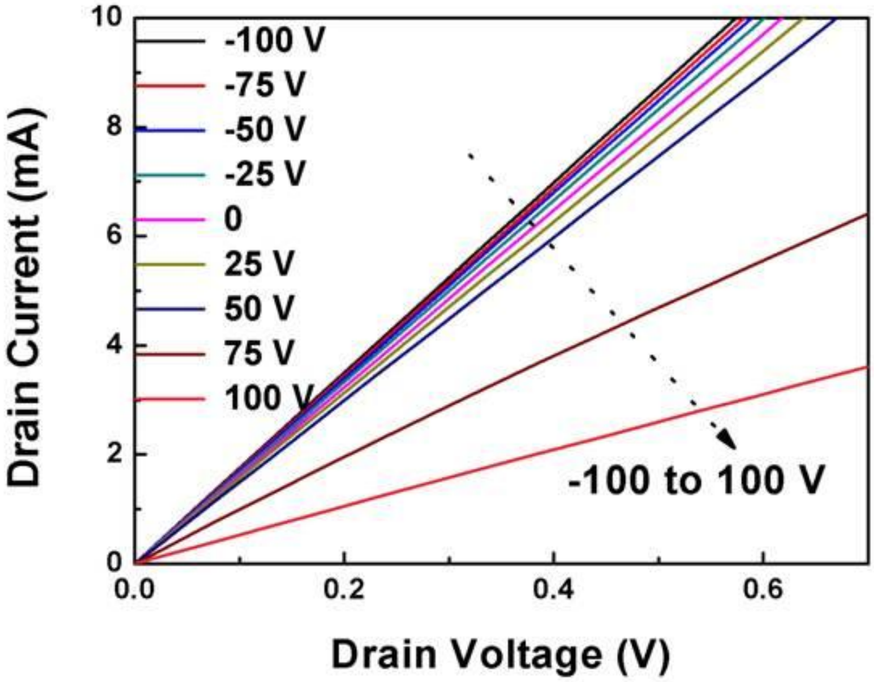

Figure 4.6 The room temperature output characteristics with the gate voltage changed from –100 to 100 V at a step of 25 V.

Then, I_{ds} is measured as a function of the V_g, as shown in Figure 4.7. The V_{ds} of 0.5 V is applied while the V_g is swept in a closed loop from $+V_{gmax}$ to $-V_{gmax}$ then back to $+V_{gmax}$, where V_{gmax} is the maximum sweep V_g. It is clear that the I_{ds} gradually decreases as the gate voltage increases from –50 to +50 V, indicating that the graphene which is fabricated by CVD and subsequently transferred onto the PMN-PT substrate is p-type. The I_{ds}–V_g curves of the graphene/PMN-PT FET show a similar pattern as the V_{gmax} increases up to 100 V. So does the graphene on conventional SiO_2 wafer, as shown in the inset of Figure 4.7. Our graphene FETs are exposed to air ambient, which are usually observed to be p-type.[144] It is known that the charge concentration of graphene on various types of substrates mainly depends on the gate voltage and the capacitance of gate insulator. The doping concentration varies in direct ratio to the dielectric constant of the insulator layer, but in inverse ratio to the insulator thickness, with the bias voltage being constant. In our experiments, the values of both thickness and dielectric constant of PMN-PT (0.5 mm, ~5000) are much greater compared to SiO_2 (300 nm, ~3.9). Thus, electric field doping effects on the graphene on PMN-PT and SiO_2 are comparable under same bias voltage. It is worth noting that the I_{ds} of the graphene on the PMN-PT is about 2 times larger as that on the SiO_2 wafer, suggesting a decrease in resistivity of the graphene on the ferroelectric substrate. Subsequently, for the V_{gmax} higher than 100 V, the I_{ds}–V_g curves exhibit anomalous behaviors. There is an abrupt transition at about ±75 V, resulting in a large memory window which should be very useful for graphene/ferroelectric memory applications. Such sharp transition corresponds to the dramatic change of I_{ds} from about 1.66 to 9.15 mA and leads to an on/off current ratio of about 5.5. When the V_{gmax} increases further, I_{ds}–V_g characteristics of the graphene show a similar loop to that with V_{gmax} = 150 V. Such V_{gmax}-independent I_{ds}–V_g characteristics might result from the saturation of ferroelectric polarization.

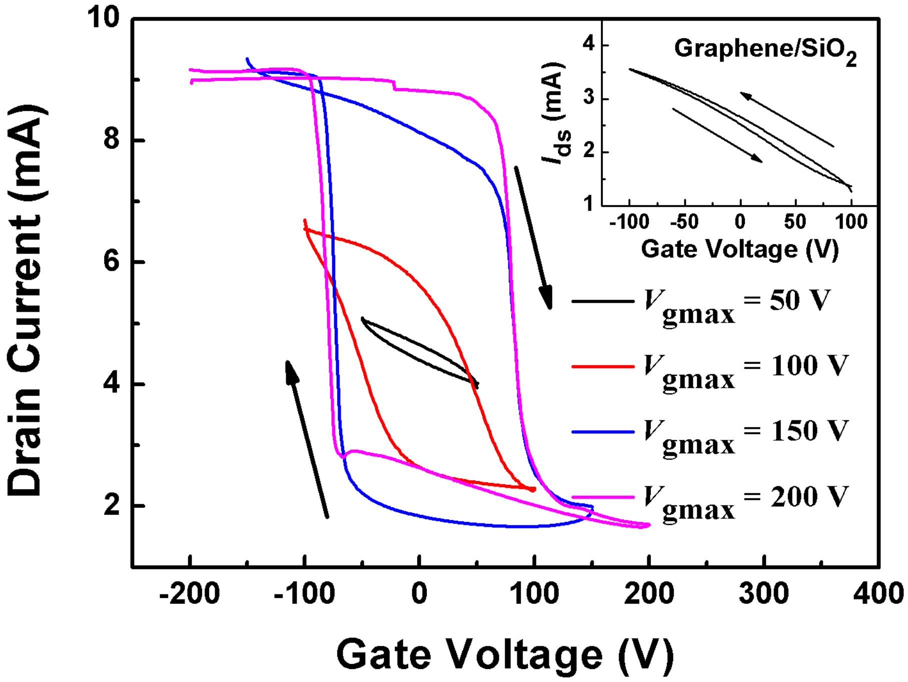

Figure 4.7 The I_{ds}–V_g curves of graphene on PMN-PT with V_{gmax} from 50 to 200 V. The inset shows I_{ds}–V_g curves of graphene on 300-nm SiO$_2$.

To explore the possible correlation between the transport properties of the graphene and the ferroelectric properties of the underlying PMN-PT, we measured the polarization versus electric field (*P*–*E*) hysteresis loop of the graphene/PMN-PT hybrid structure as shown in Figure 4.8. The coercive field of the PMN-PT with the graphene as electrode is ~200 kV/cm. Accordingly, the coercive voltage is ~100 V for the PMN-PT. While, the reversal polarization starts at around 75 V (–75 V) when the bias voltage sweeping from negative (positive) voltage, corresponding to the sharp transition of I_{ds} when the V_{gmax} in excess of coercive voltage of 100 V.

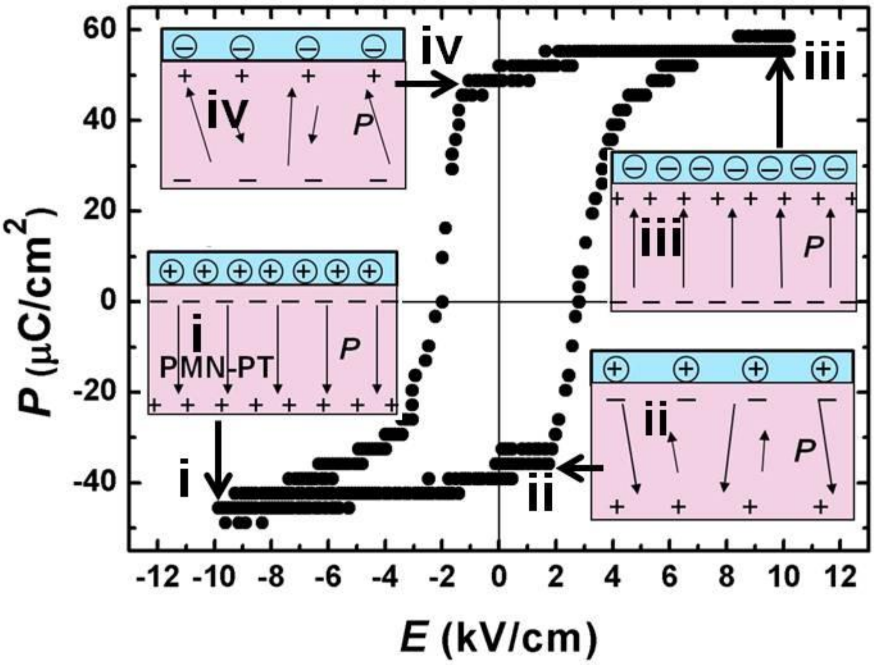

Figure 4.8 The *P*–*E* hysteresis loop of the PMN-PT single crystal with graphene as top electrode. The insets show schematic of polarization orientation of PMN-PT under different electric field, the bound charges at the top and bottom surface of PMN-PT and the hole and electron carriers in the graphene layer also have been schematically displayed.

There are positive (negative) bound charges on the top surface of the PMN-PT with an up (down) polarization as schematically shown in the insets of Figure 4.8. Furthermore, when the negative bound charge density decreases (from stage i to ii, during the sweeping voltage from negative to positive one), the hole carriers in p-type graphene decrease, resulting in the lower hole concentration and the reduced I_{ds}. On the other hand, when the positive bound charge density decreases, the electron carriers in graphene will decrease (from stage iii to iv, during the sweeping voltage from positive to negative one). For the p-type graphene, the hole doping level and I_{ds} will be effectively increased.[28,130] Specifically, at the vicinity of coercive voltage, the polarization switching occurs in the PMN-PT and the carriers in the graphene can be changed from holes to electrons (or electrons to holes), which can bring about the dramatic transition of I_{ds}.

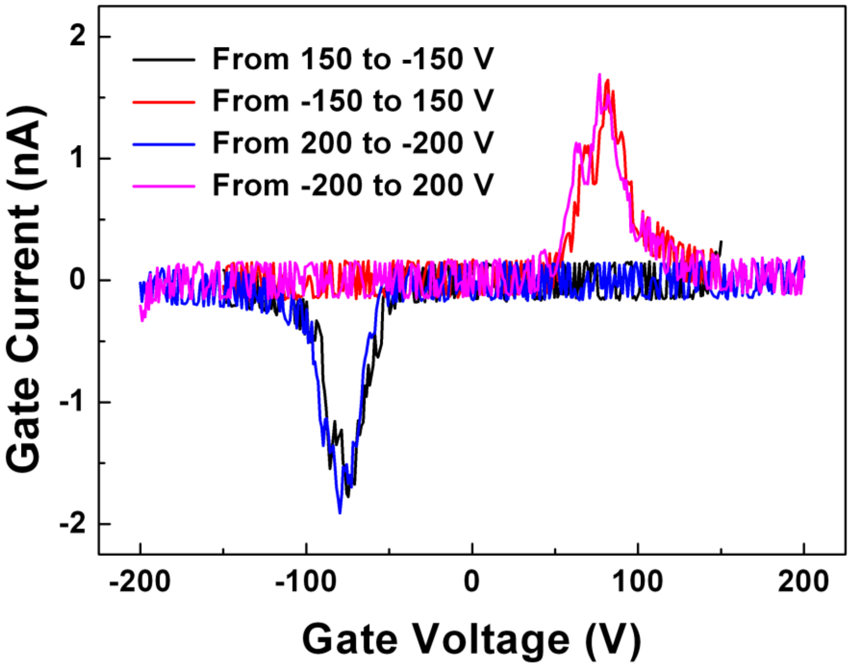

Figure 4.9 I_g–V_g curves of graphene FET with different sweeping direction and starting voltage.

From the above interpretation, it is postulated that the transport behaviors of the graphene stem not only from the extrinsic charging effects but also from the coupling of the ferroelectric polarization to charge carriers in graphene. To further verify this hypothesis, the gate current (I_g) was recorded simultaneously during the measurement of drain current as shown in Figure 4.9. The dramatic rise in $|I_g|$ reaching a maximum value at about $|V_g| = 75$ V where the reversal of ferroelectric polarization begins for the PMN-PT (as can be seen from Figure 4.8). The polarization reversal can lead to the transfer of positive and negative charges in the PMN-PT, giving rise to the increase in intrinsic current.

Figure 4.10 exhibits the first derivative of I_{ds} ($\partial I_{ds}/\partial V_g$) with different sweeping direction and starting voltage. It is clear that the non-monotonic $\partial I_{ds}/\partial V_g$ curves show identical behaviours with the I_g–V_g, implying that the I_{ds} varies precisely during the polarization switching. Such an observation of simultaneous rise in $|I_g|$ with the dramatic variation in I_{ds} ($\partial I_{ds}/\partial V_g$), can further support the conclusion that the polarization reversal is responsible for the sudden rise and drop of I_{ds}.

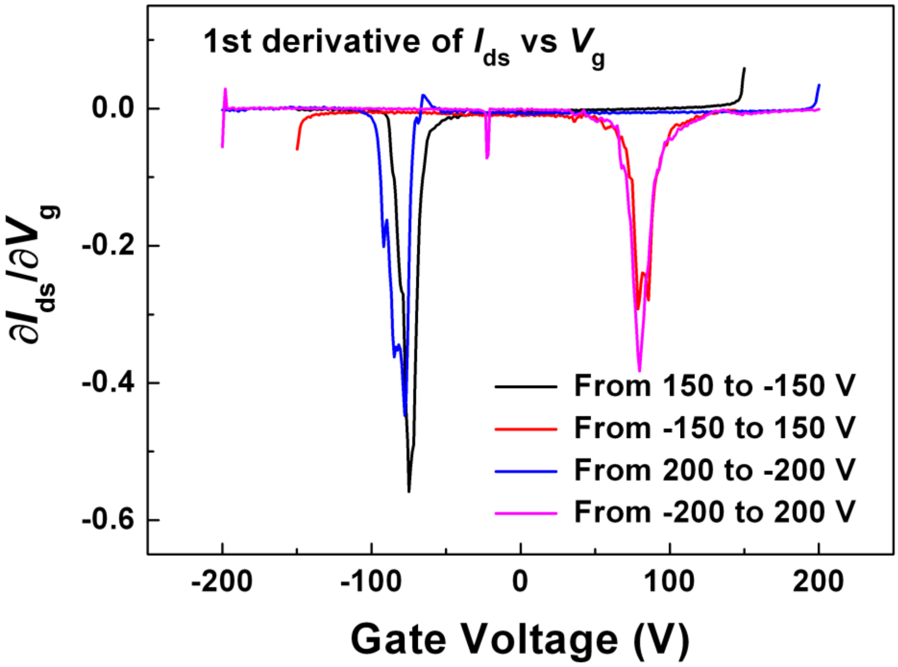

Figure 4.10 The first derivative of I_{ds}–V_g curves with different sweeping direction and starting voltage.

However, the graphene on the PMN-PT substrate still shows p-type characteristics when the V_{gmax} changed from 50 to 200 V. Although it is common for graphene FETs is p-doped in air ambient at room temperature when considering the adsorbed molecules enhancing charge trapping at the interface,[145,146] v-shape behaviors or a reduction in p-doping is expected for graphene FETs by ferroelectric gating. In our experiments, such a behavior can be realized via the pre-polarization of the PMN-PT substrate by applying a perpendicular electric field to the substrate. This approach may result in the electric dipole moments in the PMN-PT substrate pointing away from the graphene sheet (down polarization). Prior to the I_{ds}–V_g measurements, the PMN-PT substrate has been pre-poled by –500 V for 10 min to realize in the down polarization state. After that, the I_{ds}–V_g curves are measured with different initial voltage, ad shown in Figure 4.11.

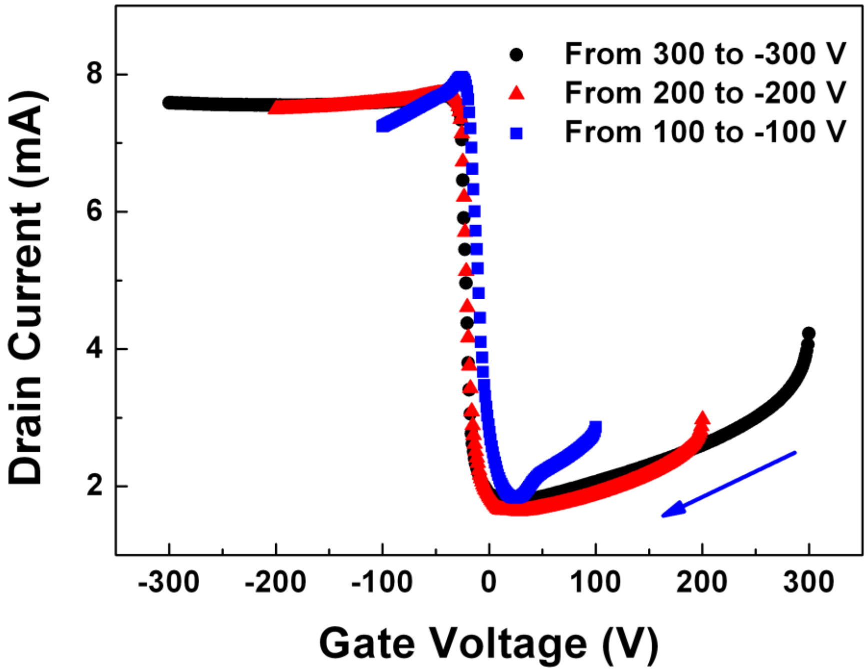

Figure 4.11 I_{ds}–V_g curves of graphene FET by pre-poling and swept from different

initial voltage from 100 to 300 V.

Based on this I_{ds}-V_g curve with V_g starting from 100 V, the excess hole concentration ($n_{\text{ex-h}}$) can be calculated as:

$$n_{\text{ex-h}} = \frac{\varepsilon_0 \varepsilon_r}{e d_{ox}} \Delta V_{\text{Dirac}} \tag{4.1}$$

where, ε_0 is the dielectric constant of vacuum, ε_r is the dielectric constant of PMN-PT (5000), e is the electronic charge (1.602×10^{-19} C) and d_{ox} is the thickness of the insulator (0.5 mm for PMN-PT). The excess hole concentration can be calculated to be about 6.74×10^{12} cm^{-2}. Besides, field effect mobility ($\mu_{\text{e,h}}$) can be calculated as:

$$\mu_{\text{e,h}} = \frac{L}{W C_{ox} V_{ds}} \frac{\Delta I_{ds}}{\Delta V_g} \tag{4.2}$$

where L (100 μm) and W (2 mm) are the length and the width of the FET channel, respectively. C_{ox} is the gate oxide capacitance. $\Delta I_{ds}/\Delta V_g$ is the transconductance in the linear regime of the I_{ds}-V_g curve. Then the mobility of graphene gated by PMN-PT is estimated to be about 4.52×10^3 cm^{2}v^{-1}s^{-1}. For the graphene on SiO_2 substrate, the comparable hole concentration can be derived, while the mobility is just about 110 cm^{2}v^{-1}s^{-1}. Similar improvement in the mobility of graphene has also been reported for graphene on PZT.[27,30]

When an initial positive voltage (larger than coercive voltage) is applied to the PMN-PT, the dipole moments can be re-oriented (pointing to the graphene layer and PMN-PT in the up polarization state). Once such a positive voltage is applied to the

PMN-PT in the down polarization state, the reversal of ferroelectric polarization (from down to up state) can be obtained in the PMN-PT. The polarization switching can be characterized by the sudden drop of I_g at initial sweeping voltage shown in Figure 4.12 when the V_g starting from 100, 200 or 300 V. The initial high current is resulted mainly from the polarization switching. Accordingly, the polarization switching can lead to the variation of I_{ds}. As discussed in the text for Figure 4.8, the polarization from down to up state can induce the carriers in graphene to change from holes to electrons, resulting in a reduction of p-doping for graphene. Then, as the sweeping voltage decreases, the electron density and I_{ds} decrease, simultaneously. As a consequence, the positive Dirac point shows a left shift to 22 V (or 16 V) when V_{gmax} = 100 V (or 300 V). And the larger initial voltage can lead to a smaller Dirac point. This may be caused by the absolute polarization reversal for the PMN-PT under bias voltage larger than coercive voltage. This Dirac value is relatively small considering the thickness of PMN-PT (0.5 mm). After that, the I_{ds} increases dramatically due to the reversal of polarization corresponding to the sharp change of I_g at about –25 V. Figure 4.13 exhibits the first derivative of I_{ds}, showing identical curve of I_g–V_g. The polarization reversal gives rise to the sudden change of I_g at the initial period of sweeping and around –25 V, where I_{ds} changes quickly. This result further verifies the pre-polarization and polarization reversal of ferroelectric PMN-PT play an important role in the I_{ds} behaviors and the improvement in the mobility of graphene.

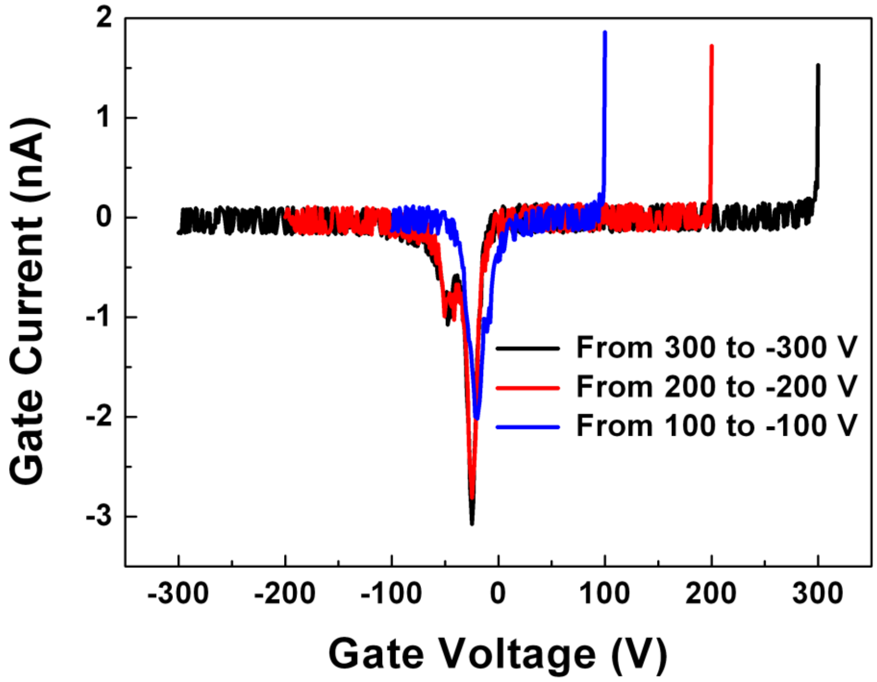

Figure 4.12 The I_g–V_g curves measured after pre-poling PMN-PT by a bias of –500 V for 10 min and swept from different initial voltage.

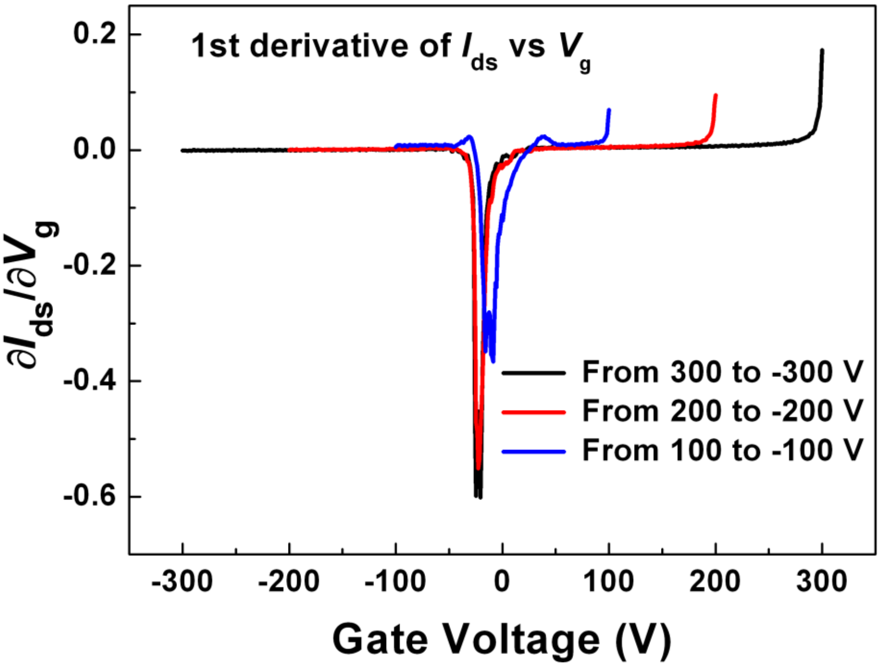

Figure 4.13 The first derivative of I_g–V_g curves with initial voltage of 100, 200 and 300 V after pre-poling PMN-PT.

The temperature-dependent resistivity in suspended graphene sheets increases linearly with temperature from 50 to 240 K with the carrier density tuned to finite values by an applied gate voltage.[147,148] Typically, it is agreed that the carrier mobility in suspended graphene is governed by out-of-plane flexural phonons. On the other hand, for non-suspended graphene (placed on a substrate), the temperature characteristics is affected not only by the quasi-periodic nano ripples in CVD graphene,[27] and the substrate induced optical phonon scattering,[28,29] but also by the electron–acoustic phonon scattering.[30,31] However, the T-dependent behaviors exhibit a strong dependence on the substrate.[32] While, few studies have been reported on the temperature response of the behaviors for graphene on ferroelectrics. Only graphene on PZT thin film was characterized as a function of temperature until now.[30] So it is essential to study the T dependent properties of graphene on PMN-PT substrate. Figure 4.14 shows the sheet resistance R_s (V_g, T) of graphene on PMN-PT substrate versus temperature T from 15 to 290 K, with different gate voltage applied to the substrate. Similarly to graphene on SiO_2 and PZT, graphene on PMN-PT shows an increased trend as the temperature increases to 290 K, indicating a metallic character rather than a semiconductor one. The metallic characteristics of graphene can be obtained at high doping level due to the etching and transfer processes where heavy chemical doping is introduced. [53] It is also noted that, without bias voltage, the R_s exhibits a nearly linear rise at temperatures above ~150 K, while there are fluctuations for R_s at low temperature. The fluctuated R_s without bias voltage mainly caused by carrier-density inhomogeneity induced by the potential of charged impurities for low charge-carrier densities.[153,154] Graphene on SiO_2 also shows fluctuated resistivity at low temperature with low carrier density.[155,156]

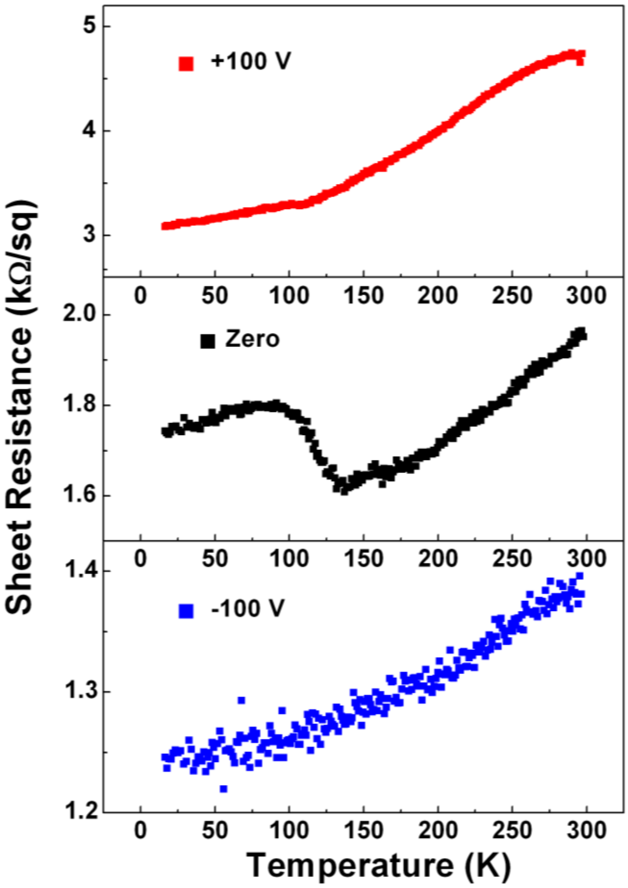

Figure 4.14 Temperature dependence of the sheet resistance for graphene on PMN-PT substrate tuned by the voltages of 100, 0 –100 V, respectively.

By tuning the gate voltage to control the carrier density, the resistance of the graphene was investigated as a function of temperature with different carrier density. For the graphene under ±100 V, the R_s is linearly increased when the temperatures are above ~120 K, and below 120 K, R_s still shows a linear increase with a relative low slope (compared with higher temperature). In our experiment, the resistance shows strong dependence on the bias voltage (carrier density), i.e. the linear increases of R_s exhibit different slopes under different bias voltages. For a positive bias voltage, the R_s has large slope compared to zero and negative voltage biased graphene, but in contrast, weak temperature dependence is observed for a negative bias voltage. The change rate of the R_s under the -100 V bias is not in excess of 10% from 15 to 290 K as shown in Figure 4.15.

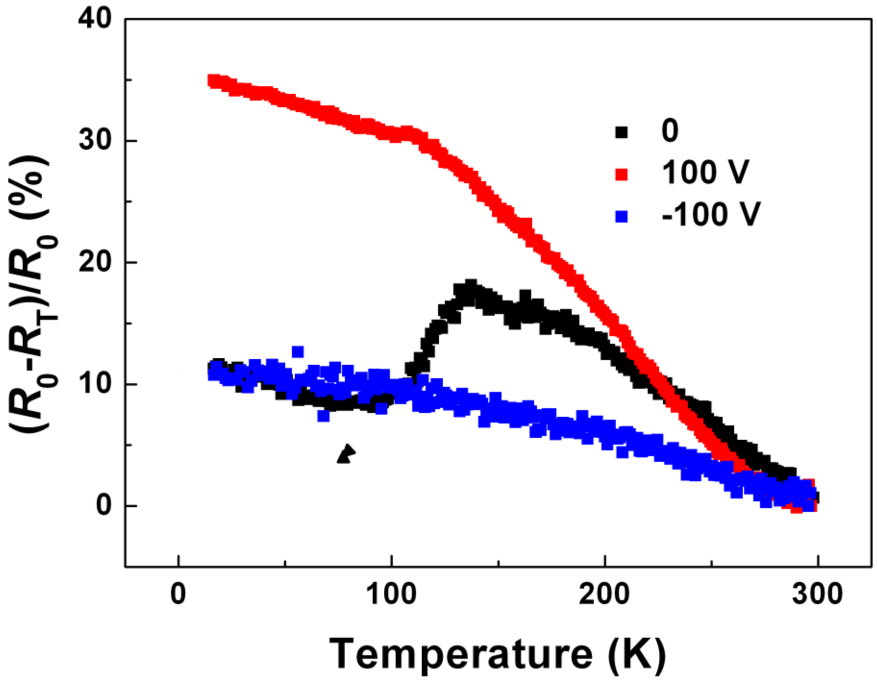

Figure 4.15 The change rate of sheet resistance as a function of temperature under different bias voltage.

4.4 The biaxial strain effects on Raman spectra of graphene

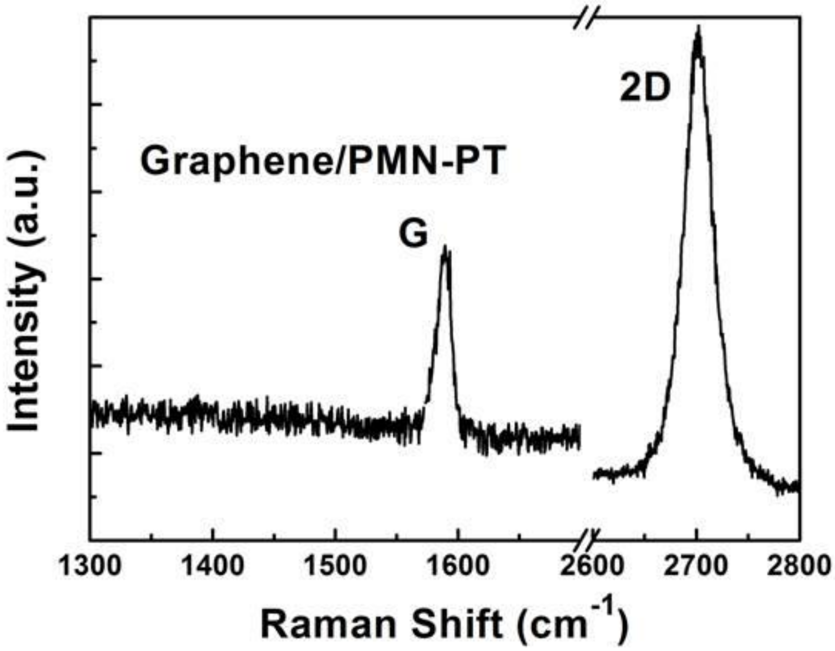

Figure 4.16 Raman spectrum of SLG graphene on PMN-PT substrate with feature peaks of G and 2D mode.

The Raman spectrum of graphene on the PMN-PT substrate is shown in Figure 4.16. Prior to the measurements of vibrational properties of graphene under strain, we positively polarized the PMN-PT substrate by applying an electric field of 10 kV/cm to the substrate, resulting in the electric dipole moments in the PMN-PT substrate pointing towards the graphene sheet. The most intense features of G and 2D peaks, corresponding to the doubly degenerate E_{2g} phonon at the Brillouin zone center and the second order of the D peak respectively, can be clearly observed. A symmetric and sharp 2D peak lies at about 2700 cm^{-1}, with full-width-at-half maximum (FWHM) of about 40 cm^{-1}. The intensity of the 2D peak is found to be approximately 2 times of that of the G peak, indicating that the graphene is single-layer.[143] No defect-related D peak is observed, confirming the absence of significant defects in the graphene sheet.

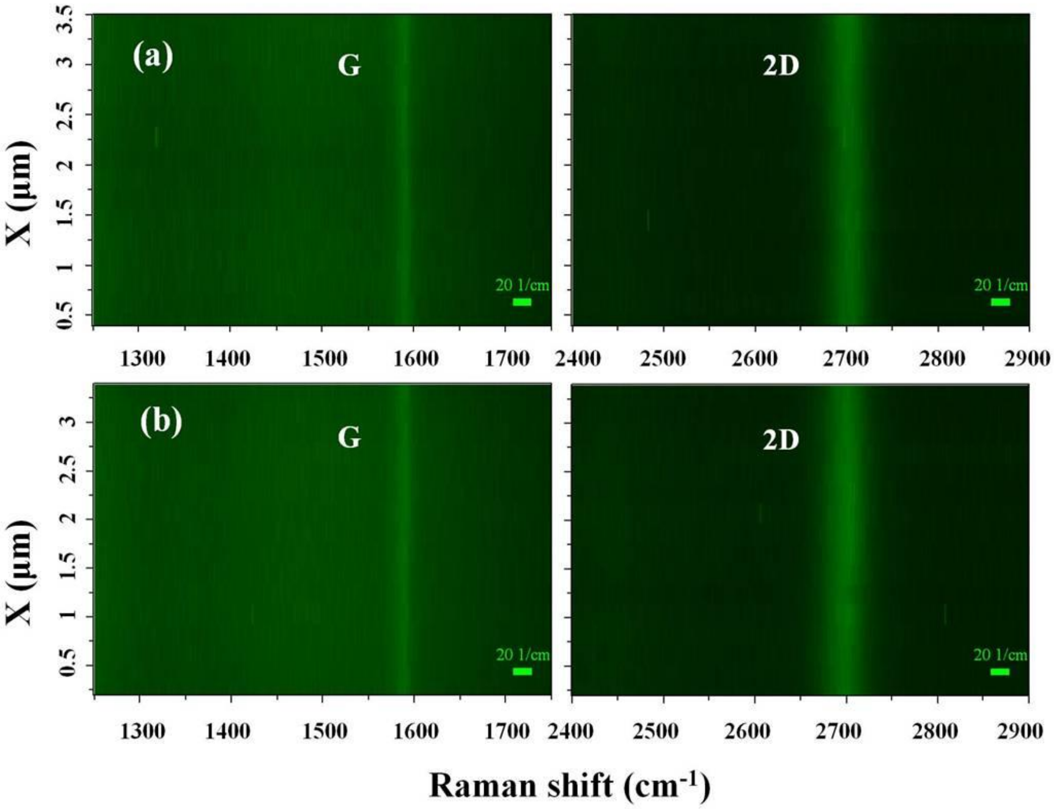

Figure 4.17 Raman spectra mapping images of feature peaks of graphene before (a) and after (b) the voltage (500 V) is applied to the PMN-PT substrate.

The mapping images of Raman spectra in terms of both position and intensity from graphene feature peaks are obtained before and after the strain is applied to the graphene, as shown in Figure 4.17a and b, respectively. The defect-related D band is still invisible after removing the strain, which rules out the possibility of slipping or buckling after strain is applied to graphene sheet. Figure 4.18 shows the two-dimensional Raman mapping of 2D band intensity of graphene. The mapping images reveal a uniform and continuous graphene flake has been transferred onto the PMN-PT.

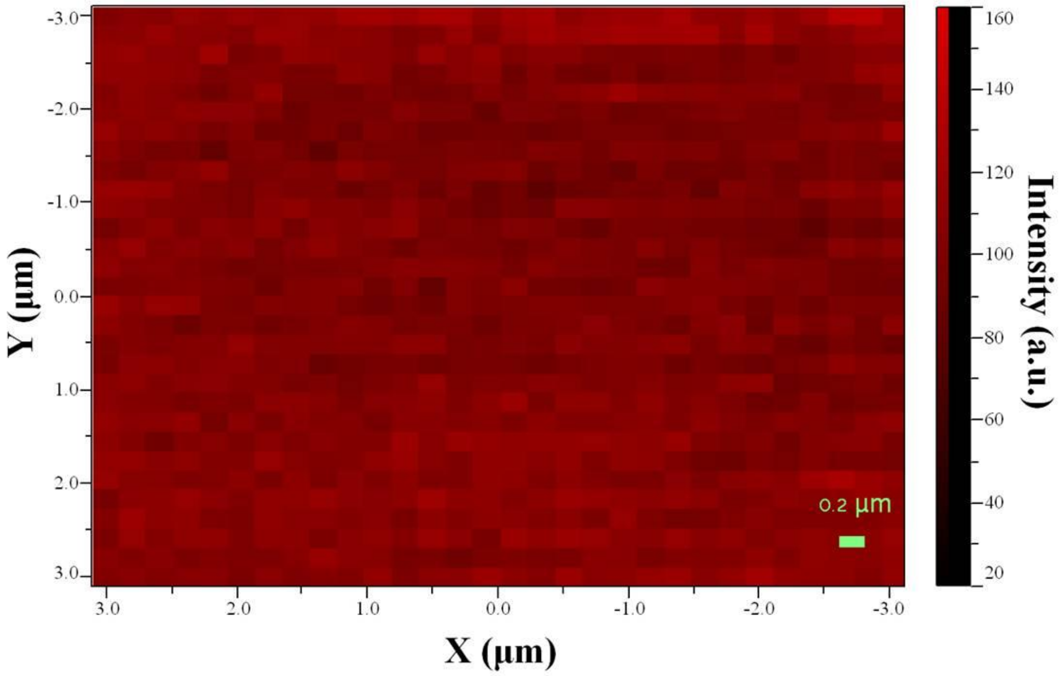

Figure 4.18 Two-dimensional Raman mapping image of 2D band intensity over a 6 μm × 6 μm area of graphene on PMN-PT substrate.

To fully understand the strain arising from the underlying substrate, XRD technique was used to analyze the lattice deformation of PMN-PT. As shown in Figure 4.19, the (002) diffraction peak of PMN-PT shows a visible shift when the hybrid structure is applied by dc voltages, and more importantly, with increasing the applied voltage, the (002) peak shifts towards lower angles. The inset of Figure 4.19 shows the position of (002) peak of PMN-PT as a function of the applied voltage. Evidently, the PMN-PT substrate can produce out-of-plane tensile strain. In other words, the in-plane strain is compressive. According to the Bragg's law and Poisson ratio, the in-plane strain can be calculated.[157]. The substrate-induced strain has a linear dependence on the bias voltage with a slope of –0.04% per 100 V.

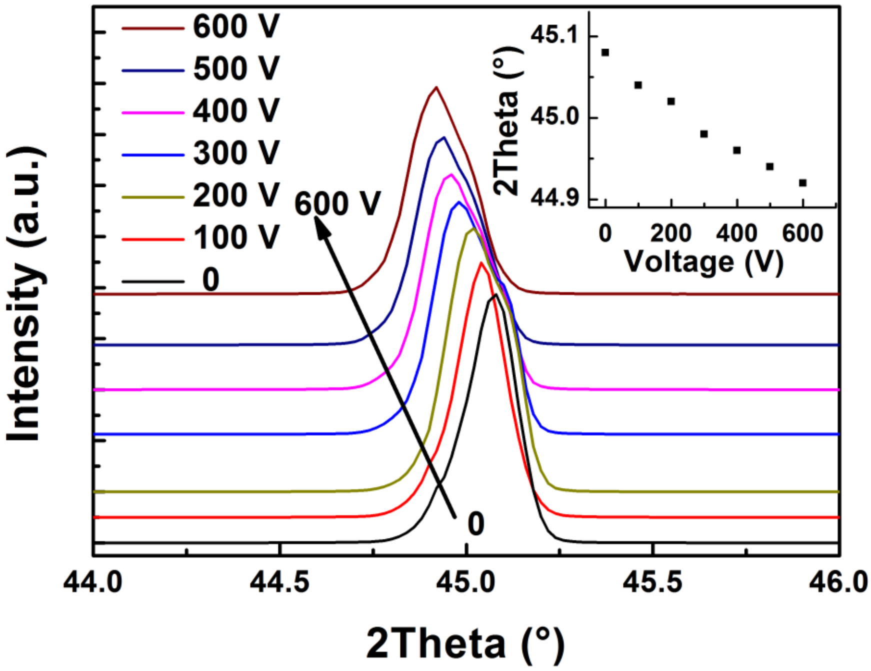

Figure 4.19 The PMN-PT (002) peaks of XRD 2θ scanning patterns with bias voltage changed from 0 to 600 V. The position of (002) peak at different voltage is shown in the inset.

Figure 4.20 shows the 2D peaks of the graphene shift to higher frequency as the applied voltage increases from 100 to 600 V. This shift in Raman peak is usually caused by the distortion of the graphene lattice, which can alter the vibrational properties of the phonons within the lattice. The 2D band shift ($\Delta\omega_{2D}$) is exhibited as a function of the applied strain in the inset of Figure 4.20. Typically, compressive biaxial strain leads to a phonon hardening (blue shift) for single-crystal graphene, while tension leads to phonon softening (red-shift).[59,135] In our experiments, the 2D peaks show blue-shifted characteristics under compressive strain, which is consistent with mechanically exfoliated graphene.

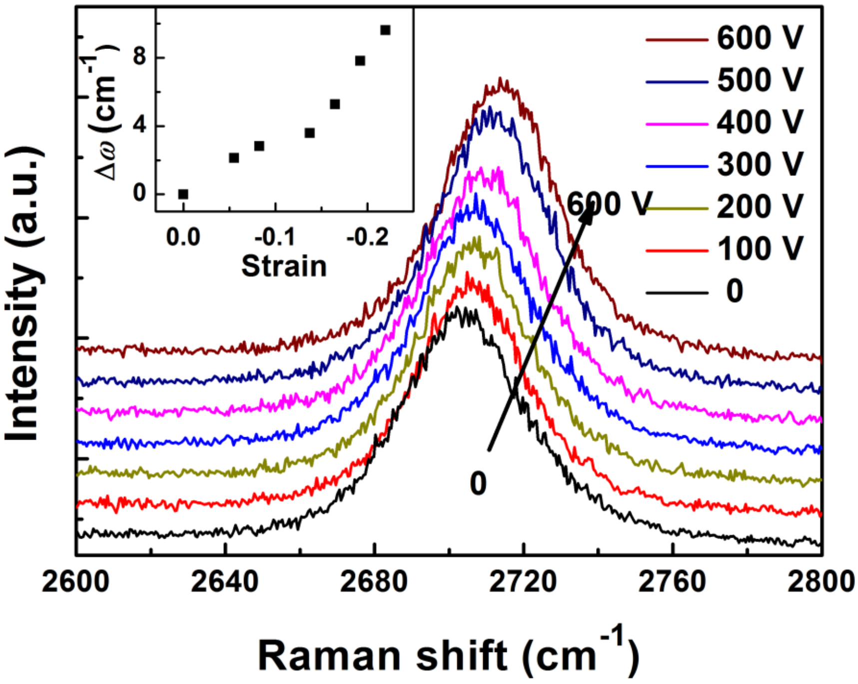

Figure 4.20 2D peaks of graphene under different bias voltage varied from 0 to 600 V. Inset shows the shift of 2D band as a function of voltage.

Negative voltages also give rise to the left shifts of (002) peaks in the XRD patterns shown in Figure 4.21. The left shifts of the diffraction peak under negative bias voltage indicate a compressive strain is produced, which is consisted with previous reports.[158,159]. Similarly to the positive bias voltage, such compressive strain also gives rise to the blue shifts of 2D Raman band. As shown in Figure 4.22, the 2D band exhibits blue shifts from 2703 gradually to 2714 cm^{-1} when the bias voltage changed from 0 to –500 V.

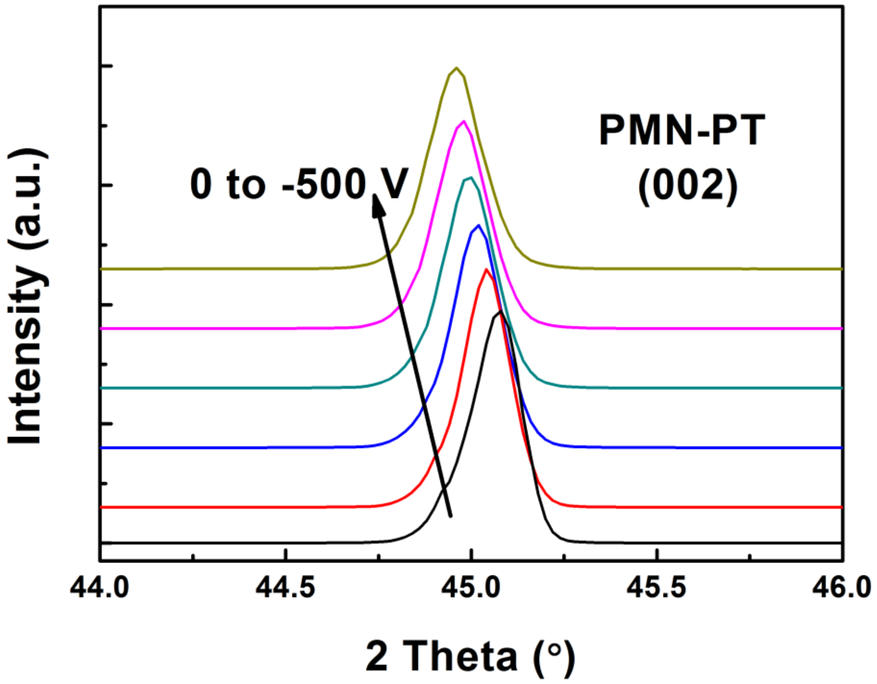

Figure 4.21 The PMN-PT (002) peaks of XRD 2θ scanning patterns with bias voltage changed from 0 to –500 V.

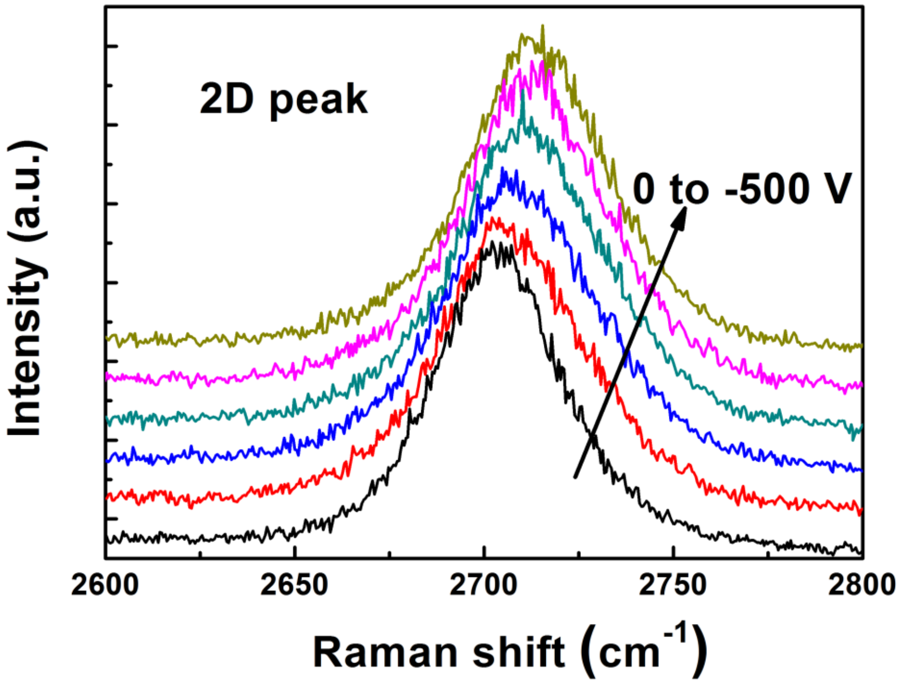

Figure 4.22 The Raman spectra of graphene 2D peaks with bias voltage varied from 0 to –500 V.

The 2D peaks of the graphene flake shift to higher frequency as the applied voltage increases, as shown in Figure 4.23. However, both the intensity and the FWHM of 2D peak show weak dependence on the applied voltage. In fact, the positions of Raman feature peaks are also carrier dependent. Earlier studies reported that carrier doping can usually lead to the decrease in intensity of 2D band and line broadening in 2D peak, accompanied by the low ratio (usually less than 1) of $\Delta\omega_{\mathrm{2D}}/\Delta\omega_{\mathrm{G}}$ ($\Delta\omega_{\mathrm{2D}}$ is the shift of 2D band frequency, while $\Delta\omega_{\mathrm{G}}$ is the shift of G band) [160]. As shown in Figures 4.20 and 4.22, the 2D peaks of the graphene show a blue shift as the applied voltage increases, while both the intensity and the FWHM of 2D peak show weak dependence on the applied voltage.

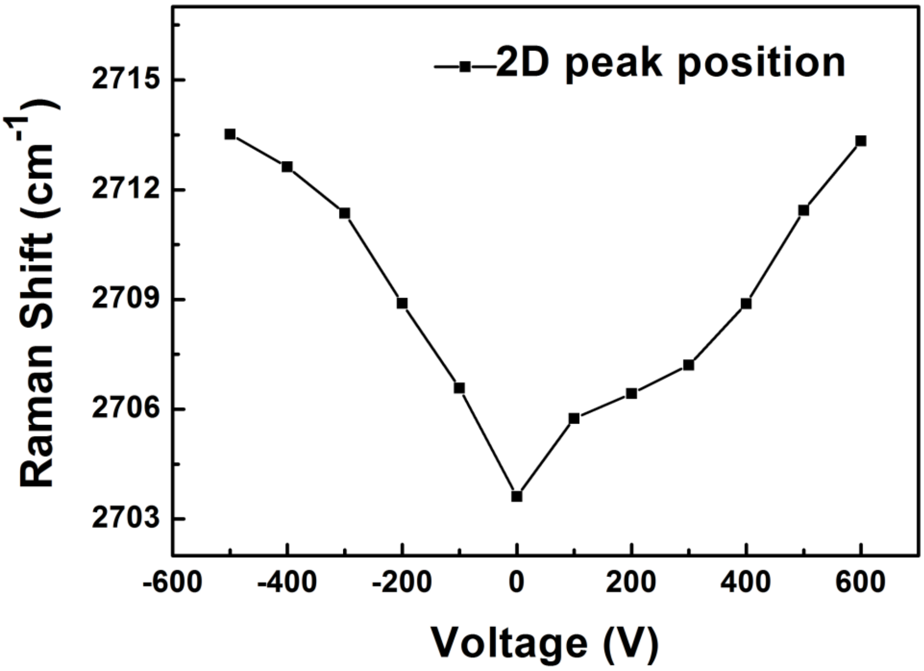

Figure 4.23 The voltage-dependent 2D peak position with bias voltage varied from –500 to 600 V.

In addition, 2D peak shift is over 2 times more than G peak shift under the same bias voltage, as shown in Figure 4.24. Furthermore, the position of the 2D peak calculated through density functional theory (DFT) framework does not change much even at high hole doping level (hole density of 10^{13} cm^{-2}). In fact, the carrier concentration is relatively low considering the thickness of PMN-PT is 0.5 mm. Besides that, the 2D band position shows a V-shape curve as a function of the bias voltage in our experiments as shown in Figure 4.23, which is in conflict with the 2D band shift behaviors induced by carrier doping. Generally, the decrease in intensity and line broadening in 2D peak were caused by such carrier doping and the ratio of $\Delta\omega_{2D}/\Delta\omega_{G}$ is usually less than 1.[160] Thus, the bias voltage-dependence of the 2D peak in our experiment mainly arises from substrate-induced compressive strain.

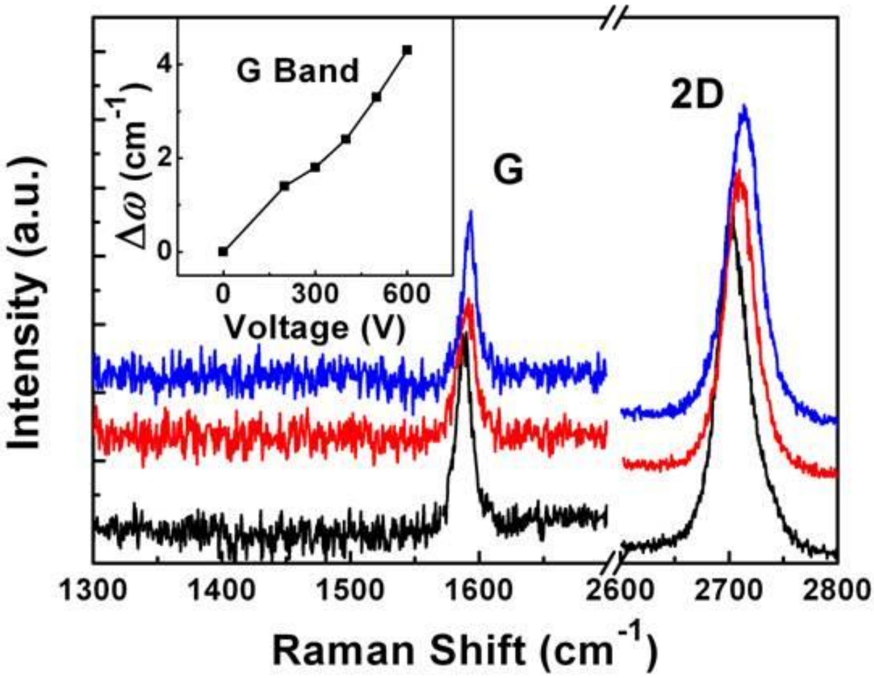

Figure 4.24 Raman spectra of G and 2D peaks for graphene under different bias

voltage. The inset shows the bias voltage dependent G band shift.

As shown in Figure 4.20, the 2D peak shifts towards higher frequency by about 1.5 cm^{-1} because of the in-plane strain induced by a bias voltage of 100 V. Then, by using the Grüneisen parameter (γ), we can estimate the strain applied to the graphene. The Grüneisen parameter is defined as:

$$\gamma = -1/(2\omega_0)\, \partial\omega/\partial\varepsilon \tag{4.3}$$

where ω_0 and ω are Raman frequencies at zero strain and finite biaxial strain, respectively. ε is the biaxial strain. Here, the $\Delta\omega$ can be expressed as:

$$\Delta\omega_{2\mathrm{D}} = -2\omega_0\gamma_{2\mathrm{D}}\varepsilon \tag{4.4}$$

In this work, the CVD-grown graphene is polycrystalline, and its mechanical properties are different from those of the single-crystal graphene because of the former consisting of grain boundaries.[161,162] Theoretical analysis indicates that strain is distributed homogenously inside polycrystalline graphene grains while strain is increased in the grain boundaries. However, the 2D band is affected only by strain inside of the grains.[163] Thus, the Grüneisen parameter for 2D band derived from mechanically exfoliated graphene can be applied to the CVD-grown polycrystalline graphene.[164] We take the Grüneisen parameter for 2D band derived from the shift of Raman peak by Zabel et al to be 2.6 ± 5%.[59,135] This value is in good agreement with the Grüneisen parameter (2.7) calculated from first principles by Mohiuddin *et al*.[61] Herein, we obtain the actual strain applied to the graphene to be about – 0.011% per

100 V bias voltage (or 2D peak shift to be about 1.5 cm^{-1} per biaxial strain of –0.011%). And this strain is the homogenous strain distributed inside the grains. Unfortunately, such strain magnitude is much smaller than that of the PMN-PT (–0.04%) based on the aforementioned XRD result. It suggests that the piezoelectric-induced in-plane strain might have not been completely transferred to the graphene sheet. This may be attributed to the extremely high stiffness of graphene and the inefficient interfacial strain transfer.[164] Graphene has been reported to be one of the strongest materials ever tested with a Young's modulus (stiffness) more than 1 TPa.[165] Another possible cause for this behaviour is that graphene prepared by CVD can be introduced a certain compressive strain because of the wrinkles produced in the growth procedure.[131,134] Such growth-induced strain may make the subsequent compressive stress difficult to be introduced to the graphene. Herein, we deduce that the piezoelectric PMN-PT substrate can produce in-plane strain under a bias voltage, while, only small part of such strain is exerted on the graphene.

Next, we measured the 2D band of Raman frequency during the retention of V_g = 400 V as shown in Figure 4.25. Obviously, there is a continuous blue shift when the voltage is kept for longer duration. The 2D peak shifts towards higher frequency by 6 cm^{-1} as the gate voltage is applied to the hybrid system. After the immediate blue shift, 2D peak shifts steadily to higher frequency with a further shift of about 4 cm^{-1}. Then, after about 60 min, the shift is saturated.

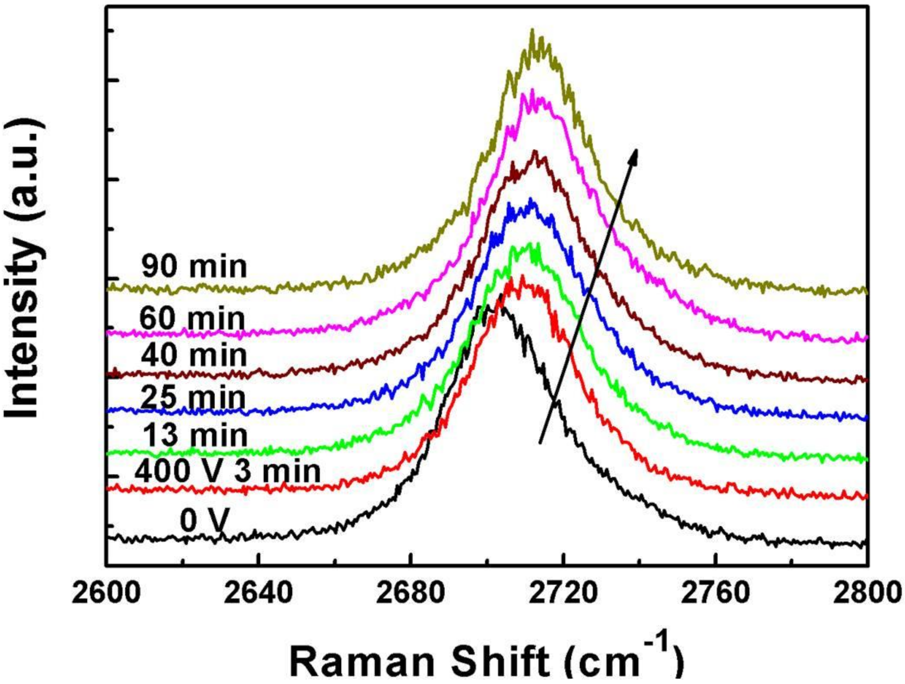

Figure 4.25 Raman spectra of graphene during the retention of the applied voltage of 400 V. For comparison, the Raman spectrum without bias voltage is presented.

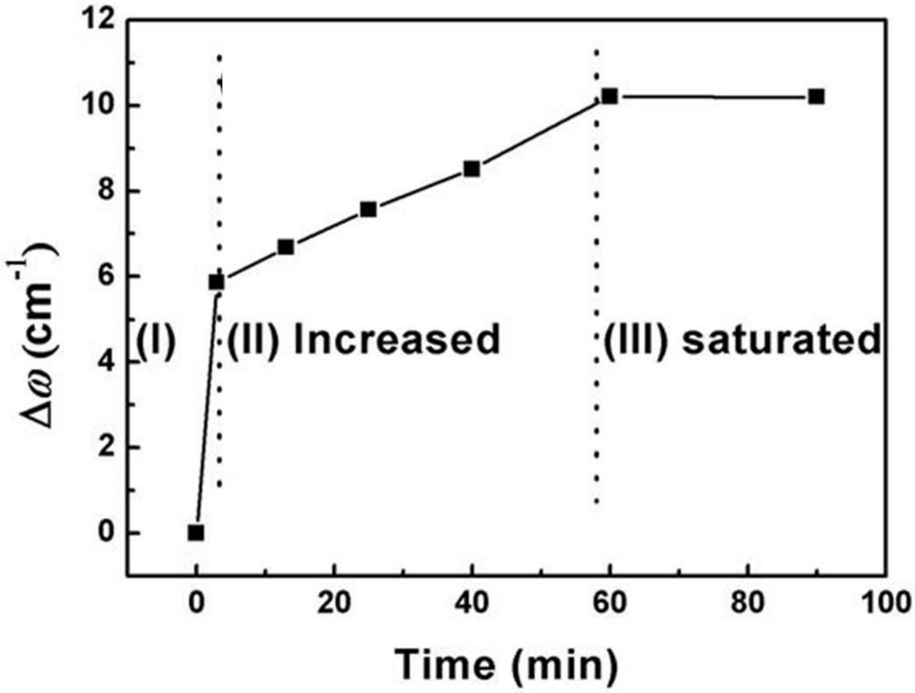

Figure 4.26 The 2D peak shift as a function of time during the retention of the applied external electric field.

As shown in Figure 4.26, the evolution of the 2D peak shift can be divided into three regions as I, II, and III, which correspond to jumping, steadily increased and saturated states, respectively. This experimental result implies that the PMN-PT-induced in-plane strain indeed results in a time-dependent strain to graphene. Based on the 2D Raman peak shift, the strain introduced to the graphene can be calculated. The voltage of 400 V initially corresponds to –0.043% biaxial strain, after further deformation, finally introduces a strain of –0.071% to the graphene. That is the compressive strain applied to the graphene by the PMN-PT is time-dependent.

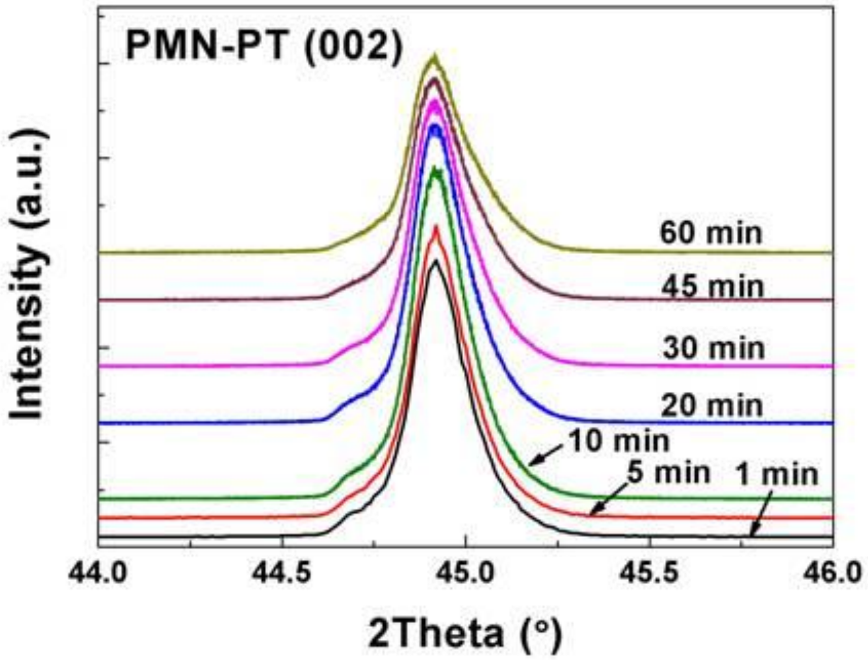

Figure 4.27 Time-dependent XRD 2θ scanning patterns for PMN-PT during the retention of 400 V bias voltage.

The PMN-PT under a bias voltage was measured by the XRD technique, as shown in Figure 4.27. The position of (002) peak is time-independent when the bias voltage keeps constant, which implies that the strain provided by the underlying substrate remains constant.

However, the strain exerted on the graphene is time-dependent. One possible reason for such unique behavior could be the different strain distribution between grains and grain boundaries. It is reported that grain boundaries can reduce the stiffness of graphene. As a consequence, strain in grain boundaries is larger than that inside grains.[35,36] Therefore, the larger strain in grain boundaries would be likely to introduce the additional increase of strain inside the grains. Although such anomalous behavior is elusive to understand, reproducible experimental results still exhibit the time-dependent Raman shift. Also, it is reported that buckling or slipping of the graphene may occur if strain energy is greater than the adhesion between graphene and the substrate.[166] However, in our experiment, the biaxial strain applied to the graphene is provided by the piezoelectric PMN-PT. And such strain is very small (much less than 0.1%) and cannot induce the slipping of graphene. Raman mapping images reveal a uniform and continuous graphene before and after the strain is applied to the graphene, which rules out the possibility of slipping.

4.5 Summary

In summary, we present the transport and vibrational properties of the graphene based on the hybrid structure of graphene/PMN-PT. The graphene/PMN-PT FETs show p-type behaviors and exhibit a large memory window in contrast to conventional graphene/SiO_2 FETs. The on/off ratio, field effect mobility and excess hole concentration are calculated to be about 5.5, 4.52×10^3 $cm^2v^{-1}s^{-1}$ and 6.74×10^{12} cm^{-2}, respectively. A reduction in p-doping for graphene FETs can be obtained through pre-polarization of PMN-PT substrate. The observation of simultaneous rise in gate current with the dramatic transition in drain current suggested that the coupling of the ferroelectric polarization to the charge carriers in graphene can dramatically affect the transport behaviors of graphene. Temperature-dependent R_s of graphene exhibits a metallic behavior and the R_s of graphene on the PMN-PT substrate can be reduced to about 1.25 kΩ/sq. On the other hand, PMN-PT serves as an actuator to provide controllable biaxial strain to the above CVD-grown graphene layer. The PMN-PT substrate could impose impressive strain to graphene and result in a blue shift in the Raman G and 2D bands. The actual biaxial strain exerted on the graphene can be calculated according to the shifts of feature peaks. And such strain is much smaller than that of PMN-PT provided calculated from the XRD. After the initial response to the applied voltage, a continuous blue shift can be detected during the retention of bias voltage. The time-dependent Raman shift could be ascribed to the different strain distribution in CVD-grown graphene.

Chapter 5 **Photovoltaic Properties of Graphene/GaAs Solar Cells**

5.1 **Introduction**

Due to the unique properties of high optical transmittance, mechanical flexible and fascinating electric characteristics (i.e. low resistivity, ultra-high mobility, near-zero band gap etc.),[167,168] graphene has been widely investigated in some optoelectronic devices.[169–171] Also, graphene has been regarded as one of the promising materials for applications in the photovoltaic devices,[172] especially as transparent electrodes.[173] Actually, any semiconductor can form a Schottky junction with a certain metal if the difference between their work functions is large enough, and the carrier density of the semiconductor is moderate.[71] It is very interesting that graphene can serve as such metal in the MS junction, and such junction is capable of exhibiting photovoltaic behaviors, which has been well described in Chapter 2. Due to the difference of the work-function between graphene and the semiconductor, a build-in potential is generated in the semiconductor adjacent to the Schottky junction interface. Under the illumination, the photon-generated carriers can be separated and then transferred to the electrodes, yielding photovoltaic effects from such junction devices. In such Schottky junction solar cells, Si generally plays the part of semiconductor, while, other materials are seldom investigated in the junctions. As we all know, in comparison with Si, GaAs has the merits of high electron mobility and direct band gap, allowing GaAs-based devices to function at high frequencies and be efficient in light emitting devices. Both of the two merits are very important in optoelectronic devices. As a consequence, GaAs is a traditional semiconductor in photovoltaic devices and shows superb performance. So, it is interesting to investigate the graphene/GaAs heterojunction. In this chapter, chemical-vapor-deposited graphene sheets have been transferred onto n-type and p-type GaAs (n- and p-GaAs) substrates. The contact behaviors, rectifying characteristics and photovoltaic effects of graphene/GaAs heterojunctions have been systematically investigated.[94]

5.2 Experimental

5.2.1 Fabrication of graphene/GaAs junction solar cells

Single-layer graphene (SLG) and bilayer graphene (BLG) flakes were prepared on Cu foils through CVD method. The graphene/GaAs hetero-junctions were fabricated by transferring the graphene sheets onto n- or p-GaAs substrates by standard transfer process. Figure 5.1 shows the schematic of the graphene/GaAs junction soalr cell. Before transferring graphene, low-resistance Au contacts were grown on the back side of the GaAs by thermal evaporation. Then, a 200-nm SiO_2 layer was deposited on GaAs substrate by magnetron sputtering at 400 K using a defined mask to form a GaAs channel with a width of 1 mm which will be used to contact with graphene.

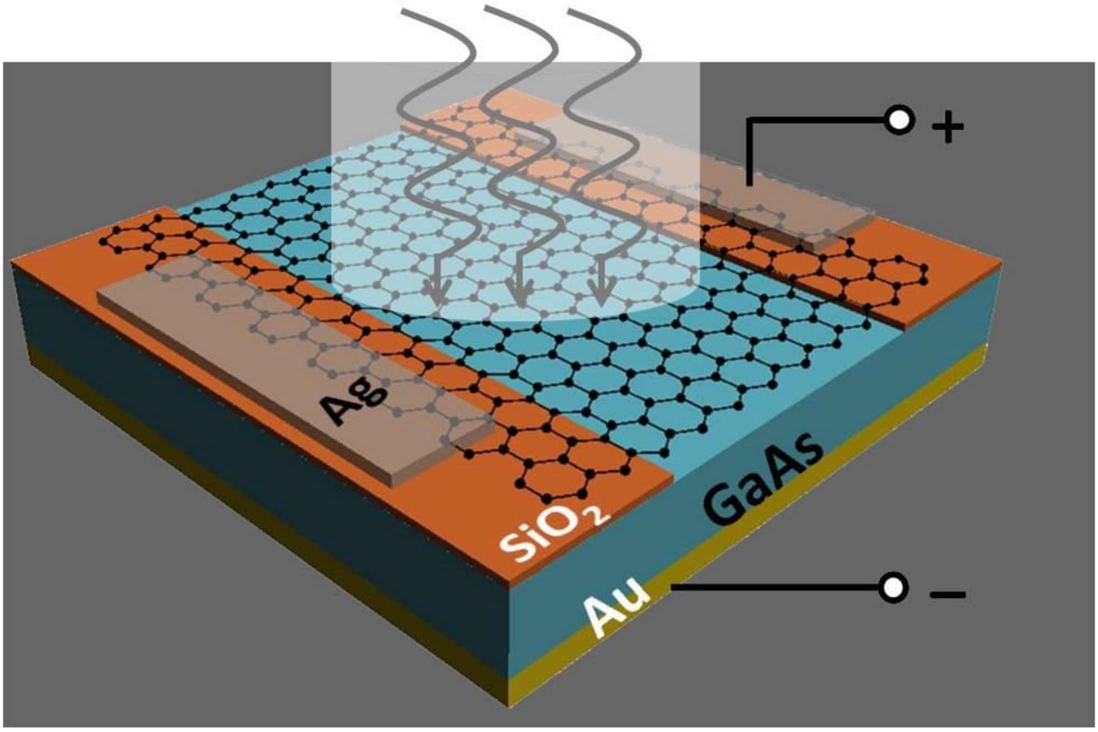

Figure 5.1 The schematic of Ag/graphene/GaAs/Au hybrid system with SiO_2 as an insulating layer.

After the growth of SiO_2 layer, SLG and BLG flakes were respectively transferred onto n-GaAs (p-GaAs) substrates with the resistivity of 1.2 ~ 1.6 $\times 10^3$ Ωcm (3.2 ~ 3.4 $\times 10^2$ Ωcm). In our experiments, the 200-nm SiO_2 serves as an insulator layer which will prevent the direct contact of metal (the top Ag electrode) with semiconductor (the GaAs substrate) due to the existing holes and/or discontinuity in CVD-grown graphene. There are inevitably a few holes existing in one-atom thick SLG formed during the growth or transferring process. Through this process, we can rule out the possibility of Ag/GaAs contact and conclude the M/S contact is graphene/GaAs. Thus, an insulating layer of SiO_2 is essential in this Schottky junction solar cell.

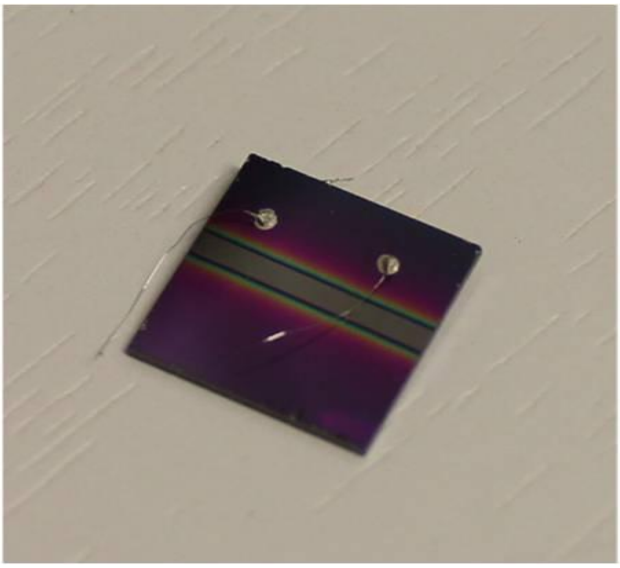

Figure 5.2 The real image of the graphene/GaAs Schottky junction solar cells on one GaAs chip.

Figure 5.2 shows the real image of two pieces of graphene sheets after transferred onto the GaAs substrate (10 mm × 10 mm × 0.5 mm) to form two individual solar cell devices. The graphene layers could be combined with the underlying GaAs channel to form a junction with the contact area of about 1 mm × 1 mm. Owing to its good mechanical properties, the graphene sheet could be continuous (at least electrically continuous) across the patterned steps between the SiO_2 layers and GaAs channel. Baking was then performed at 110 ℃ for 20 min to achieve tight adhesion between the graphene and the GaAs. Then, silver paste was employed to serve as top electrodes on graphene where the underlying layer is SiO_2 insulator rather than GaAs. The Aluminum wire is used to connect the Ag top electrodes to the measurement systems.

5.2.2 Characterization

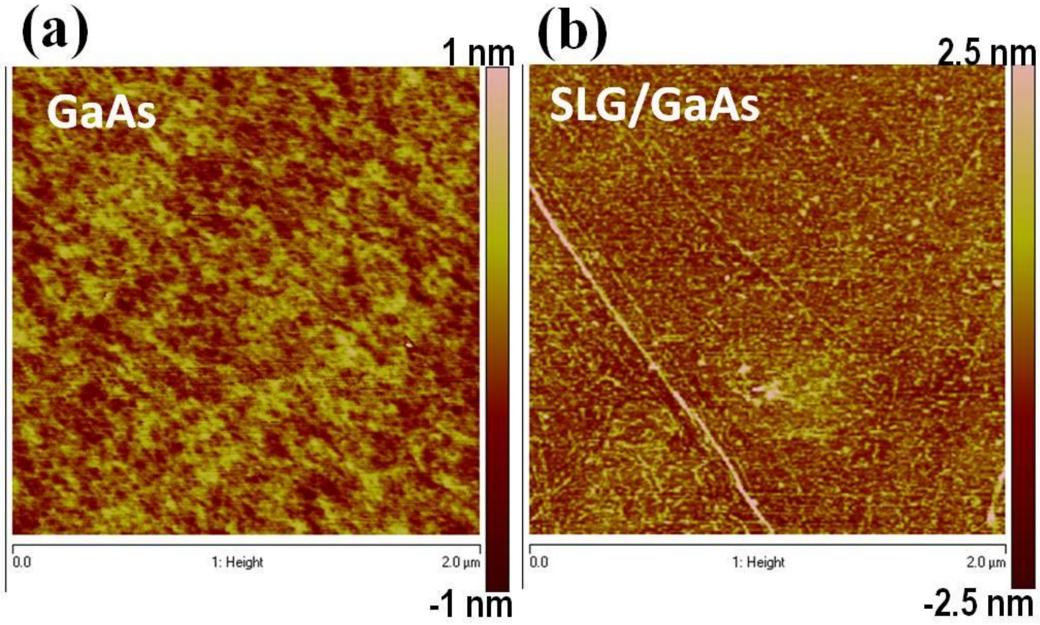

Figure 5.3 Atomic Force Microscopy images of (a) GaAs substrate; (b)SLG on GaAs the substrate.

The surface morphology of the GaAs substrate and the graphene was characterized by AFM (DI Nanocope 8). The AFM image of the GaAs substrate (Figure 5.3a) demonstrates its very smooth surface (with the RMS roughness of 0.195 nm), providing good mechanical support to the above graphene layers. Figure 5.3b shows the surface morphology of the SLG sheet transferred onto the GaAs substrate with the RMS roughness of 0.482 nm. There are wrinkles in the SLG sheet on GaAs substrates, which are also inevitable in CVD-grown graphene sheets after being transferred onto SiO_2 substrates.

The BLG sheet without cracks is shown in Figure 5.4a, suggesting a continuous and uniform graphene sheet has been transferred onto the GaAs substrate. Similarly to SLG, the wrinkles are also inevitable in BLG on GaAs, as shown in Figure 5.4b. Although there are wrinkles in the graphene layer, the flat SLG and BLG sheets can be obtained on the GaAs substrates. This is also essential to the fabrication of graphene/GaAs junction solar cell.

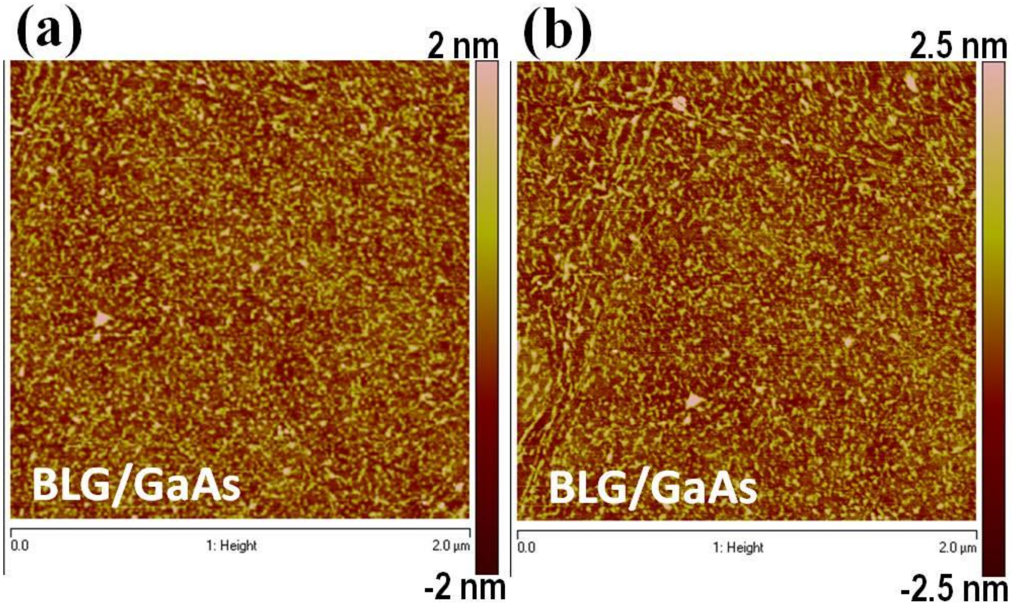

Figure 5.4 AFM images of BLG on GaAs substrates. (a) A uniform graphene sheet without winkles; (b) winkles on graphene.

The graphene flakes on Cu and GaAs substrates were characterized by Raman spectroscopy (HORIBA, HR800) with the excitation wavelength of 488 nm and the laser spot size of about 1 μm. Figure 5.5 shows the typical Raman spectra of the SLG and BLG on Cu foils. After the graphene sheets were transferred onto the GaAs substrates, their Raman spectra were measured which are shown in Figure 5.6. The most intense features, the G and 2D peaks, can be clearly observed in all Raman spectra. For the graphene on GaAs, sharp 2D peak lies at about 2682 cm^{-1} (2689 cm^{-1}) with full-width-at-half maximum (FWHM) of about 46 cm^{-1} (54 cm^{-1}) for single-layer (bilayer) graphene. Considering the 2D peak is relatively intense (approximately 2 times the height of G peak) and the feature peaks are slightly red-shifted (in comparison with the other Raman spectrum), we can conclude that single- and bilayer graphene sheets are successfully transferred onto GaAs substrates, respectively. No defect-related D peak is detected, confirming the absence of significant defects in the graphene sheets.

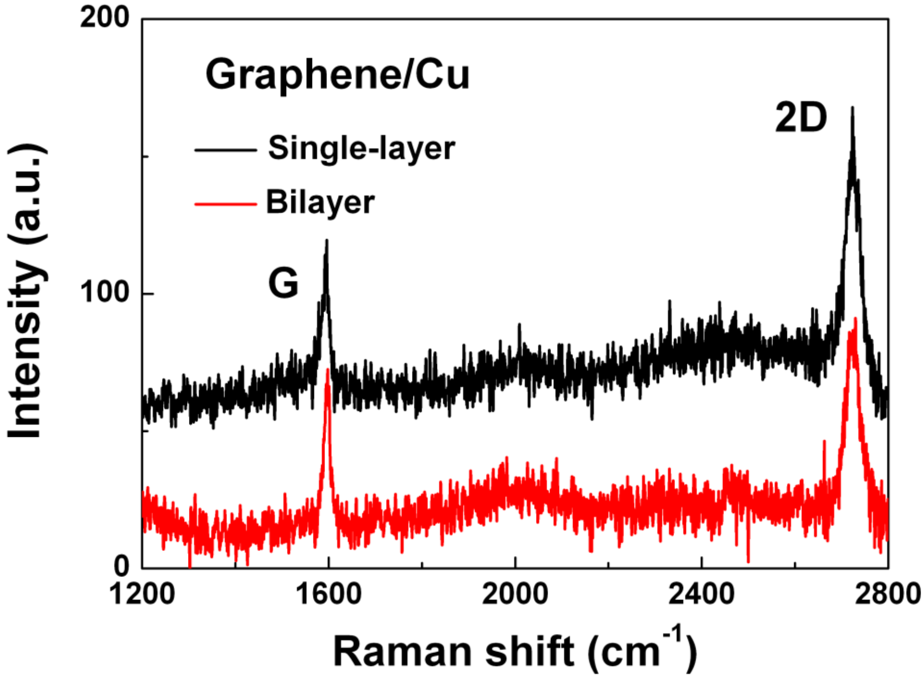

Figure 5.5 The Raman spectra of SLG and BLG on Cu foils.

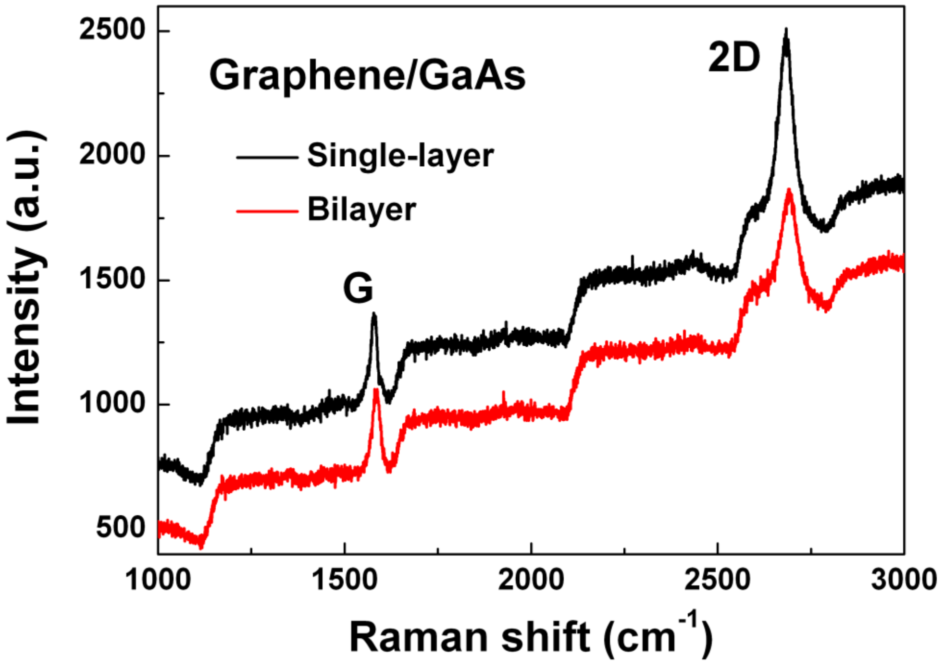

Figure 5.6 Raman spectra of SLG and BLG measured after transferred onto GaAs substrates.

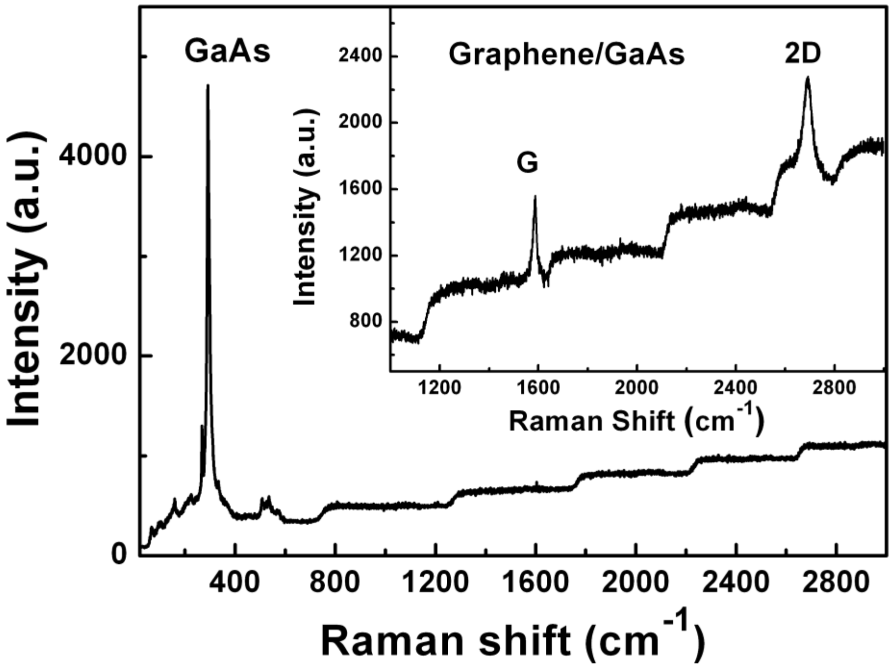

Figure 5.7 Raman spectrum of GaAs substrate. The inset shows the Raman spectra of bilayer graphene after transferred onto the GaAs substrate.

It should be noted that the steps in the Raman spectra of the graphene/GaAs, as shown in Figure 5.7, result from the underlying GaAs substrate. They also appear in the Raman spectrum of GaAs substrate without graphene layer. So, such steps are detected in the Raman spectrum of graphene after transferred onto the GaAs substrate. The corresponding Raman spectrum of bilayer graphene on the GaAs substrate is also shown in the inset of Figure 5.7 for comparison.

The current–voltage (*I*–*V*) data of the devices were recorded using a Keithley 2400 sourcemeter. The forward bias was defined as the case where positive voltage was applied to the graphene. The photovoltaic effects of the devices were tested with a solar simulator (Thermo Oriel 91192-1000) under conditions of AM 1.5 illumination. All the above measurements were performed in air ambient at room temperature.

5.3 The electrical properties of graphene/p-GaAs heterojunction

The contact behaviors between SLG and Ag electrode were firstly studied. The measurement system is schematically shown in Figure 5.8. This strategy not only enables us to measure the contact behaviors between graphene and the Ag electrode, but also provides us the opportunity to characterize the continuity of graphene after transferred onto GaAs substrate with a SiO_2-step.

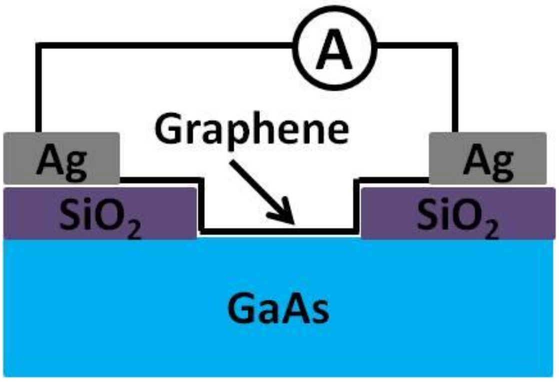

Figure 5.8 Schematic of current measurement of Ag/graphene/Ag hybrid system for graphene on the GaAs substrate.

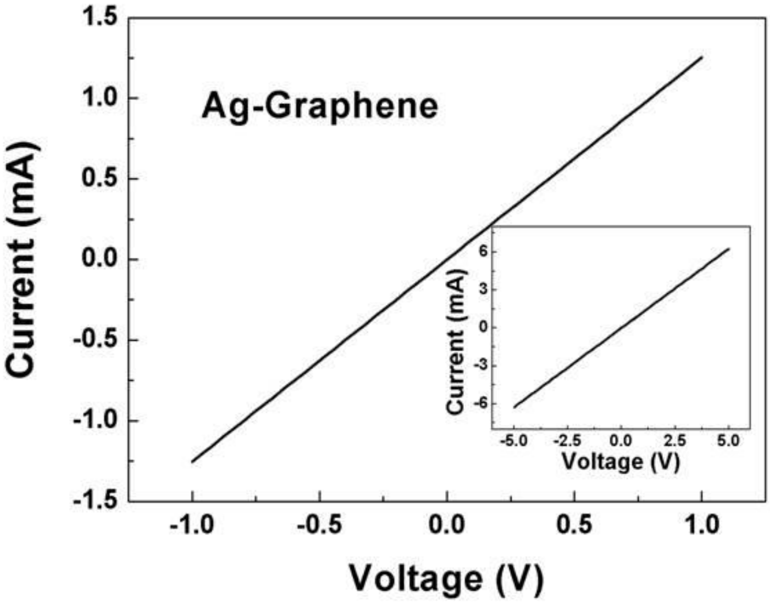

Figure 5.9 The current between two Ag electrodes as a function of the applied voltage from –1 to 1 V. Inset shows the linear curve with the applied voltage ranging from –5 to 5 V.

A good Ohmic contact is formed between the top electrodes and the graphene, as shown in Figure 5.9. The current shows linear relationship on the applied bias voltage. Even when the applied bias voltage reached 5 V, the linear and symmetric *I*–*V* curve can still be obtained, as shown in the inset of Figure 5.9. The symmetric *I*–*V* curve not only indicates a good Ohmic contact between graphene and Ag, but also suggests a continuous graphene sheets through the SiO_2 step with height of about 200 nm.

The dark and light current density–voltage (*J*–*V*) curves of the BLG/p-GaAs hybrid system are shown in Figure 5.10. A nearly linear *J*–*V* curve indicates that an Ohmic contact is obtained between graphene and p-GaAs. The illumination still gives rise to the linear *J*–*V* characteristics. And the current density keeps almost unchanged after illumination. The doping concentration of p-GaAs is in the range of 4.81~4.87 × 10^{17} cm^{-3}. The Fermi level (E_F) of n-GaAs can be calculated according to the equation:

$$E_F = E_i - \Delta E_F \tag{5.1}$$

where E_i is the intrinsic Fermi level, showing where the Fermi level would be for the material to be neutrally doped, E_i = 4.785 eV, and ΔE_F is the energy difference between E_i and E_F. ΔE_F can be expressed as the following equation:

$$\Delta E_F = kTln\, N_d/n_i \tag{5.2}$$

where k is the Boltzmann constant, T is the absolute temperature, N_d is the real doping concentration, and n_i is the doping concentration when the Fermi level located at E_i. For GaAs, n_i = 1.8 $\times 10^6$ cm^{-3}. Then, we can obtain the Fermi level, i.e., the work function, of p-type GaAs ($\Phi_{\text{p-GaAs}}$) is about 5.45 eV.

In principle, there should be a Schottky barrier between graphene and such p-type semiconductor considering the higher work function of p-GaAs than that of the graphene Φ_G (4.8~5.0 eV). However, the dark *J*–*V* curve exhibits Ohmic characteristics. This can be attributed to the p-type character of semimetal graphene in air ambient at room temperature.[144] Thus, a resistance in series (including contact resistance between graphene and p-GaAs, and the contact resistance between p-GaAs and gold electrode, as well as the resistance of p-GaAs itself) is actually measured. For this resistance in series, the *J*–*V* curve should keeps almost unchanged under illumination.

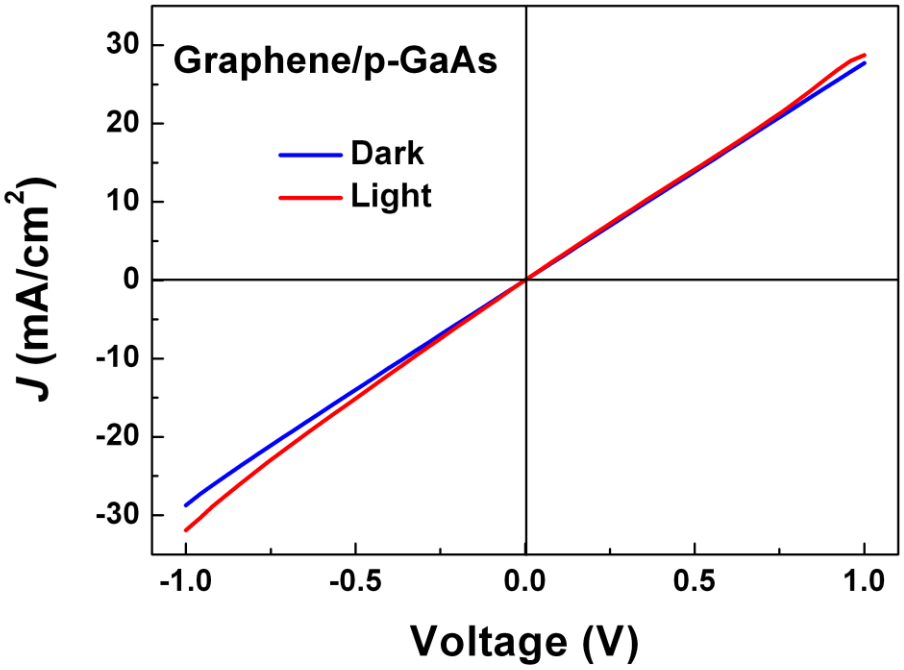

Figure 5.10 Dark and light current density–voltage curves of the heterojunction of bilayer graphene and p-GaAs.

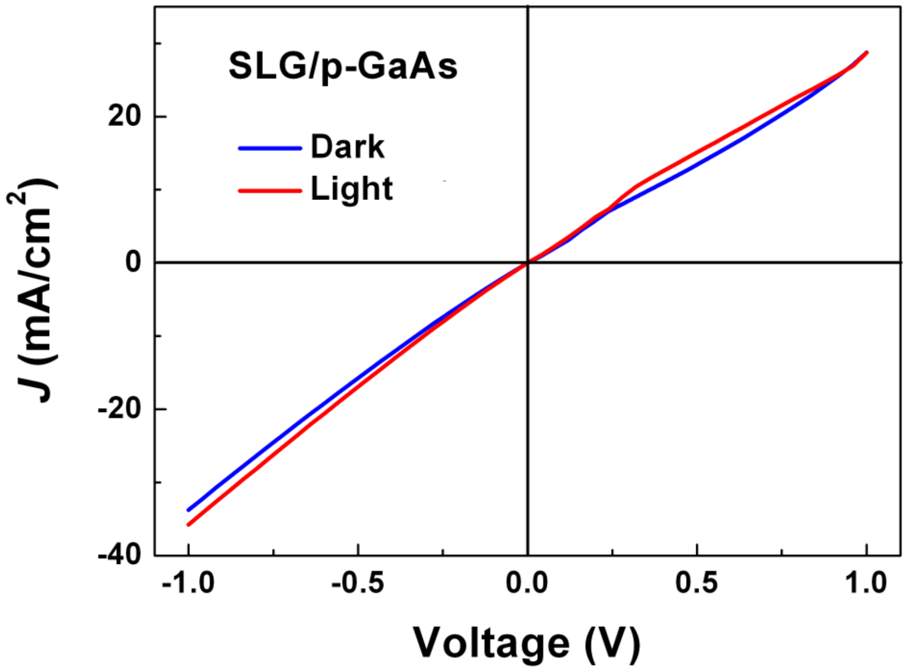

Figure 5.11 Dark and light current density–voltage curves of the heterojunction of SLG and p-GaAs.

For the SLG/p-GaAs heterojunctions, almost same linear *J*–*V* behaviors can be obtained, as shown in Figure 5.11, which can further indicate that the CVD-grown graphene can form Ohmic contact with the p-type GaAs.

5.4 The photovoltaic properties of graphene/n-GaAs heterojunction

In the following, the contact behaviors of graphene/n-GaAs will is addressed. The *J*–*V* curves of SLG/n-GaAs junctions in dark and light are shown in Figure 5.12. For n-GaAs, the doping concentration is about 5×10^{17} cm^{-3}, the work function of n-type GaAs ($\Phi_{n\text{-GaAs}}$) can be calculated (~4.11 eV) according to Equations 5.1 and

5.2. A Schottky junction should be formed due to the large work function difference between graphene and n-GaAs. The dark *J–V* curve of SLG/n-GaAs junction solar cell shows rectifying characteristics with a rectification ratio of about 24 at ± 1 V, suggesting a Schottky junction is formed between the SLG and n-GaAs. When measured under conditions of AM 1.5 illumination, the short-circuit current density (J_{sc}) and open-circuit voltage (V_{oc}) for SLG-based solar cell is 6.43 mA/cm^2 and 0.62 V, respectively. This gives rise to a PCE of 1.09 % with the fill factor (*FF*) of about 0.27, as shown in Figure 5.12. Herein, it is believed that graphene can combine with n-GaAs to form a Schottly junction and yield photovoltaic effects under illumination.

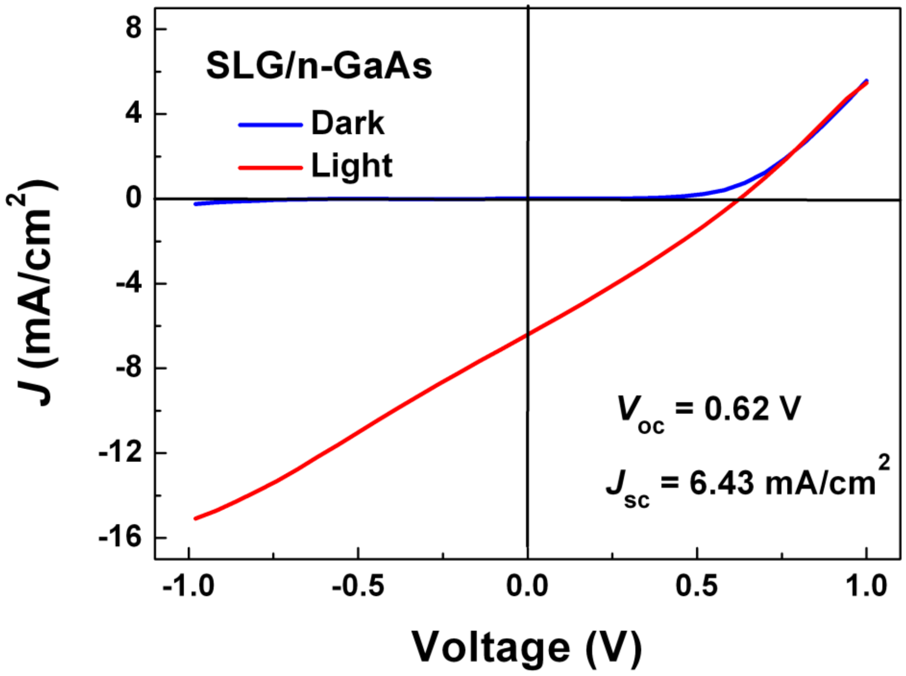

Figure 5.12 Dark and light current density–voltage curves of the heterojunction of SLG/n-GaAs.

For BLG on n-GaAs, the dark *J–V* curve exhibits enhanced rectifying characteristics with a rectification ratio of about 43 at ±1 V, as shown in Figure 5.13 Accordingly, the BLG-based Schottky junction shows superior photovoltaic effects to SLG. Not only the J_{sc} and V_{oc} are improved to 10.03 mA/cm^2 and 0.65 V, respectively, but also a higher PCE of 1.95 % and fill factor of 0.30 can be obtained. Such BLG/n-GaAs solar cell shows a PCE value comparable to that of other pristine graphene/semiconductor (such as Si, CdS and CdSe.) junction-based ones. Besides, the PCE value is maintained over a period of more than six months, exhibiting excellent stability. Also, it should be noted that the graphene/n-GaAs herterojunction solar cells exhibit a relatively large V_{oc} compared to their other semiconductor counterparts (with a V_{oc} usually not in excess of 0.6 V).

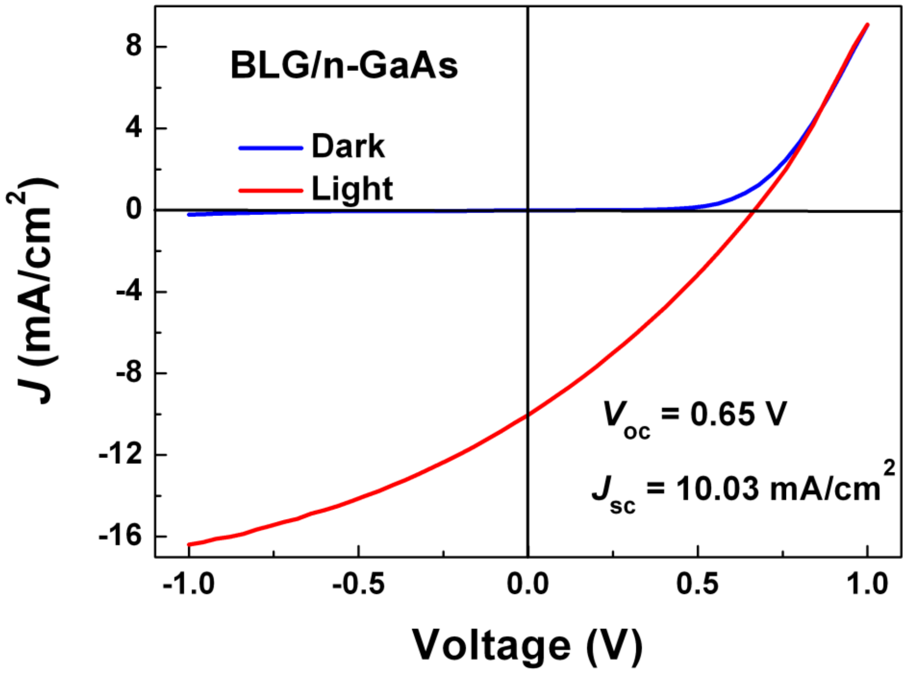

Figure 5.13 Dark and light current density–voltage curves of the heterojunction of BLG/n-GaAs.

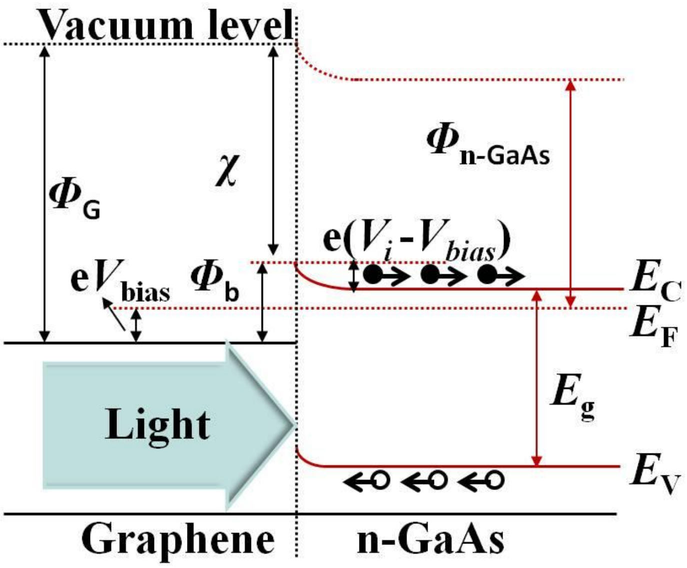

Figure 5.14 The energy band diagram of graphene/n-GaAs Schottky junction solar cell at the interface under illumination. E_C, E_V, E_F correspond to the conduction band edge, valence band edge, and Fermi level of n-GaAs, respectively. E_g stands for the energy gap.

Table 5.1 The photovoltaic behaviors of SLG and BLG Schottky junction solar cells.

Cell device	J_{sc} (mA/cm^2)	V_{oc} (V)	PCE (%)	*FF*
SLG	6.43	0.62	1.09	0.27
BLG S1	10.03	0.65	1.95	0.30
BLG S2	8.43	0.65	1.66	0.30

Table 5.1 exhibits the specific photovoltaic parameters of one SLG and two BLG (S1 and S2) based Schottky junction solar cells. It is clear that BLG-based solar cells show better performance compared to SLG/n-GaAs junction solar cell. In theory,

the graphene layer not only serves as a transparent electrode for the junction solar cell, but also contributes to carrier separation and transport. To understand the underlying mechanism of the contacts of graphene/GaAs qualitatively, the energy band diagram of the junction is plotted (Figure 5.14). Theoretically, any semiconductor with electron affinity (χ = 4.07 eV) lower than the work function of the metal can create an M/S diode with Schottky-barrier height ($\Phi_b = \Phi_G - \chi$), giving rise to the rectification behaviors of the junction. Considering the graphene/n-GaAs junction, a build-in potential ($eV_i = \Phi_G - \Phi_{\text{n-GaAs}}$) is generated in n-GaAs adjacent to the Schottky junction interface due to the difference in the work functions of graphene and n-GaAs. A space-charge region is formed accompanied by the build-in voltage (V_i) in the semiconductor near the interface. Under illumination, the carriers (electron and hole) generated by photons can be separated by the build-in electric field, yielding photovoltaic effects from such junction devices. Reproducible measurement results can be obtained when we characterize the similar junction devices of graphene/n-GaAs, which indicates a Schottky junction solar cell can be fabricated by transferring graphene onto an n-GaAs substrate.

It is well known that Schottky diodes are expected to pass current in the forward bias (when the graphene layer is positively biased) while becoming highly resistive in the reverse bias (when the semiconductor is positively biased). Such rectifying behavior of M/S junction attributed to the Schottky barrier at the interface is well described by thermionic-emission theory and can be expressed as:

$$J(V) = J_s\left[\exp\left(\frac{eV}{nk_{\mathrm{B}}T}\right) - 1\right] \tag{5.3}$$

where J_s is the reverse saturation current density, e is the electronic charge, n is the diode ideality factor, k_B is the Boltzmann constant, T is the absolute temperature. For an ideal diode, $n = 1$. While, for a non-ideal diode, $n > 1$.

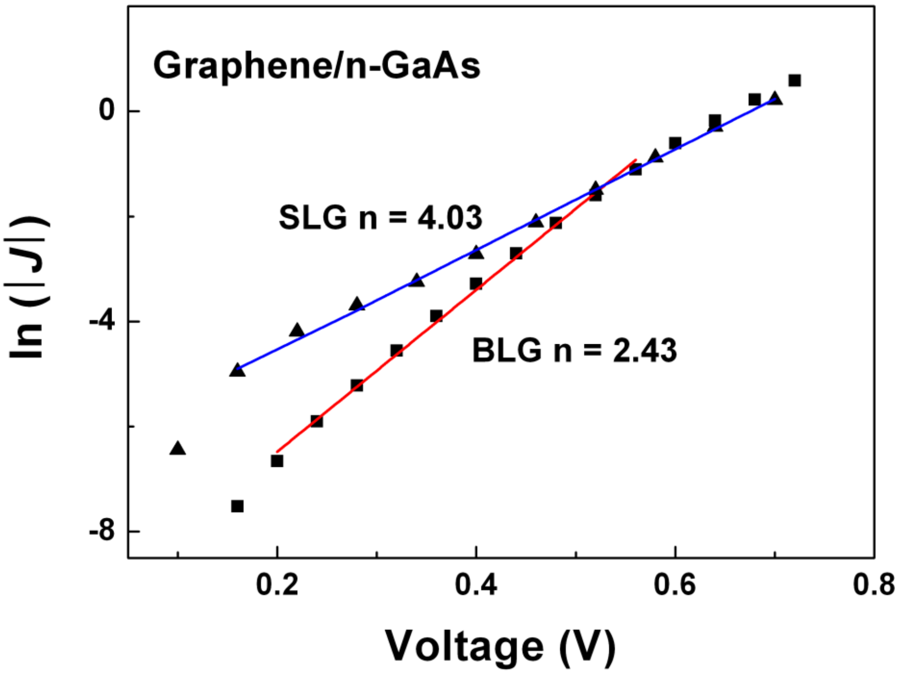

Figure 5.15 Linear fit to the ln(|J|)–V curve of SLG/n-GaAs and BLG/n-GaAs Schottky junction.

A nearly linear fit to the ln(|J|)–V curves of both SLG- and BLG-based Schottky junctions can be obtained in the range of 0.2 to 0.7 V (as shown in Figure 5.15). According to the slope of the fitting line, we can deduce the diode ideality factor of 4.03 and 2.43 for SLG- and BLG-based Schottky junction, respectively. Additionally, J_s can be described as:

$$J_s = A^{*}T^{2}\exp\left(-\frac{e\Phi_{\mathrm{b}}}{k_{\mathrm{B}}T}\right) \quad (5.4)$$

where A^* is the effective Richardson's constant of GaAs.[174] Then, the Schottky-barrier height can be calculated to be about 0.68 and 0.75 eV for SLG- and BLG-based Schottky junction, respectively. These values agree well with the difference between Φ_{G} and χ.

Furthermore, series resistance R_{s} of the diode can be extracted by plotting the line of dV/dln$I$ vs. I as shown in Figure 5.16. The slope of the linear fitting to the curves gives rise to R_{s} of 40.5 Ω (20.1 Ω) for SLG (BLG) diode with the contact area of about 0.01 cm^2 according to Equation 5.5.

$$I = I_s\exp\left(\frac{e(V-IR_{\mathrm{s}})}{nk_{\mathrm{B}}T}\right) \quad (5.5)$$

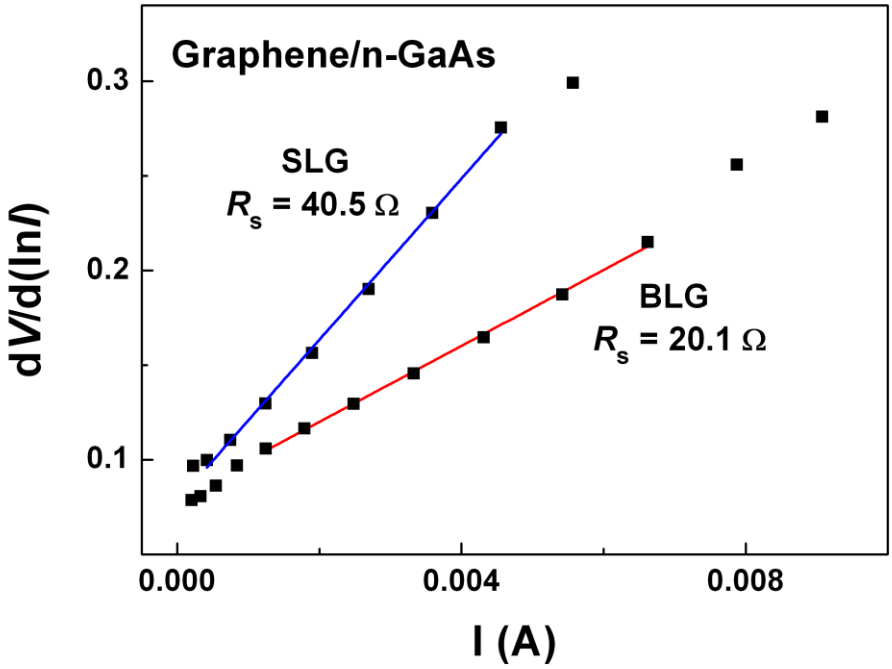

Figure 5.16 Linear fit to the line of dV/dln$I$ vs. I for SLG/n-GaAs and BLG/n-GaAs Schottky junction.

In view of the unexpectedly large ideality factor, low Schottky-barrier height, and high series resistance, SLG-based Schottky junction shows relatively poor photovoltaic characteristics compared to its BLG counterparts. Also, it is reported that multilayer graphene in solar cells exhibits better conversation ability and device stability compared to SLG.[175] In our experiment, the high series resistance between SLG and n-GaAs is considered to be a major factor for suppressing the carrier separation and transport. Accordingly, the carriers generated at the interface of the junction can easily recombine, which can give rise to the degradation of SLG-based solar cell. Moreover, the lower Schottky barrier height can also induce the degraded performance of SLG/n-GaAs solar cell. Besides, SLG is believed to contribute little in establishment of the depletion layer considering the one-atom thickness.[87] Thus, the photo-generated charges can be easily recombined, inducing the degraded performance of SLG/n-GaAs in our experiments.

5.5 Summary

In summary, the p-type GaAs can form ohmic contact with both the CVD-grown SLG and BLG sheets, while n-type GaAs can be combined with such graphene layers to form Schottky junctions. We have firstly demonstrated photovoltaic characteristics of graphene-on-GaAs Schottky junction with V_{oc} of 0.65 V, J_{sc} of 10.03 mA/cm^2 and PCE value of 1.95 %. Such performance parameters of the device are comparable to or even higher than those of other pristine graphene/semiconductor junction-based devices. Our calculations based on the rectifying characteristics of the diodes suggest that bilayer graphene/GaAs junction exhibits smaller ideality factor (2.43), higher Schottky barrier height (0.75 eV), and lower series resistance (20.1 Ω) compared to single-layer one, which can give rise to the improved photovoltaic behaviors of BLG-based junction solar cells. This work implies that the developed graphene/GaAs system can be processed to be a new system for future photovoltaic applications considering the high-performance of optoelectronic capabilities of radiation-resistant GaAs wafer.

Chapter 6 **Nonlinear Optical Properties of Few-Layer GaSe sheets**

6.1 **Introduction**

2D layered materials have drawn extensive attention since the first discovery of graphene through the method of mechanical exfoliation by Geim's group in 2004.[1] Graphene, with its unique 2D-layered structure, exhibits outstanding electronic, thermal, optical, and mechanical properties. And now graphene is considered to be one of the most promising materials for future applications in nanoelectronics. Indeed, the use of simple micro-mechanical cleavage technique has been expanded from graphene to other layered materials. Beyond graphene, a large variety of 2D materials can be exfoliated from some layered materials with the stacked structure in their bulk materials like graphite. Among the recent advances, 2D gallium selenide (GaSe), a layered III-VI semiconductor, has been receiving lifted attention from electronic and optoelectronic applications.[21,23,25] GaSe is a layered III-VI semiconductor, which consists of covalently bonded stacks of four atomic layers that are held together by a weak interstack interaction of the van der Waals type. Monolayer GaSe flakes have been obtained by mechanical cleavage method,[21] vapor phase mass transport method, van der Waals epitaxy method and pulse laser deposition method.[176]

It should be noted that one of the most important properties of bulk GaSe is the nonlinear optical property due to the absence of the inversion symmetric center.[48,49] It is known that nonlinear optics has been widely used in many important applications such as integrated optics, optical information communications, biology and material science as well as imaging techniques.[50,51,177–179] In comparison with the bulk counterparts of GaSe, the nonlinear optical properties have not been explored in its 2D form. Therefore, it is very interesting to investigate whether the intrinsic nonlinear features can be maintained in 2D layers. In this chapter, atomic-layered and micro-scale GaSe thin flakes were obtained by the mechanical exfoliation of bulk GaSe crystal and then transferred onto 300-nm SiO_2 coated Si and transparent glass substrates. This provides us an opportunity to study systematically the nonlinear optical properties of 2D layered GaSe samples. In the sense of application, this issue should be critical in developing nanophotonic devices based on 2D atomic layers.[180]

6.2 Experimental

6.2.1 Fabrication of 2D GaSe sheets

In our experiments, 2H-GaSe crystals were purchased from 2D Semiconductors. In bulk, β- and ε-GaSe can be obtained. Few-layer GaSe sheets can be cleaved and adhered to the subsequent 300-nm SiO_2 coated Si and transparent glass substrates by the micro mechanical exfoliation method. Both β-GaSe and ε-GaSe are hexagonal symmetric with a 2H stacking, and they will be used in later section of our experiments. The schematics of β-GaSe demonstrated in side and top view are shown in Figure 6.1a and b, respectively. β-GaSe has two basic layers per unit cell and belongs to space group of D^4_{6h} with an inversion symmetric center due to the stacking sequence.

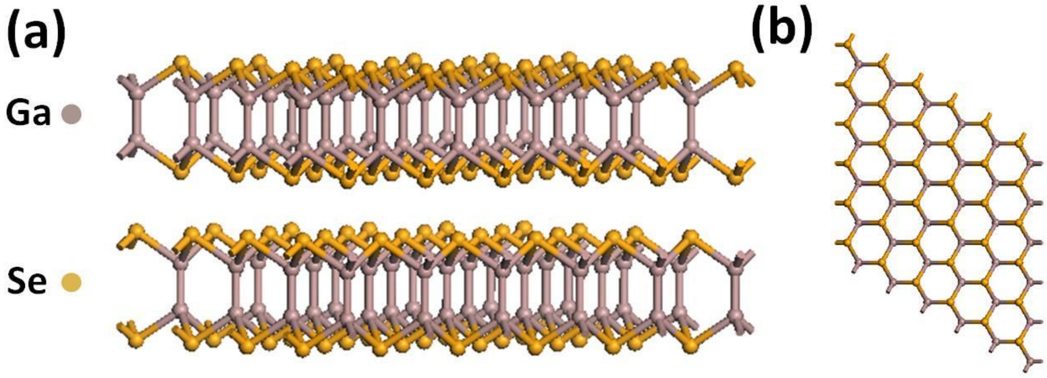

Figure 6.1 GaSe crystal structure: (a) side view and (b) top view for β-GaSe.

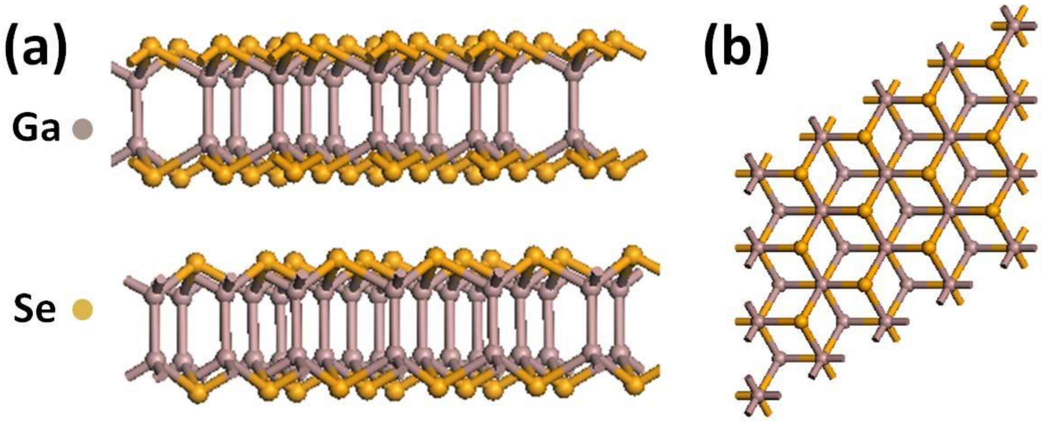

Figure 6.2 GaSe crystal structure: (a) side view and (b) top view for ε-GaSe.

On the other hand, the layered structure of ε-GaSe is generated from one primitive layer by translations, as schematically shown in Figure 6.2a and b. Among different modifications, ε-GaSe ranks the most efficient nonlinear material with high nonlinear coefficient (d_{22}) of 54 pm/V.

6.2.2 Characterization

Atomic force microscopy (AFM, DI Nanocope 8) combined with optical microscope (OM, Olympus DX51) was employed to perform the surface morphology characterization and determine the thickness of GaSe layers. Figure 6.3a shows the optical image with different optical contrast of multilayers of GaSe flakes deposited on a 300-nm SiO_2 coated Si substrate by mechanical exfoliated method. The GaSe thin flakes change their color gradually to green by decreasing their thickness, which is consistent with previous results for 2D GaSe on 300 nm SiO_2 reported by other group.[21] The AFM image for the thin GaSe flake, corresponding to the black square in Figure 6.3a, exhibits a flat and lateral micro-scale GaSe thin layer, as shown in Figure 6.3b. The inset shows corresponding AFM height profile of the GaSe layer. Apparently, the thickness is about 3 nm corresponding to 3-layer (3L) GaSe thin flake. The AFM measurements combined with the different optical contrast can determine the 5L and 7L of thickness in the vicinity of 3L GaSe flake, as shown in Figure 6.3a.

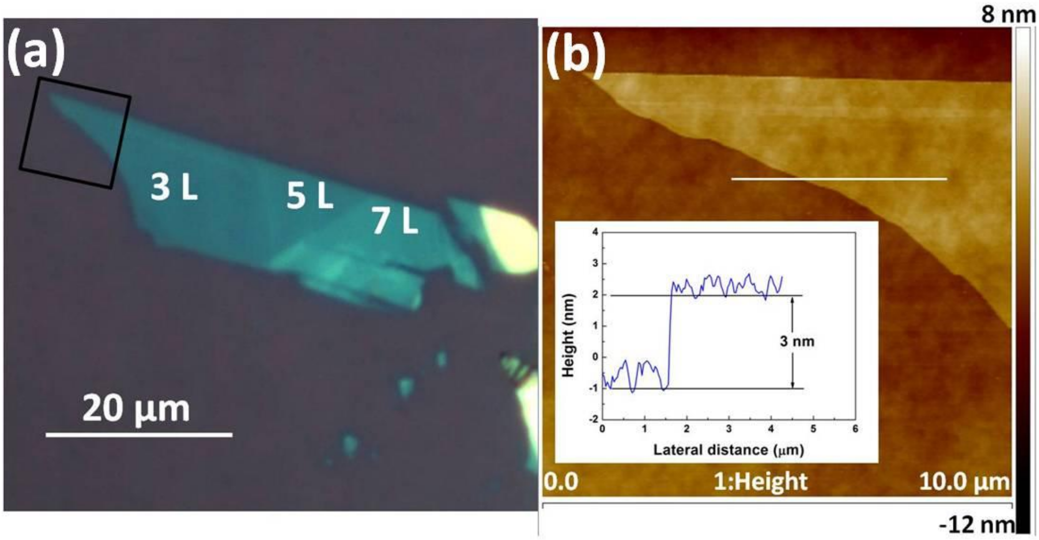

Figure 6.3 (a) Optical image of a GaSe sample on a SiO_2/Si substrate. The layer number is marked in the corresponding area. (b) AFM image of the GaSe flake with the thickness of about 3 nm. Inset shows its corresponding AFM height profile.

Moreover, the GaSe nanosheets were characterized using micro Raman spectroscopic system (HORIBA, HR800) equipped with the 633-nm laser. A 100 × objective lens was used in the system with a NA of 0.9 and the spot size of about 1 µm. Micro Raman is a powerful technique to characterize 2D layered materials and is also an efficient way to determine the layer number. Figure 6.4 shows the Raman spectra of GaSe flakes with different layer number obtained from the AFM height profile. The Raman spectrum of SiO_2/Si substrate is also shown in Figure 6.4 for comparison. In theory, there are two A_{1g} modes in GaSe, i.e. A_{1g}^1 (133 cm^{-1}) and A_{1g}^2 (306.8 cm^{-1}) corresponding to the vibration in the out-of-plane direction, while E_{1g}^2 (250 cm^{-1}) and E_{2g}^1 (211.9 cm^{-1}) are associated with the in-plane vibrational modes. As can be seen from Figure 6.4, all the Raman peaks are significantly thickness-dependent. A_{1g}^1 mode shows a dramatic reduction of intensity with decreasing the layer number. The A_{1g}^2 mode, which has overlaps with the Raman peak of the substrate at about 307 cm^{-1}, exhibits a slight red-shift to about 303 cm^{-1} when reducing the layer number to 3L. The Raman scattering intensity of out-of-plane modes is stronger than that of the in-plane modes, which also become less effective as the layer number decreases.

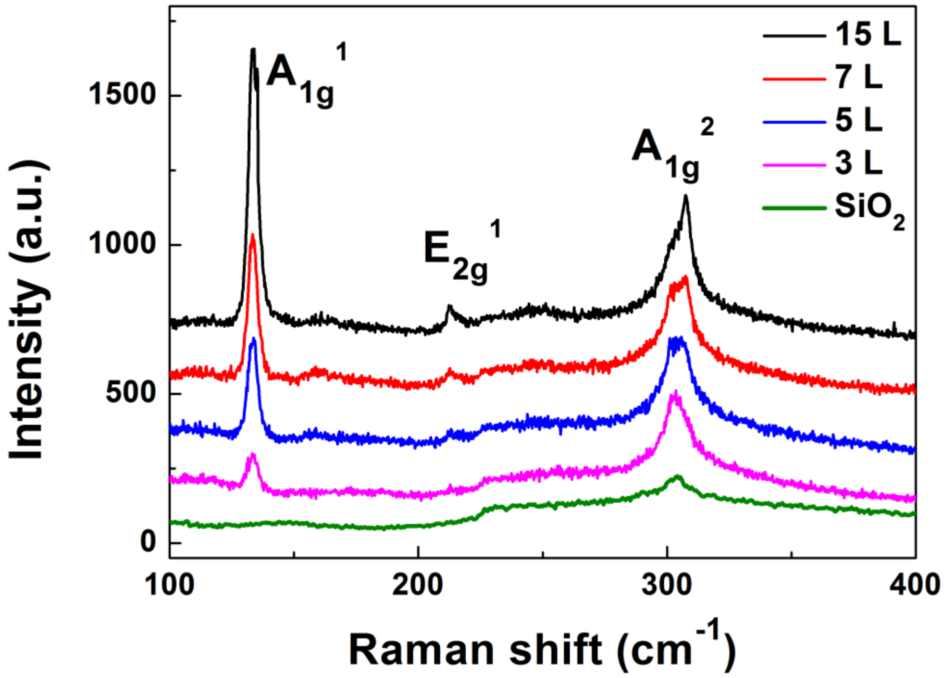

Figure 6.4 Raman spectra of GaSe thin flakes with different thickness on SiO_2/Si with the excited laser of 633 nm. The substrate without GaSe sheets was also measured for comparison.

The photoluminescence measurements were performed by employing 488-nm laser and using the PL mode in this micro Raman system. Ti:sapphire fs laser (repetition rate: 80 MHz, pulse duration: 100 fs) with the wavelength of 800 nm was used to explore the nonlinear optical properties of GaSe sheets on SiO_2/Si substrates.

The spot size of fs laser is about 1 μm. Additionally, the nonlinear optical properties of GaSe flakes on transparent glass substrates were measured by using a confocal laser scanning microscope (Leica TCS SP5) equipped with a fs Ti:sapphire laser (Libra II, Coherent). For the measurements in the confocal scanning system, the GaSe flakes were transferred onto the transparent glass substrate so that the SHG signal could be detected through transmission.

6.3 Second harmonic generation of GaSe nanosheets

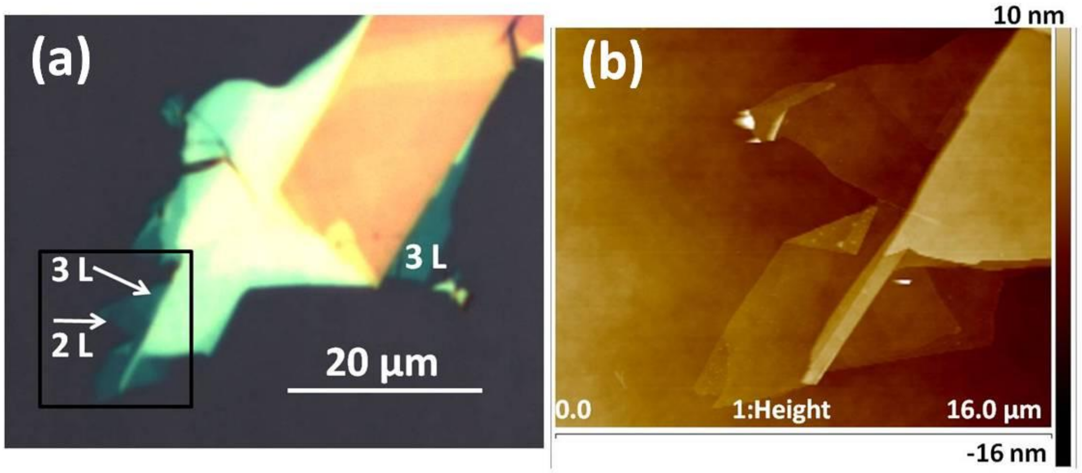

Figure 6.5 (a) Optical image of layered GaSe flakes on a SiO_2/Si substrate. (b) AFM image of GaSe sheets as shown in the black square in (a) in the scale of 16 μm × 12μm.

Figure 6.5a shows the optical image with different optical contrast of exfoliated GaSe flakes with different layer number. The thinner GaSe flakes show their color to green. Figure 6.5b exhibits the AFM image of GaSe layers corresponding to the black square in the optical image in the scale of 16 μm × 12μm. 2L and 3L GaSe flakes can be further distinguished by the AFM depth profile.

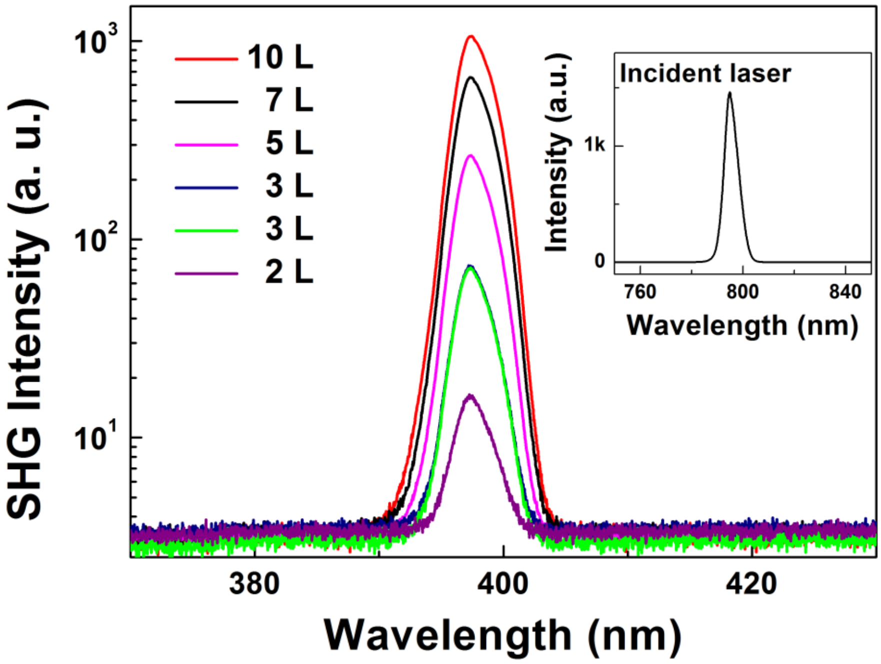

Figure 6.6 SHG from GaSe thin layers with different layer number. Inset: Incident fs laser spectrum in linear scale.

Figure 6.6 shows the SHG emission spectra from GaSe thin flakes with different layer number from 2 to 10 layers excited by femtosecond (fs) laser of 800 nm. The curves are plotted in log scale for comparison. These spectra show peaks centering at about 400 nm, confirming the observed peak is indeed at half wavelength of the fundamental laser (800 nm), as shown in the inset of Figure 6.6. Such frequency doubling is the so-called second harmonic generation, giving rise to twice the frequency and half the wavelength of the incident photons. It should be noted that when we measured 3L GaSe samples on different SiO_2 substrates, almost same SHG spectra are obtained under identical condition, as can be seen from the two curves in Figure 6.6 for 3L GaSe flakes. Therefore, we can keep the stability and repeatability of the emission spectra for GaSe layers on different SiO_2 substrates in order to compare accurately the SHG response from layered GaSe samples with different thickness. It should be noticed that a strong emission response of can be detected from bilayer (2L) GaSe flake. Therefore, second harmonic emission can arise from a bilayer GaSe sheet. This implies that bilayer GaSe sheet is of non-centrosymmetric structure due to the absence of the inversion center. In fact, single-layer TMDCs, like MoS_2 and WS_2 nanosheets, were reported to show second order optical nonlinearity due to the absence of inversion symmetry.[103–106] The SHG was only observed in odd-layered TMDCs nanosheets, while vanished or degraded in even layer numbers owing to the restoration of inversion symmetry. SHG can also be observed in artificially stacked TMDCs bilayers with an arbitrary stacking angle and *h*-BN bilayers with broken inversion symmetry.[107,108]

The log vs log plot of SHG intensity with dependence on the GaSe layer number is shown in Figure 6.7. By linearly fitting the SHG intensity points, a slope of 3.12 can be obtained when the GaSe crystal is thinner than 5L, indicating an approximately cubic dependence of SHG intensity on the layer number. On the other hand, when the thickness is in access of 5L, a quadratic dependence on the thickness of SHG can be linearly fitted with a slope of 2.00.

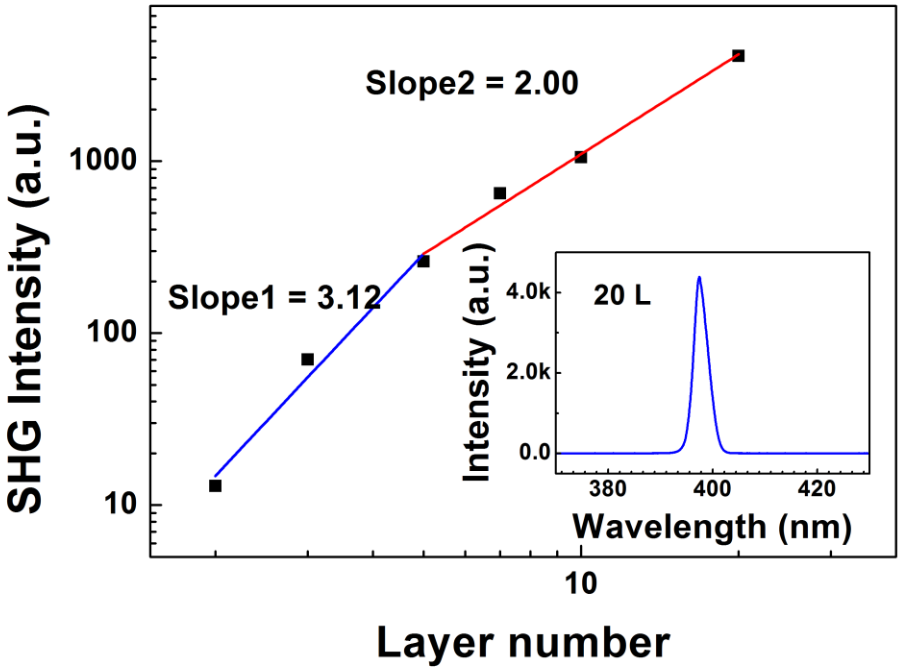

Figure 6.7 The SHG intensity as a function of layer number. SHG spectrum of 20L GaSe is shown in the inset.

However, in the limit that the sample thickness is much less than the coherence length, the SHG intensity generally has a quadratic-dependence on the thickness of thin film in principle.[181,182] In contrast to the very recent extensive study in the nonlinear optical properties of 2D TMDCs, little is known about their nonlinear optical properties of GaSe flakes with several-nanometer thickness. And for GaSe, investigation of thickness dependent second-harmonic intensity only was concentrated on thin films with thickness of tens of nanometer, in which defects cannot be ruled out.[183] In principle, in the limit that the sample thickness is much less than the coherence length, the SHG intensity has been reported to possess a quadratic-dependence on the thickness of thin film.[181,182] Such a discrepancy can be interpreted that the nonlinear coefficient is changed in GaSe nanosheets compared to their bulk one. In the case where sample thickness (l) is less than the coherence length (l_c), the SHG intensity can be expressed as:

$$I(2\omega,l)=\frac{2\omega^2 d_{\mathrm{eff}}^2 l^2}{n_{2\omega}n_\omega^2 c^3\varepsilon_0}\left(\frac{\sin(\pi l/l_c)}{\pi l/l_c}\right)^2 I^2(\omega) \quad (6.1)$$

where ω is the input frequency, d_{eff} is the nonlinear coefficient, c is the speed of light in a vacuum, ε_0 is vacuum dielectric constant, $n_{2\omega}$ and n_ω are the index of refraction at second harmonic and fundamental frequencies, respectively. When $l \ll l_c$, $\frac{\sin(\pi l/l_c)}{\pi l/l_c} \approx 1$. And, the SHG is not influenced by phase-matching conditions. So, we can obtain:

$$I(2\omega,l)=\mathrm{A}d_{\mathrm{eff}}^2 l^2 I^2(\omega). \quad (6.2)$$

Where $\mathrm{A}=\frac{2\omega^2}{n_{2\omega}n_\omega^2 c^3\varepsilon_0}$

In order to estimate the magnitude of d_{eff} of few-layer GaSe from the measurement, we model few-layer one as a bulk medium. Since the nonlinear coefficient is of structural origin, it is reasonable to consider that its 20-nm-thick scale value is not distinct from the bulk one. The SHG spectrum of 20L GaSe sheet is shown in the inset of Figure 6.7. So, according to the SHG intensity of different thickness, we can estimate their nonlinear coefficient. The estimation was done by comparing the emission intensity of few-layer GaSe sheet to the 20L one with the nonlinear coefficient of 54 pm/V. The nonlinear coefficient is estimated to be 30 and 46.3 pm/V for 2L and 3L GaSe, respectively. Although the SHG of GaSe sheets is degraded in bilayer and trilayer, multilayer GaSe sheets possess a comparable nonlinear coefficient to the bulk one when thickness is above 5L. Nevertheless, the nonlinear coefficient of our few-layer GaSe is relatively high in comparison with some other nonlinear bulk and thin film materials.[184,185]

The anomalous behaviors in second harmonic response may be related to the energy stability of stacking sequence in 2D GaSe sheets. In bulk, both β- and ε-GaSe are stable with an interlayer coupling effect by van der Waals force. However, their coupling energies should be different due to distinct stacking sequence and the impact of such discrepancy may be more remarkable in low dimension. Specifically, despite of the identical interlayer distances in both modifications, the spacing between a Ga and the nearest Se in the adjacent layer is distinct. The spacing in ε-GaSe is larger than β, resulting in a weaker interlayer coupling energy. External perturbations, such as thermal excitation, photoexcitation, may modify the stacking order at atomically thin films from ε-GaSe to β-GaSe, which consequently give rise to centrosymmetry of the whole sample. To verify this hypothesis, the free energy calculation for bulk and 2D layered ε- and β-GaSe was performed using first-principles method with the CASTEP package.[186] The final lowest energy of each modification is obtained after a geometry optimization to their structures, as shown in as shown in Table 6.1.

Table 6.1 The calculated free energy of bulk, bilayer, trilayer *β*- and *ε*-GaSe and the energy difference between the two polytype.

layer	*ε*-Gase	*β*-GaSe	Difference
Bulk	-9262.109 eV	-9262.106 eV	-0.003 eV
Bilayer	-9261.253 eV	-9261.998 eV	0.745 eV
Trilayer	-13891.769 eV	-13893.052 eV	1.283 eV

In our calculation, the unit cell in bulk contains 2 basic layers by considering the periodicity, while bilayer and trilayer GaSe consists of 2 and 3 basic layers, respectively, with breaking the periodicity on the z-axis. This can result in the energy of trilayer is approximately 1.5 times the magnitude of bilayer and bulk. The lattice parameters of *ε*- and *β*-GaSe are tuned into same value (a = b = 3.750Å, c = 15.94Å) for the better comparison of the stacking sequence. In bulk, the energies of *β*- and *ε*-GaSe are very similar with tiny difference of -0.00327 eV. However, the energy of *ε*-GaSe is higher than that of *β*-GaSe in bilayer, indicating bilayer *ε*-GaSe is less stable than *β*-GaSe. Similar energy difference between *β*- and *ε*-GaSe also can be obtained for trilayer GaSe. The energy calculation means both *β*- and *ε*-GaSe are stable in bulk with small energy difference. However, in the atomically thin flakes, larger energy difference suggests that layer-layer stacking order tends to favor *β*-polytype. This can induce the degradation of SHG in bi-and trilayer GaSe.

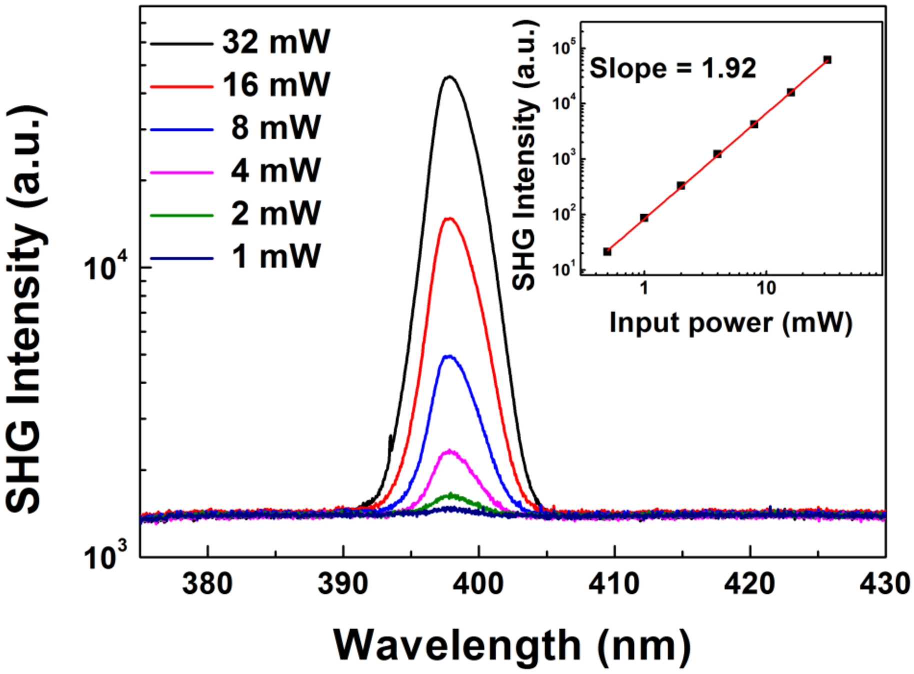

Figure 6.8 Spectra of second harmonic generation from the GaSe thin layer with different input power. Inset: the input power dependent SHG intensity from the GaSe sheet.

To further determine the SHG response of GaSe excited by fs laser of 800 nm, the SHG intensity was measured as a function of the power of fundamental excitation. Figure 6.8 shows the spectra of SHG for a thin layer of GaSe flake with different input power. With the input power is increased gradually from 1 to 32 mW, the SHG peak is dramatically enhanced. The inset of Figure 6.8 shows log vs log plot of the power dependence of SHG on the fundamental excitation power. The fitting line demonstrates a quadratic-dependence as expected in nonlinear optical bulk materials.[187] The power dependence can be linear fitted with a slope of 1.92, which can further confirm the sharp and strong peak at 400 nm is the second harmonic response of the initial input with the wavelength of 800 nm.

Above mentioned results show the second harmonic response of the specific point in the GaSe nanosheets with different thickness and input power. It is also essential to characterize the second harmonic response for the overall GaSe flakes. CLSM is a powerful technique to obtain high resolution optical images with selective depth. In our experiment, the exited laser can be tuned from 680 to 1080 nm. GaSe flakes were prepared on a transparent substrate so that the signal could be detected by the confocal microscope in transmissive mode.

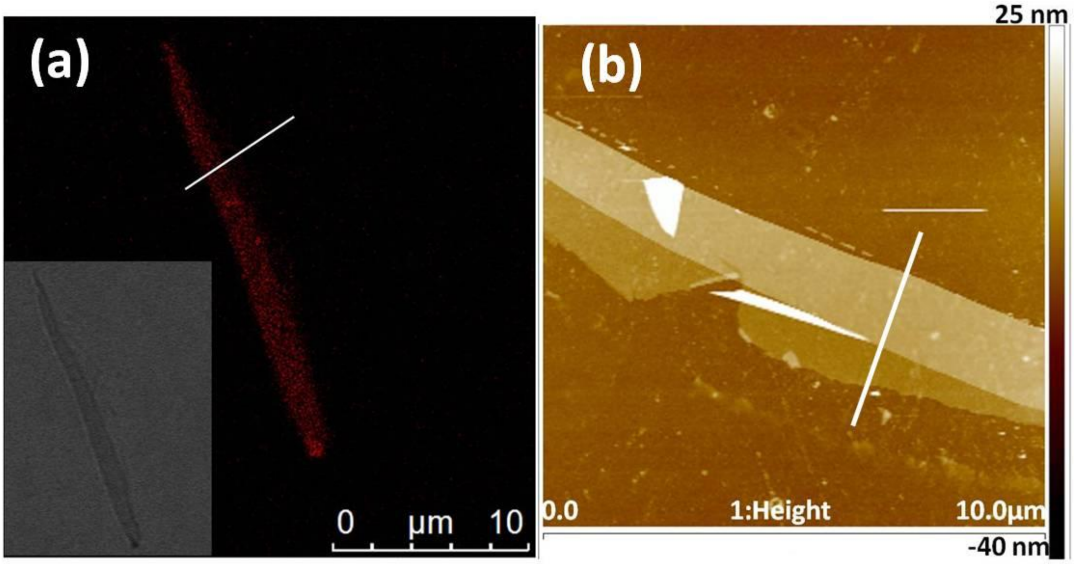

Figure 6.9 (a) Confocal laser scanning microscope SHG image excited by 976 nm laser with emission filter range from 450 to 500 nm. The inset shows the bright field image of this GaSe nanosheet. (b) The corresponding AFM image of the corresponding mechanically exfoliated GaSe layers on the transparent glass substrate.

Figure 6.9a shows the SHG image excited by 976 nm laser with emission filter range from 450 to 500 nm for a GaSe sample and the AFM image of the GaSe layers on transparent glass substrate. The emission is very weak but still visible for 5L GaSe thin layers, in comparison with its 10L ones. The inset in Figure 6.9a shows the corresponding bright field image of the GaSe flakes. The corresponding AFM image of the corresponding mechanically exfoliated GaSe layers on transparent glass substrate is shown in Figure 6.9b.

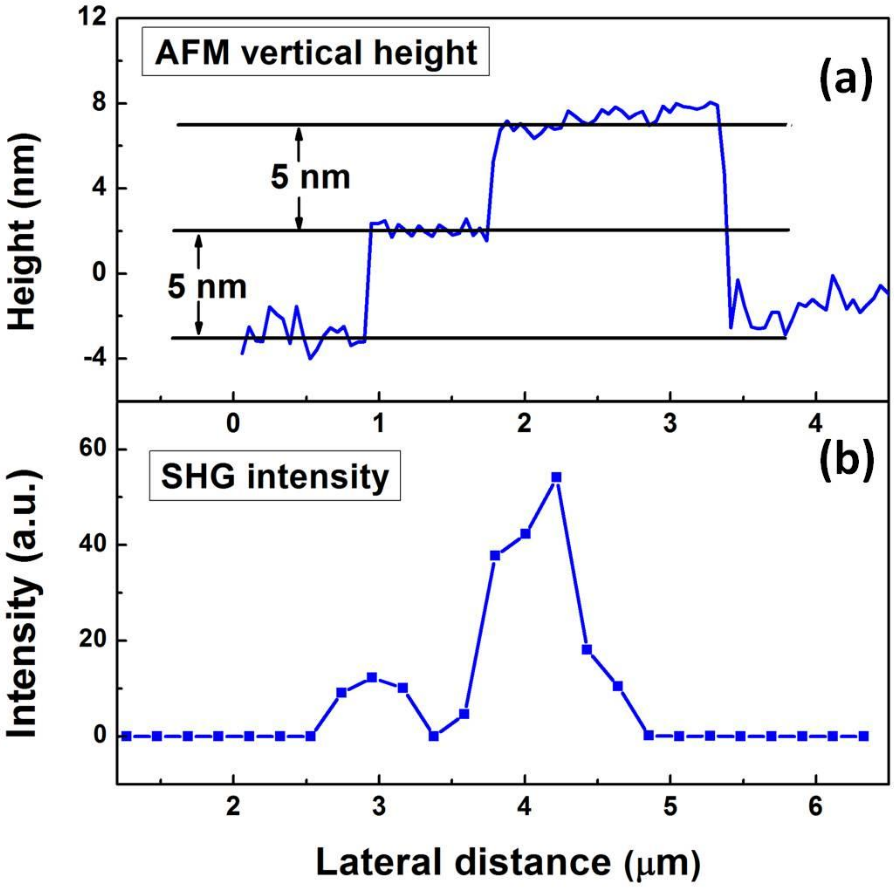

Figure 6.10 (a) AFM height profile for the GaSe sample on transparent glass substrate in Figure 6.9b. (b) Intensity profile of the SHG from right to left at the white line shown in Figure 6.9a.

Figure 6.10a demonstrates the corresponding AFM height profile for the GaSe sample shown in Figure 6.9, which clearly indicates the thickness of 5 nm and 10 nm for GaSe flakes. The SHG intensity profile of fluorescent image for the GaSe flakes with thickness of 5 nm and 10 nm is shown in Figure 6.10b. The SHG intensity of 10L GaSe flake is about 4 times intensity of 5L GaSe one.

The SHG emission spectrum can also be measured by the confocal scanning system. Under an excitation of 976 nm, strong and eminent blue emission (488 nm) can be observed in the GaSe flakes with different thickness, as shown in Figure 6.11. It should be noted that the fs laser with various wavelength from 900 to 1080 nm can give rise to second harmonic response for GaSe sheets. By switching the excited laser from 900 nm to 1080 nm, the luminescence peak shows corresponding shift from 450 nm to 540 nm, as shown in Figure 6.11. The results provide further evidence of the realization of the frequency doubling from the nonlinear material of GaSe even down to atomic-layer.

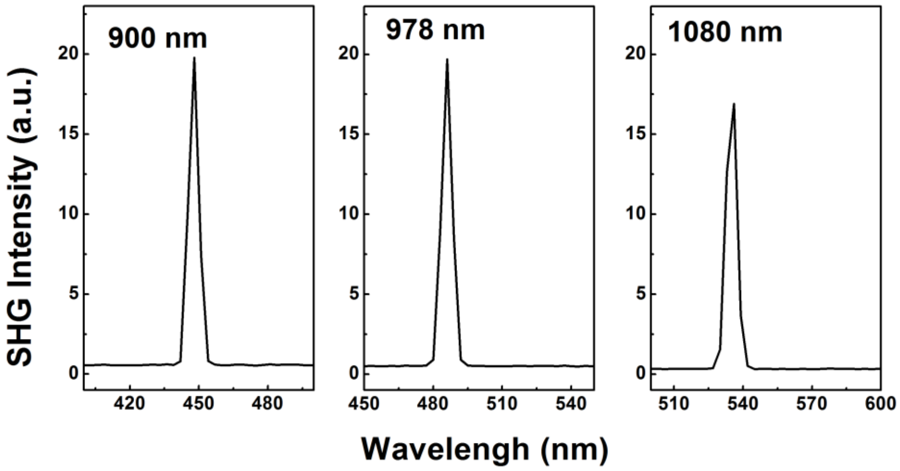

Figure 6.11 The SHG spectra of GaSe thin flakes with the excited laser of 900, 976, 1080 nm, respectively.

To further investigate the nonlinear optical properties using the CLSM, another set of GaSe flakes was prepared on a transparent glass substrate. Figure 6.12a shows the bright field image of GaSe flakes on a transparent glass substrate. AFM was used to determine the layer thickness, as shown in the inset of Figure 6.12a, indicating 7L and 15L GaSe flakes. Figure 6.12b shows a representative bright field image of few-layer GaSe sheets. The SHG image with emission filter from 450 to 500 nm clearly shows the thickness-dependent optical contrast. Although AFM is an accurate method to identify the layer number, it is time-consuming and scale-limited. On the basis of the different emission intensity in the SHG image, we can estimate the thickness of the GaSe layers. This provides a rapid way to characterize large-scale GaSe layers, which is more efficient than AFM. It was recently reported that an optical imaging technique was developed by utilizing the edge effects of nonlinear optical response for monolayer MoS_2.[188] Although the evaluation of layer number is not sufficiently precise, it still shows potential in future for rapidly estimating the layer number and accurately determining the shape and location for few-layer GaSe nanosheets. The overlay image of bright field and SHG image for GaSe flakes suggests the SHG can be utilized as an effective method to find the location of GaSe sheets, as shown in Figure 6.13.

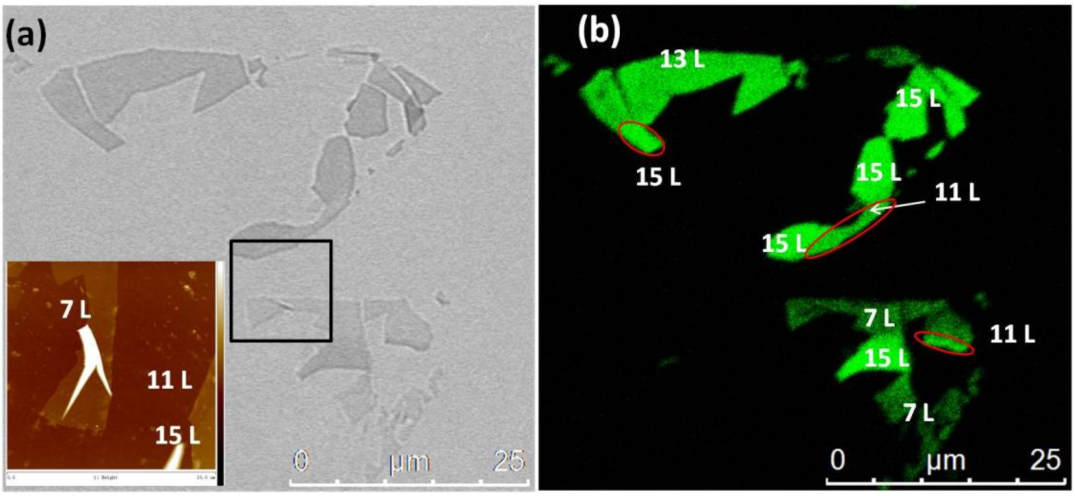

Figure 6.12 Confocal laser scanning microscope image of layered GaSe flakes on transparent glass substrate (a) the bright filed image; (b) the SHG image with emission filter ranging from 450 to 500 nm.

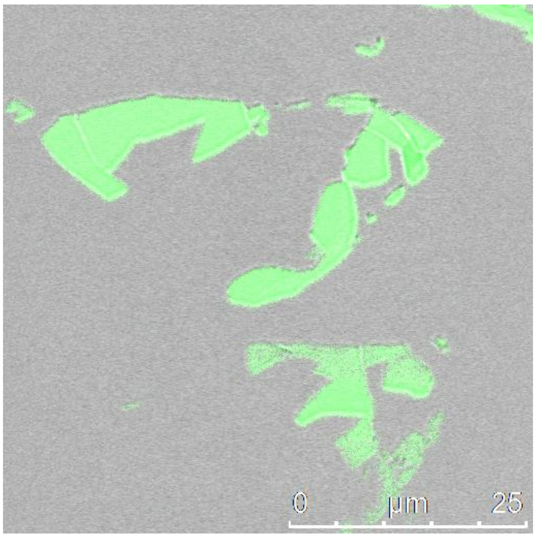

Figure 6.13 The overlay image of the bright field and the corresponding SHG image for GaSe flakes.

6.4 Two-photon excited fluorescence of GaSe nanosheets

In theory, SHG involves that two photons interact simultaneously with the nonlinear material with no absorption process, which is essentially a scattering process. However, two-photon excited fluorescence (TPEF) is a third order optical process involving absorption of the two photons and then emission of radiation. In this process, two-photon absorption (TPA) is the simultaneous absorption of two photons, which usually takes place when the excitation is a pulse wave with high intensity. In particular, TPA is a nonlinear optical process being several orders of magnitude weaker than linear absorption, i.e., one photon absorption (OPA).[189,190] It is clear that TPEF is also a nonlinear optical process. However, for TPEF, the nonlinear material is not essential. The difference between SHG and TPEF is that the nonlinear material with a noncentrosymmetric structure is essential for SHG.

It is common to observe both SHG and TPEF to achieve high resolution imaging for biological tissues and organic nanocrystals.[191,30] Especially, it was reported that TPEF and SHG could both be observed in odd layer 2D WS_2 layers.[194] So, it is also interesting and essential to investigate the TPEF of GaSe nanosheets in order to understand their nonlinear optical properties. By changing the emission filter range to from 600 to 700 nm, a dim but still visible fluorescent image analogous to the bright field can be obtained. The emission image is shown in Figure 6.14. This image may result from TPEF considering the excited laser is of high intensity and the band gap of GaSe is about 2.0 eV.

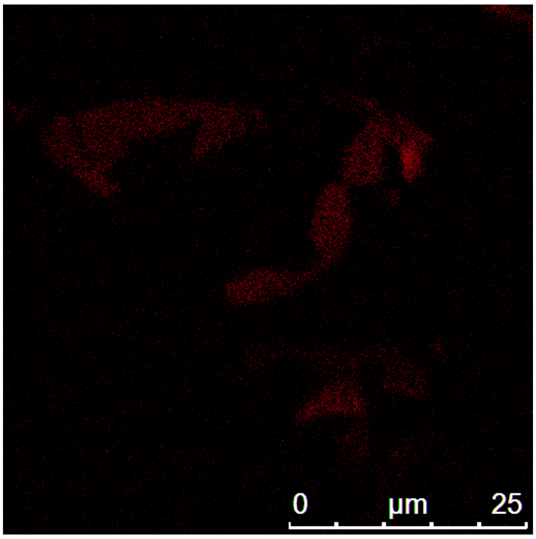

Figure 6.14 The fluorescent image with emission filter ranging from 600 to 700 nm.

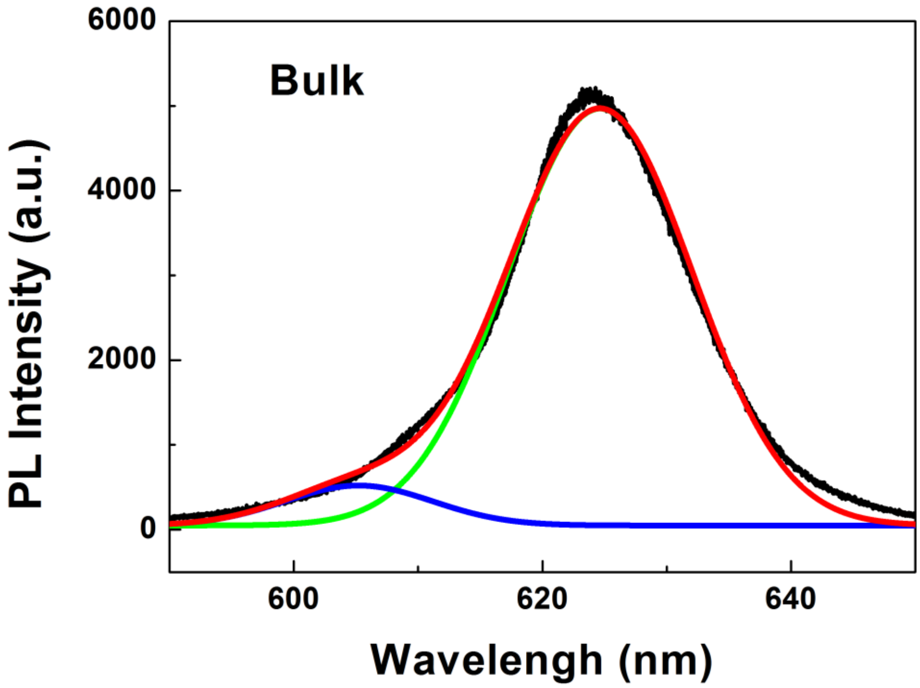

Figure 6.15 PL spectrum of bulk GaSe excited by 488-nm cw laser.

To fully understand TPEF of GaSe nanosheets, the photoluminescence (PL) of bulk GaSe samples induced by direct OPA excited by 488 nm continuous wave (cw) laser and nonlinear TPA excited by 800 nm fs laser was studied, respectively.

One-photon PL spectrum of bulk GaSe is shown in Figure 6.15. The PL peak shows at about 620 nm, indicating a band gap of about 2.0 eV. There is a significant shoulder peak at the red side of the feature peak. As a consequence, this peak can be well described by a superposition (red line) of two Gauss peaks, which center at 605 nm (blue line) and 624 nm (green line), corresponding to photon energies of 2.051 eV and 1.989 eV, respectively. This may be caused by the two different modifications of H-stacking of the GaSe, i.e., β- and ε-GaSe. At 300 K, the band gap of β- and ε-GaSe is about 2.046 and 1.996 eV, respectively.[195] It should be noted that the later shows relatively strong PL peak compared to the former, with an intensity ratio of in excess of 10. This PL spectrum also indicates the main modification of our GaSe crystal is noncentrosymmetric ε-GaSe.

TPEF of the bulk GaSe was measured using 800 nm fs laser to investigate the nonlinear third order response, as shown in Figure 6.16. The spectrum also shows a peak at about 620 nm, and the peak can be fitted by two peaks with center positions (phonon energies) of 605 nm (2.051 eV) and 620 nm (2.001 eV). Similar to OPA induced PL, the intensity of TPEF peak of ε-GaSe is much higher than that of β-GaSe, further indicating the major modification of bulk GaSe samples is ε-type.

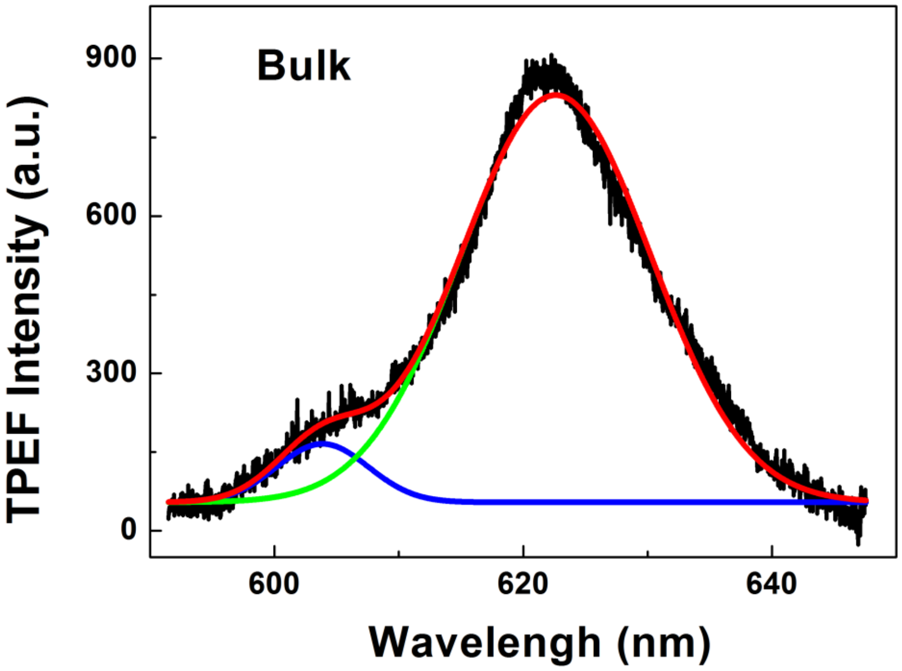

Figure 6.16 Two-photon excited fluorescence spectrum excited by 800-nm fs laser for bulk GaSe.

For cleaved layered-GaSe with atomic-layer thickness, the band gap is gradually increased to about 2.1 eV. Figure 6.17 shows the PL spectrum of several-layer GaSe on SiO_2. The PL peak is analogous to that of the bulk GaSe and can be resolved into two peaks, which center at 596 nm and 611 nm, respectively. The blue shift of the two peaks indicates a larger band gap (2.082 eV and 2.031 eV) compared with their bulk counterparts. Such increase of 30 meV has been achieved by exfoliated GaSe to atomic layer thickness. This slight blue shift is possibly due to the modification of band structure caused by the decrease of layered GaSe in thickness, differing from the quantum confinement effect.[23,25] Additionally, the PL intensity is significantly weakened with a decrease in layer number, compared to that of bulk GaSe. This behavior is different from MoS_2, whose band gap is changed from in-direct to direct as the thickness decreases to monolayer, resulting in an enhancement of PL.

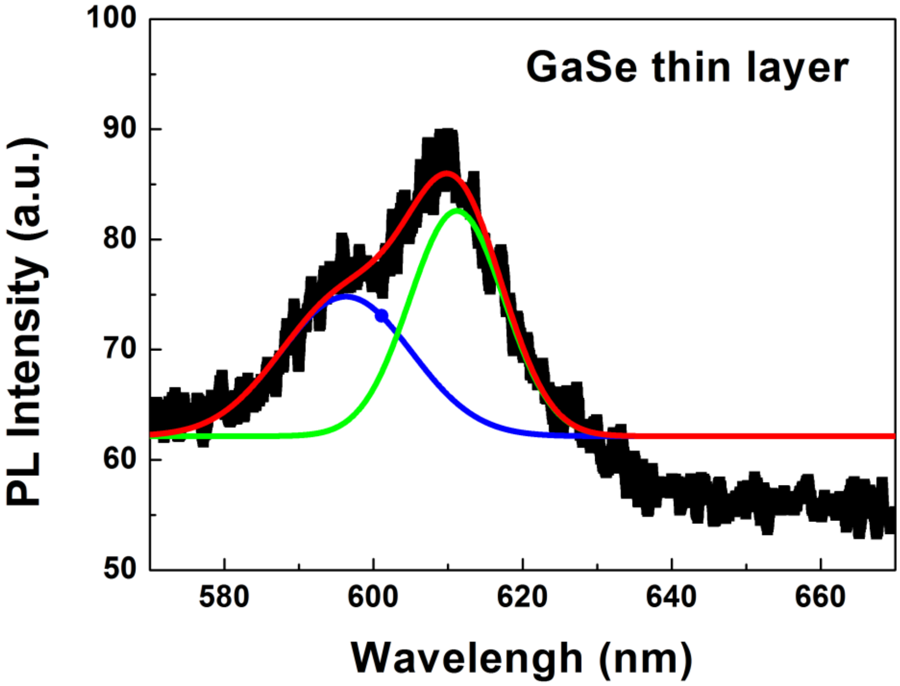

Figure 6.17 PL spectrum of GaSe nanosheets excited by 488-nm cw laser.

The TPEF of 2D GaSe has also been investigated and the spectrum is shown in Fig.ure 6.18. The TPEF spectrum can also be described by a superposition of two peaks, centering at 595 nm and 610 nm, respectively. This indicates the slight blue shift of layered GaSe sheets in comparison to the bulk crystal.

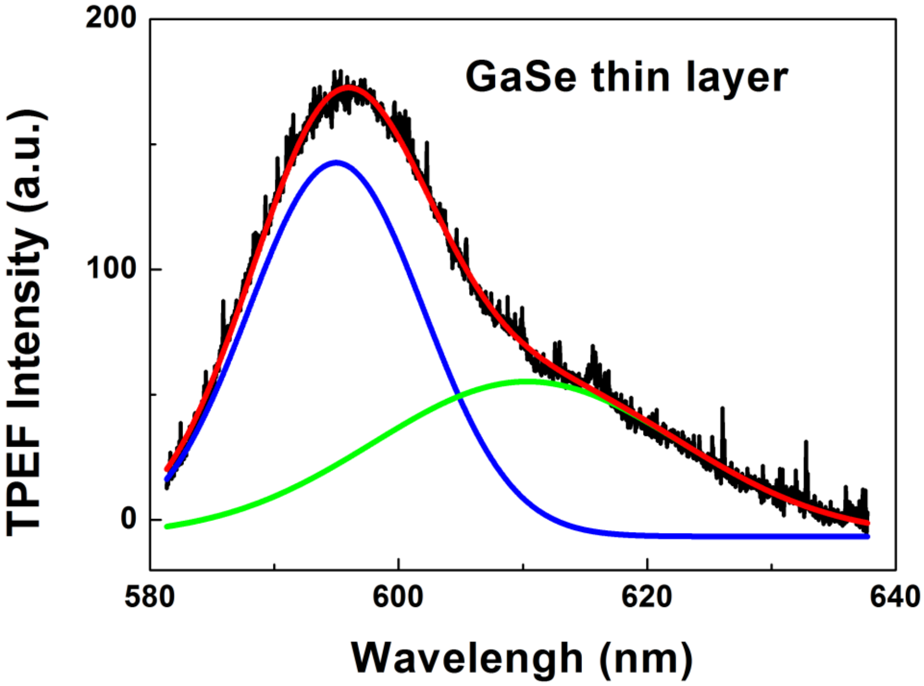

Figure 6.18 Two-photon excited fluorescence spectrum excited by 800-nm fs laser for GaSe nanosheets.

Table 6.2 Peak central positions of bulk and 2D layered GaSe samples with two modifications attracted from PL and TPEF spectra.

Position	Bulk β-GaSe	Bulk ε-Gase	2D β-Gase	2D ε-Gase
PL	605 nm	624 nm	596 nm	611 nm
TPEF	605 nm	620 nm	595 nm	610 nm

From both the PL and TPEF spectra, there is a blue shift in the emission peak position can be found from bulk to 2D thin layer for both ε- and β-GaSe. The blue shift can be clearly seen from Table 6.2 which summarizes the central peak positions of bulk and 2D layered GaSe samples with two modifications attracted from PL and TPEF spectra. However, we also notice the intensity ratio of the two peaks is changed from bulk to 2D thin layers. In bulk, the intensity of *ε*-Gase is much higher than that of *β*-Gase, while, in 2D forms, comparable intensity for two modifications can be achieved. This also can be well explained by the calculation result which is stacking order at atomically thin films tends to form *β*-GaSe modification.

6.5 Summary

We have observed the nonlinear properties of SHG and TPEF in few-layer GaSe sheets. Especially, bilayer GaSe sheet is capable of demonstrating strong second harmonic response when excited by fs pulse laser. The SHG response of GaSe nanosheets smaller than 5L shows a nearly cubic dependence on the layer number, differing from the quadratic dependence of GaSe sheets with the thickness beyond 5L. This can be attributed to the weakened stability of *ε*-GaSe in the atomically thin flakes. First-principles calculations indicate that the stacking order at atomically thin films tends to form *β*-GaSe modification with centrosymmetric structure which is not capable of possessing nonlinear optical properties. SHG and TPEF have also simultaneously been observed in few-layer GaSe sheets by CLSM, suggesting an efficient and rapid way in determining the layer number and location of GaSe nanosheets. At any rate, our results firstly provide experimental evidence that the intrinsic nonlinear optical properties can be maintained even when the thickness of GaSe is decreased to bilayer. In the view of applications, the observation in this work suggests that 2D layered GaSe sheets with strong second harmonic response can be considered as a promising candidate for the future nanophotonic devices.

Chapter 7 **Conclusion and Future Prospect**

7.1 **Conclusion**

In conclusion, huge effort has been devoted to the research of 2D materials in view of their promising applications. Hybrid structures of graphene combined with ferroelectric or semiconductor show fascinating behaviors and practical applications. Besides, the nonlinear optical properties of 2D layered GaSe sheets have been studied. In this thesis, we perform the characterization of CVD-grown graphene-based electronic and optoelectronic devices as well as the pristine nonlinear behaviors of mechanically exfoliated GaSe nanosheets.

Firstly, we present the transport and vibrational properties of the graphene based on a graphene/PMN-PT hybrid system. The graphene/PMN-PT FETs show p-type behaviors and exhibit a large memory window in contrast to conventional graphene/SiO_2 FETs. The on/off ratio, field effect mobility and excess hole concentration are calculated to be about 5.5, 4.52×10^3 $cm^2v^{-1}s^{-1}$ and 6.74×10^{12} cm^{-2}, respectively. A reduction in p-doping for graphene FETs can be obtained through pre-polarization of PMN-PT substrate. Temperature-dependent R_s of graphene exhibits a metallic behavior and the R_s of graphene on the PMN-PT substrate can be reduced to about 1.25 kΩ/sq. On the other hand, PMN-PT serves as an actuator to provide controllable biaxial strain to the above CVD-grown graphene layer, and such strain can result in a blue shift in the 2D band. We present the *in-situ* and real-time Raman spectra of graphene under such biaxial strain. The actual amount of strain exerted on the graphene is much smaller than that provided by the PMN-PT. After the initial response to the applied voltage, a continuous blue shift can be detected during the retention of bias voltage. The time-dependent Raman shift could be ascribed to the different strain distribution in CVD-grown graphene.

Secondly, p-type GaAs can form ohmic contact with both the CVD-grown SLG and BLG sheets, while n-type GaAs can be combined with such graphene layers to form Schottky junctions. We have firstly demonstrated photovoltaic characteristics of graphene-on-GaAs Schottky junction with the V_{oc} of 0.65 V, J_{sc} of 10.03 mA/cm^2 and PCE value of 1.95 %. Such performance parameters of the device are comparable to or even higher than those of other pristine graphene/semiconductor junction-based devices. Our calculations based on the rectifying characteristics of the diodes suggest that bilayer graphene/GaAs junction exhibits smaller ideality factor (2.43), higher Schottky barrier height (0.75 eV), and lower series resistance (20.1 Ω) compared to single-layer one, which can give rise to the improved photovoltaic behaviors of BLG-based junction solar cells. This work implies that the developed graphene/GaAs system can be processed to be a new system for future photovoltaic applications considering the high-performance of optoelectronic capabilities of radiation-resistant GaAs wafer.

Thirdly, the nonlinear properties of SHG and TPEF have been studied in few-layer GaSe sheets. Especially, bilayer GaSe sheet is capable of demonstrating strong second harmonic response when excited by fs pulse laser. The SHG response of GaSe nanosheets smaller than 5L shows a nearly cubic dependence on the layer number, differing from the quadratic dependence of GaSe sheets with the thickness beyond 5L. This can be attributed to the weakened stability of ε-GaSe in the atomically thin flakes. First-principles calculations indicate that the stacking order at atomically thin films tends to form β-GaSe modification with centrosymmetric structure which is not capable of possessing nonlinear optical properties. SHG and TPEF have also simultaneously been observed in few-layer GaSe sheets by CLSM, suggesting an efficient and rapid way in determining the layer number and location of GaSe nanosheets. At any rate, our results firstly provide experimental evidence that the intrinsic nonlinear optical properties can be maintained even when the thickness of GaSe is decreased to bilayer. In the view of applications, the observation in this work suggests that 2D layered GaSe sheets with strong second harmonic response can be considered as a promising candidate for future nanophotonic devices.

7.2 Future Prospect

In future, some optoelectronic devices will be fabricated in aim to utilizing the strong second harmonic response of GaSe nanosheets. Few-layer GaSe sheets can achieve the frequency doubling, which is very essential in nano devices. In order to do this, we should achieve the stability and reproducibility as well as the endurance to air ambient of GaSe sheets. More importantly, it is expected that devices with new functions and better performance are expected to be realized by choosing this nonlinear 2D materials with optimum device design.

On the other hand, it has been proven feasible to integrate two types of low-dimensional materials, such as combining graphene with other 2D layered semiconductors of MoS_2[196] and WS_2[197,198] or insulator of hBN,[199–201] or 1D carbon nanotubes[202,203] to obtain some nanoelectronic or nanophotonic devices with novel functions. This concept provides us opportunity to integrate our previous studied 2D materials to pursue some new functional devices.

References

(1) Novoselov, K. S.; Geim, A. K.; Morozov, S. V.; Jiang, D.; Zhang, Y.; Dubonos, S. V.; Grigorieva, I. V.; Firsov, A. A. Electric Field Effect in Atomically Thin Carbon Films. *Science* **2004**, *306*, 666–669.

(2) Bianco, A.; Cheng, H.-M.; Enoki, T.; Gogotsi, Y.; Hurt, R. H.; Koratkar, N.; Kyotani, T.; Monthioux, M.; Park, C. R.; Tascon, J. M. D. *et al.* All in the Graphene Family – A Recommended Nomenclature for Two-dimensional Carbon Materials. *Carbon* **2013**, *65*, 1–6.

(3) Freitag, M. Graphene: Nanoelectronics Goes Flat Out. *Nat. Nanotechnol.* **2008**, *3*, 455–457.

(4) Geim, A. K.; Novoselov, K. S. The Rise of Graphene. *Nat. Mater.* **2007**, *6*, 183–191.

(5) Geim, A. K. Graphene: Status and Prospects. *Science* **2009**, *324*, 1530–1534.

(6) Morozov, S.; Novoselov, K.; Katsnelson, M.; Schedin, F.; Elias, D.; Jaszczak, J.; Geim, A. K. Giant Intrinsic Carrier Mobilities in Graphene and Its Bilayer. *Phys. Rev. Lett.* **2008**, *100*, 016602.

(7) Chen, J.; Jang, C.; Adam, S.; Fuhrer, M. S.; Williams, E. D.; Ishigami, M. Charged-impurity Scattering in Graphene. **2008**, *3*, 377–381.

(8) Chen, J.-H.; Jang, C.; Xiao, S.; Ishigami, M.; Fuhrer, M. S. Intrinsic and Extrinsic Performance Limits of Graphene Devices on SiO2. *Nat. Nanotechnol.* **2008**, *3*, 206–209.

(9) Berry, V. Impermeability of Graphene and Its Applications. *Carbon* **2013**, *62*, 1–10.

(10) Zhao, Y.; Xie, Y.; Hui, Y. Y.; Tang, L.; Jie, W.; Jiang, Y.; Xu, L.; Lau, S. P.; Chai, Y. Highly Impermeable and Transparent Graphene as an Ultra-thin Protection Barrier for Ag Thin Films. *J. Mater. Chem. C* **2013**, *1*, 4956–4961.

(11) Balandin, A. A.; Ghosh, S.; Bao, W.; Calizo, I.; Teweldebrhan, D.; Miao, F.; Lau, C. N. Superior Thermal Conductivity of Single-Layer Graphene 2008. *Nano Lett.* **2008**, *8*, 902–907.

(12) Li, X.; Zhu, Y.; Cai, W.; Borysiak, M.; Han, B. Transfer of Large-area Graphene Films for High-performance Transparent Conductive Electrodes. *Nano Lett.* **2009**, *9*, 4359–4363.

(13) Lee, C.; Wei, X.; Kysar, J. W.; Hone, J. Measurement of the Elastic Properties and Intrinsic Strength of Monolayer Graphene. *Science* **2008**, *321*, 385–388.

(14) Bao, Q.; Loh, K. P. Graphene Photonics, Plasmonics, and Broadband Optoelectronic Devices. *ACS Nano* **2012**, *6*, 3677–3694.

(15) Zhu, Y.; Murali, S.; Cai, W.; Li, X.; Suk, J. W.; Potts, J. R.; Ruoff, R. S. Graphene and Graphene Oxide: Synthesis, Properties, and Applications. *Adv. Mater.* **2010**, *22*, 3906–3924.

(16) Novoselov, K. S.; Jiang, Z.; Zhang, Y.; Morozov, S. V.; Stormer, H. L.; Zeitler, U.; Maan, J. C.; Boebinger, G. S.; Kim, P.; Geim, A. K. Room-Temperature Quantum Hall. *Science* **2007**, *315*, 1379.

(17) Schwierz, F. Graphene Transistors. *Nat. Nanotechnol.* **2010**, *5*, 487–496.

(18) Mas-Ballesté, R.; Gómez-Navarro, C.; Gómez-Herrero, J.; Zamora, F. 2D Materials: To Graphene and Beyond. *Nanoscale* **2011**, *3*, 20–30.

(19) Novoselov, K. S.; Jiang, D.; Schedin, F.; Booth, T. J.; Khotkevich, V. V.; Morozov, S. V.; Geim, A. K. Two-dimensional Atomic Crystals. *Proc. Nati. Acad. Sci. USA* **2005**, *102*, 10451–10453.

(20) Mak, K. F.; Lee, C.; Hone, J.; Shan, J.; Heinz, T. F. Atomically Thin MoS2: A New Direct-Gap Semiconductor. *Phys. Rev. Lett.* **2010**, *105*, 136805.

(21) Late, D. J.; Liu, B.; Matte, H. S. S. R.; Rao, C. N. R.; Dravid, V. P. Rapid Characterization of Ultrathin Layers of Chalcogenides on SiO2/Si Substrates. *Adv. Funct. Mater.* **2012**, *22*, 1894–1905.

(22) Lei, S.; Ge, L.; Liu, Z.; Najmaei, S.; Shi, G.; You, G.; Lou, J.; Vajtai, R.; Ajayan, P. M. Synthesis and Photoresponse of Large GaSe Atomic Layers. *Nano Lett.* **2013**, *13*, 2777–2781.

(23) Hu, P.; Wen, Z.; Wang, L.; Tan, P.; Xiao, K. Synthesis of Few-layer GaSe Nanosheets for High Performance Photodetectors. *ACS Nano* **2012**, *6*, 5988–5994.

(24) Hu, P.; Wang, L.; Yoon, M.; Zhang, J.; Feng, W.; Wang, X.; Wen, Z.; Idrobo, J. C.; Miyamoto, Y.; Geohegan, D. B. *et al.* Highly Responsive Ultrathin GaS

Nanosheet Photodetectors on Rigid and Flexible Substrates. *Nano Lett.* **2013**, *13*, 1649–1654.

(25) Late, D. J.; Liu, B.; Luo, J.; Yan, A.; Matte, H. S. S. R.; Grayson, M.; Rao, C. N. R.; Dravid, V. P. GaS and GaSe Ultrathin Layer Transistors. *Adv. Mater.* **2012**, *24*, 3549–3554.

(26) Zheng, Y.; Ni, G.-X.; Toh, C.-T.; Zeng, M.-G.; Chen, S.-T.; Yao, K.; O¨ zyilmaz, B. Gate-controlled Nonvolatile Graphene-ferroelectric Memory. *Appl. Phys. Lett.* **2009**, *94*, 163505.

(27) Hong, X.; Hoffman, J.; Posadas, A.; Zou, K.; Ahn, C. H.; Zhu, J. Unusual Resistance Hysteresis in N-layer Graphene Field Effect Transistors Fabricated on Ferroelectric Pb (Zr0 . 2Ti0 . 8) O3 Unusual Resistance Hysteresis in N-layer Graphene Field Effect Transistors. *Appl. Phys. Lett.* **2010**, *97*, 033114.

(28) Song, E. B.; Lian, B.; Kim, S. M.; Lee, S.; Chung, T.; Wang, M.; Zeng, C.; Xu, G.; Wong, K.; Zhou, Y. *et al.* Robust Bi-stable Memory Operation in Single-layer Graphene Ferroelectric Memory Robust Bi-stable Memory Operation in Single-layer Graphene Ferroelectric Memory. *Appl. Phys. Lett.* **2011**, *99*, 042109.

(29) Zheng, Y.; Ni, G.-X.; Toh, C.-T.; Tan, C.-Y.; Yao, K.; Özyilmaz, B. Graphene Field-Effect Transistors with Ferroelectric Gating. *Phys. Rev. Lett.* **2010**, *105*, 166602.

(30) Hong, X.; Posadas, A.; Zou, K.; Ahn, C.; Zhu, J. High-mobility Few-layer Graphene Field Effect Transistors Fabricated on Epitaxial Ferroelectric Gate Oxides. *Phys. Rev. Lett.* **2009**, *102*, 136808.

(31) Zheng, Y.; Ni, G.-X.; Bae, S.; Cong, C.-X.; Kahya, O.; Toh, C.-T.; Kim, H. R.; Im, D.; Yu, T.; Ahn, J. H. *et al.* Wafer-scale Graphene/ferroelectric Hybrid Devices for Low-voltage Electronics. *Europhys. Lett.* **2011**, *93*, 17002.

(32) Castro, E.; Novoselov, K.; Morozov, S.; Peres, N.; dos Santos, J.; Nilsson, J.; Guinea, F.; Geim, A.; Neto, A. Biased Bilayer Graphene: Semiconductor with a Gap Tunable by the Electric Field Effect. *Phys. Rev. Lett.* **2007**, *99*, 216802.

(33) Han, M.; Özyilmaz, B.; Zhang, Y.; Kim, P. Energy Band-Gap Engineering of Graphene Nanoribbons. *Phys. Rev. Lett.* **2007**, *98*, 206805.

(34) Choi, S.-M.; Jhi, S.-H.; Son, Y.-W. Effects of Strain on Electronic Properties of Graphene. *Phys. Rev. B* **2010**, *81*, 081407(R).

(35) Cocco, G.; Cadelano, E.; Colombo, L. Gap Opening in Graphene by Shear Strain. *Phys. Rev. B* **2010**, *81*, 241412(R).

(36) Yang, H.; Heo, J.; Park, S.; Song, H. J.; Seo, D. H.; Byun, K.-E.; Kim, P.; Yoo, I.; Chung, H.-J.; Kim, K. Graphene Barristor, a Triode Device with a Gate-controlled Schottky Barrier. *Science* **2012**, *336*, 1140–1143.

(37) Tongay, S.; Schumann, T.; Miao, X.; Appleton, B. R.; Hebard, A. F. Tuning Schottky Diodes at the Many-layer-graphene/semiconductor Interface by Doping. *Carbon* **2011**, *49*, 2033–2038.

(38) Tongay, S.; Lemaitre, M.; Schumann, T.; Berke, K.; Appleton, B. R.; Gila, B.; Hebard, A. F. Graphene/GaN Schottky Diodes: Stability at Elevated Temperatures. *Appl. Phys. Lett.* **2011**, *99*, 102102.

(39) Li, X.; Zhu, H.; Wang, K.; Cao, A.; Wei, J.; Li, C.; Jia, Y.; Li, Z.; Li, X.; Wu, D. Graphene-on-silicon Schottky Junction Solar Cells. *Adv. Mater.* **2010**, *22*, 2743–2748.

(40) Tongay, S.; Schumann, T.; Hebard, A. F. Graphite Based Schottky Diodes Formed on Si, GaAs, and 4H-SiC Substrates. *Appl. Phys. Lett.* **2009**, *95*, 222103.

(41) Tongay, S.; Lemaitre, M.; Miao, X.; Gila, B.; Appleton, B.; Hebard, A. F. Rectification at Graphene-Semiconductor Interfaces: Zero-Gap Semiconductor-Based Diodes. *Phys. Rev. X* **2012**, *2*, 011002.

(42) Behura, S. K.; Mahala, P.; Ray, A.; Mukhopadhyay, I.; Jani, O. Theoretical Simulation of Photovoltaic Response of Graphene-on-semiconductors. *Appl. Phys. A* **2012**, *111*, 1159–1163.

(43) Chen, C.-C.; Aykol, M.; Chang, C.-C.; Levi, A. F. J.; Cronin, S. B. Graphene-silicon Schottky Diodes. *Nano Lett.* **2011**, *11*, 1863–1867.

(44) Munshi, A. M.; Dheeraj, D. L.; Fauske, V. T.; Kim, D.-C.; van Helvoort, A. T. J.; Fimland, B.-O.; Weman, H. Vertically Aligned GaAs Nanowires on Graphite and Few-layer Graphene: Generic Model and Epitaxial Growth. *Nano Lett.* **2012**, *12*, 4570–4576.

(45) Huang, X.; Zeng, Z.; Zhang, H. Metal Dichalcogenide Nanosheets: Preparation, Properties and Applications. *Chem. Soc. Rev.* **2013**, *42*, 1934–1946.

(46) Jie, W.; Hao, J. Graphene-based Hybrid Structures Combined with Functional Materials of Ferroelectrics and Semiconductors. *Nanoscale* **2014**, *6*, 6346–6362.

(47) Jariwala, D.; Sangwan, V. K.; Lauhon, L. J.; Marks, T. J.; Hersam, M. C. Emerging Device Applications for Semiconducting Two-Dimensional Transition Metal Dichalcogenides. **2014**, *8*, 1102–1120.

(48) Fernelius, N. Properties of Gallium Selenide Single Crystal. *Prog. Cryst. Growth Charact. Mater.* **1994**, *28*, 275–353.

(49) Segura, A.; Bouvier, J.; Andrés, M.; Manjón, F.; Munoz, V. Strong Optical Nonlinearities in Gallium and Indium Selenides Related to Inter-valence-band Transitions Induced by Light Pulses. *Phys. Rev. B* **1997**, *56*, 4075–4083.

(50) Bancelin, S.; Aimé, C.; Gusachenko, I.; Kowalczuk, L.; Latour, G.; Coradin, T.; Schanne-Klein, M.-C. Determination of Collagen Fibril Size via Absolute Measurements of Second-harmonic Generation Signals. *Nat. Commun.* **2014**, *5*, 4920.

(51) Zhao, S.; Gong, P.; Bai, L.; Xu, X.; Zhang, S.; Sun, Z.; Lin, Z.; Hong, M.; Chen, C.; Luo, J. Beryllium-free Li4Sr(BO3)2 for Deep-ultraviolet Nonlinear Optical Applications. *Nat. Commun.* **2014**, *5*, 4019.

(52) Weiss, N. O.; Zhou, H.; Liao, L.; Liu, Y.; Jiang, S.; Huang, Y.; Duan, X. Graphene: An Emerging Electronic Material. *Adv. Mater.* **2012**, *24*, 5782–5825.

(53) Giovannetti, G.; Khomyakov, P.; Brocks, G.; Karpan, V.; van den Brink, J.; Kelly, P. Doping Graphene with Metal Contacts. *Phys. Rev. Lett.* **2008**, *101*, 026803.

(54) Lee, J. S.; Ryu, S.; Yoo, K.; Choi, I. S.; Yun, W. S.; Kim, J. Origin of Gate Hysteresis in Carbon Nanotube Field-Effect Transistors. *J. Phys. Chem. C* **2007**, *111*, 12504–12507.

(55) Hsieh, C.-Y.; Chen, Y.-T.; Tan, W.-J.; Chen, Y.-F.; Shih, W. Y.; Shih, W.-H. Graphene-lead Zirconate Titanate Optothermal Field Effect Transistors. *Appl. Phys. Lett.* **2012**, *100*, 113507.

(56) Wu, T.; Bur, A.; Wong, K.; Zhao, P.; Lynch, C. S. Electrical Control of Reversible and Permanent Magnetization Reorientation for Magnetoelectric Memory Devices Electrical Control of Reversible and Permanent

Magnetization Reorientation for Magnetoelectric Memory Devices. *Appl. Phys. Lett.* **2011**, *98*, 262504.

(57) Kingon, A. Memories Are Made of …. *Nature* **1999**, *401*, 658–659.

(58) Zhang, Y.; Gao, G.; Chan, H. L. W.; Dai, J.; Wang, Y.; Hao, J. Piezo-phototronic Effect-induced Dual-mode Light and Ultrasound Emissions from ZnS:Mn/PMN-PT Thin-film Structures. *Adv. Mater.* **2012**, *24*, 1729–1735.

(59) Ding, F.; Ji, H.; Chen, Y.; Herklotz, A.; Dörr, K.; Mei, Y.; Rastelli, A.; Schmidt, O. G. Stretchable Graphene: a Close Look at Fundamental Parameters Through Biaxial Straining. *Nano Lett.* **2010**, *10*, 3453–3458.

(60) Wong, J.-H.; Wu, B.-R.; Lin, M.-F. Strain Effect on the Electronic Properties of Single Layer and Bilayer Graphene. *J. Phys. Chem. C* **2012**, *116*, 8271–8277.

(61) Mohiuddin, T.; Lombardo, A.; Nair, R.; Bonetti, A.; Savini, G.; Jalil, R.; Bonini, N.; Basko, D.; Galiotis, C.; Marzari, N. *et al.* Uniaxial Strain in Graphene by Raman Spectroscopy: G Peak Splitting, Grüneisen Parameters, and Sample Orientation. *Phys. Rev. B* **2009**, *79*, 205433.

(62) Yu, T.; Ni, Z.; Du, C.; You, Y.; Wang, Y.; Shen, Z. Raman Mapping Investigation of Graphene on Transparent Flexible Substrate: The Strain Effect. *J. Phys. Chem. C* **2008**, *112*, 12602–12605.

(63) Konstantatos, G.; Sargent, E. H. Nanostructured Materials for Photon Detection. *Nat. Nanotechnol.* **2010**, *5*, 391–400.

(64) Wang, X.; Zhi, L.; Mu, K. Transparent , Conductive Graphene Electrodes for Dye-Sensitized Solar Cells. *Nano Lett.* **2008**, *8*, 323–327.

(65) Yin, Z.; Wu, S.; Zhou, X.; Huang, X.; Zhang, Q.; Boey, F.; Zhang, H. Electrochemical Deposition of ZnO Nanorods on Transparent Reduced Graphene Oxide Electrodes for Hybrid Solar Cells. *Small* **2010**, *6*, 307–312.

(66) Pospischil, A.; Humer, M.; Furchi, M. M.; Bachmann, D.; Guider, R.; Fromherz, T.; Mueller, T. CMOS-compatible Graphene Photodetector Covering All Optical Communication Bands. *Nat. Photon.* **2013**, *7*, 892–896.

(67) Wang, X.; Cheng, Z.; Xu, K.; Tsang, H. K.; Xu, J.-B. High-responsivity Graphene/silicon-heterostructure Waveguide Photodetectors. *Nat. Photon.* **2013**, *7*, 888–891.

(68) Gan, X.; Shiue, R.-J.; Gao, Y.; Meric, I.; Heinz, T. F.; Shepard, K.; Hone, J.; Assefa, S.; Englund, D. Chip-integrated Ultrafast Graphene Photodetector with High Responsivity. *Nat. Photon.* **2013**, *7*, 883–887.

(69) Chen, C.-C.; Chang, C.-C.; Li, Z.; Levi, A. F. J.; Cronin, S. B. Gate Tunable Graphene-silicon Ohmic/Schottky Contacts. *Appl. Phys. Lett.* **2012**, *101*, 223113.

(70) Wu, X.; Sprinkle, M.; Li, X.; Ming, F.; Berger, C.; de Heer, W. Epitaxial-Graphene/Graphene-Oxide Junction: An Essential Step Towards Epitaxial Graphene Electronics. *Phys. Rev. Lett.* **2008**, *101*, 026801.

(71) Ye, Y.; Dai, L. Graphene-based Schottky Junction Solar Cells. *J. Mater. Chem.* **2012**, *22*, 24224–24229.

(72) An, X.; Liu, F.; Jung, Y. J.; Kar, S. Tunable Graphene-silicon Heterojunctions for Ultrasensitive Photodetection. *Nano Lett.* **2013**, *13*, 909–916.

(73) Jin, W.; Ye, Y.; Gan, L.; Yu, B.; Wu, P.; Dai, Y.; Meng, H.; Guo, X.; Dai, L. Self-powered High Performance Photodetectors Based on CdSe Nanobelt/graphene Schottky Junctions. *J. Mater. Chem.* **2012**, *22*, 2863–2867.

(74) Ye, Y.; Gan, L.; Dai, L.; Meng, H.; Wei, F.; Dai, Y.; Shi, Z.; Yu, B.; Guo, X.; Qin, G. Multicolor Graphene Nanoribbon/semiconductor Nanowire Heterojunction Light-emitting Diodes. *J. Mater. Chem.* **2011**, *21*, 11760–11763.

(75) Pang, S.; Hernandez, Y.; Feng, X.; Müllen, K. Graphene as Transparent Electrode Material for Organic Electronics. *Adv. Mater.* **2011**, *23*, 2779–2795.

(76) Bonaccorso, F.; Sun, Z.; Hasan, T.; Ferrari, A. C. Graphene Photonics and Optoelectronics. *Nat. Photon.* **2010**, *4*, 611–622.

(77) Kim, R.-H.; Bae, M.-H.; Kim, D. G.; Cheng, H.; Kim, B. H.; Kim, D.-H.; Li, M.; Wu, J.; Du, F.; Kim, H.-S. *et al.* Stretchable, Transparent Graphene Interconnects for Arrays of Microscale Inorganic Light Emitting Diodes on Rubber Substrates. *Nano Lett.* **2011**, *11*, 3881–3886.

(78) Won, R. Photovoltaics: Graphene–silicon Solar Cells. *Nat. Photon.* **2010**, *4*, 411.

(79) Li, Z.; Zhu, H.; Xie, D.; Wang, K.; Cao, A.; Wei, J.; Li, X.; Fan, L.; Wu, D. Flame Synthesis of Few-layered Graphene/graphite Films. *Chem. Commun.* **2011**, *47*, 3520–3522.

(80) Li, X.; Xie, D.; Park, H.; Zhu, M.; Zeng, T. H.; Wang, K.; Wei, J.; Wu, D.; Kong, J.; Zhu, H. Ion Doping of Graphene for High-efficiency Heterojunction Solar Cells. *Nanoscale* **2013**, *5*, 1945–1948.

(81) Green, M. A.; Emery, K.; Hishikawa, Y.; Warta, W.; Dunlop, E. D. Solar Cell Efficiency Tables (version 43). *Prog. Photovolt: Res. Appl.* **2013**, 827–837.

(82) Feng, T.; Xie, D.; Lin, Y.; Zang, Y.; Ren, T.; Song, R.; Zhao, H.; Tian, H.; Li, X.; Zhu, H. *et al.* Graphene Based Schottky Junction Solar Cells on Patterned Silicon-pillar-array Substrate. *Appl. Phys. Lett.* **2011**, *99*, 233505.

(83) Shi, Y.; Kim, K. K.; Reina, A.; Hofmann, M.; Li, L.-J.; Kong, J. Work Function Engineering of Graphene Electrode via Chemical Doping. *ACS Nano* **2010**, *4*, 2689–2694.

(84) Fan, G.; Zhu, H.; Wang, K.; Wei, J.; Li, X.; Shu, Q.; Guo, N.; Wu, D. Graphene/silicon Nanowire Schottky Junction for Enhanced Light Harvesting. *ACS Appl. Mater. Interfaces* **2011**, *3*, 721–725.

(85) Li, X.; Fan, L.; Li, Z.; Wang, K.; Zhong, M.; Wei, J.; Wu, D.; Zhu, H. Boron Doping of Graphene for Graphene-Silicon P-n Junction Solar Cells. *Adv. Energy Mater.* **2012**, *2*, 425–429.

(86) Miao, X.; Tongay, S.; Petterson, M. K.; Berke, K.; Rinzler, A. G.; Appleton, B. R.; Hebard, A. F. High Efficiency Graphene Solar Cells by Chemical Doping. *Nano Lett.* **2012**, *12*, 2745–2750.

(87) Li, X.; Xie, D.; Park, H.; Zeng, T. H.; Wang, K.; Wei, J.; Zhong, M.; Wu, D.; Kong, J.; Zhu, H. Anomalous Behaviors of Graphene Transparent Conductors in Graphene-Silicon Heterojunction Solar Cells. *Adv. Energy Mater.* **2013**, *3*, 1029–1034.

(88) Lin, Y.; Li, X.; Xie, D.; Feng, T.; Chen, Y.; Song, R.; Tian, H.; Ren, T.; Zhong, M.; Wang, K. *et al.* Graphene/semiconductor Heterojunction Solar Cells with Modulated Antireflection and Graphene Work Function. *Energy Environ. Sci.* **2013**, *6*, 108–115.

(89) Shi, E.; Li, H.; Yang, L.; Zhang, L.; Li, Z.; Li, P.; Shang, Y.; Wu, S.; Li, X.; Wei, J. *et al.* Colloidal Antireflection Coating Improves Graphene-silicon Solar Cells. *Nano Lett.* **2013**, *13*, 1776–1781.

(90) Green, M. A.; Emery, K.; Hishikawa, Y.; Warta, W.; Dunlop, E. D. Solar Cell Efficiency Tables (Version 39). *Prog. Photovolt: Res. Appl.* **2012**, *20*, 12–20.

(91) Wei, X. H.; Huang, W.; Yang, Z. B.; Hao, J. H. Interfacial and Rectifying Characteristic of Epitaxial SrTiO3-δ/GaAs P–n Junctions. *Scripta Mater.* **2011**, *65*, 323–326.

(92) Huang, W.; Wu, Z. P.; Hao, J. H. Electrical Properties of Ferroelectric BaTiO[sub 3] Thin Film on SrTiO[sub 3] Buffered GaAs by Laser Molecular Beam Epitaxy. *Appl. Phys. Lett.* **2009**, *94*, 032905.

(93) Yang, Z.; Huang, W.; Hao, J. Determination of Band Alignment of Pulsed-laser-deposited Perovskite titanate/III-V Semiconductor Heterostructure Using X-ray and Ultraviolet Photoelectron Spectroscopy. *Appl. Phys. Lett.* **2013**, *103*, 031919.

(94) Jie, W.; Zheng, F.; Hao, J. Graphene/gallium Arsenide-based Schottky Junction Solar Cells. *Appl. Phys. Lett.* **2013**, *103*, 233111.

(95) Li, X.; Zhang, S.; Wang, P.; Zhong, H. High Performance Solar Cells Based on Graphene / GaAs Heterostructures. 1–22.

(96) Ye, Y.; Gan, L.; Dai, L.; Dai, Y.; Guo, X.; Meng, H.; Yu, B.; Shi, Z.; Shang, K.; Qin, G. A Simple and Scalable Graphene Patterning Method and Its Application in CdSe Nanobelt/graphene Schottky Junction Solar Cells. *Nanoscale* **2011**, *3*, 1477–1481.

(97) Ye, Y.; Dai, Y.; Dai, L.; Shi, Z.; Liu, N.; Wang, F.; Fu, L.; Peng, R.; Wen, X.; Chen, Z. *et al.* High-performance Single CdS Nanowire (nanobelt) Schottky Junction Solar Cells with Au/graphene Schottky Electrodes. *ACS Appl. Mater. Interfaces* **2010**, *2*, 3406–3410.

(98) Voevodin, V. G.; Voevodina, O. V.; Bereznaya, S. A.; Korotchenko, Z. V.; Morozov, A. N.; Sarkisov, S. Y.; Fernelius, N. C.; Goldstein, J. T. Large Single Crystals of Gallium Selenide: Growing, Doping by In and Characterization. *Opt. Mater.* **2004**, *26*, 495–499.

(99) Plucinski, L.; Johnson, R.; Kowalski, B.; Kopalko, K.; Orlowski, B.; Kovalyuk, Z.; Lashkarev, G. Electronic Band Structure of GaSe (0001): Angle-resolved Photoemission and Ab Initio Theory. *Phys. Rev. B* **2003**, *68*, 125304.

(100) Lei, S.; Ge, L.; Liu, Z.; Najmaei, S.; Shi, G.; You, G.; Lou, J.; Vajtai, R.; Ajayan, P. M. Synthesis and Photoresponse of Large GaSe Atomic Layers. *Nano Lett.* **2013**, *13*, 2777–2781.

(101) Zhou, Y.; Nie, Y.; Liu, Y.; Yan, K.; Hong, J.; Jin, C.; Zhou, Y.; Yin, J.; Liu, Z.; Peng, H. Epitaxy and Photoresponse of Two-dimensional GaSe Crystals on Flexible Transparent Mica Sheets. *ACS Nano* **2014**, *8*, 1485–1490.

(102) Mahjouri-Samani, M.; Gresback, R.; Tian, M.; Wang, K.; Puretzky, A. A.; Rouleau, C. M.; Eres, G.; Ivanov, I. N.; Xiao, K.; McGuire, M. A. *et al.* Pulsed Laser Deposition of Photoresponsive Two-Dimensional GaSe Nanosheet Networks. *Adv. Funct. Mater.* **2014**, DOI: 10.1002/adfm.201401440.

(103) Zeng, H.; Liu, G.-B.; Dai, J.; Yan, Y.; Zhu, B.; He, R.; Xie, L.; Xu, S.; Chen, X.; Yao, W. *et al.* Optical Signature of Symmetry Variations and Spin-valley Coupling in Atomically Thin Tungsten Dichalcogenides. *Sci. Rep.* **2013**, *3*, 1608.

(104) Malard, L. M.; Alencar, T. V.; Barboza, A. P. M.; Mak, K. F.; de Paula, A. M. Observation of Intense Second Harmonic Generation from MoS2 Atomic Crystals. *Phys. Rev. B* **2013**, *87*, 201401.

(105) Kumar, N.; Najmaei, S.; Cui, Q.; Ceballos, F.; Ajayan, P.; Lou, J.; Zhao, H. Second Harmonic Microscopy of Monolayer MoS2. *Phys. Rev. B* **2013**, *87*, 161403.

(106) Li, Y.; Rao, Y.; Mak, K. F.; You, Y.; Wang, S.; Dean, C. R.; Heinz, T. F. Probing Symmetry Properties of Few-layer MoS2 and h-BN by Optical Second-harmonic Generation. *Nano Lett.* **2013**, *13*, 3329–3333.

(107) Hsu, W.; Zhao, Z.; Li, L.; Chen, C. Second Harmonic Generation from Artificially Stacked Transition Metal Dichalcogenide Twisted Bilayers. *ACS Nano* **2014**, *8*, 2951–2958.

(108) Kim, C.-J.; Brown, L.; Graham, M. W.; Hovden, R.; Havener, R. W.; McEuen, P. L.; Muller, D. A.; Park, J. Stacking Order Dependent Second Harmonic Generation and Topological Defects in h-BN Bilayers. *Nano Lett.* **2013**, *13*, 5660–5665.

(109) Emtsev, K. V.; Bostwick, A.; Horn, K.; Jobst, J.; Kellogg, G. L.; Ley, L.; McChesney, J. L.; Ohta, T.; Reshanov, S. A.; Röhrl, J. *et al.* Towards Wafer-size Graphene Layers by Atmospheric Pressure Graphitization of Silicon Carbide. *Nat. Mater.* **2009**, *8*, 203–207.

(110) Sutter, P. W.; Flege, J.-I.; Sutter, E. A. Epitaxial Graphene on Ruthenium. *Nat. Mater.* **2008**, *7*, 406–411.

(111) Stankovich, S.; Dikin, D. A.; Piner, R. D.; Kohlhaas, K. A.; Kleinhammes, A.; Jia, Y.; Wu, Y.; Nguyen, S. T.; Ruoff, R. S. Synthesis of Graphene-based Nanosheets via Chemical Reduction of Exfoliated Graphite Oxide. *Carbon* **2007**, *45*, 1558–1565.

(112) Wang, H.; Robinson, J. T.; Li, X.; Dai, H. Solvothermal Reduction of Chemically Exfoliated Graphene Sheets. *J. Am. Chem. Soc.* **2009**, *131*, 9910–9911.

(113) Li, X.; Zhang, G.; Bai, X.; Sun, X.; Wang, X.; Wang, E.; Dai, H. Highly Conducting Graphene Sheets and Langmuir-Blodgett Films. *Nat. Nanotechnol.* **2008**, *3*, 538–542.

(114) Novoselov, K. S.; Geim, A. K.; Morozov, S. V.; Jiang, D.; Zhang, Y.; Dubonos, S. V.; Grigorieva, I. V.; Firsov, A. A. Electric Field Effect in Atomically Thin Carbon Films. *Science* **2004**, *306*, 666–669.

(115) Kim, K. S.; Zhao, Y.; Jang, H.; Lee, S. Y.; Kim, J. M.; Kim, K. S.; Ahn, J.-H.; Kim, P.; Choi, J.-Y.; Hong, B. H. Large-scale Pattern Growth of Graphene Films for Stretchable Transparent Electrodes. *Nature* **2009**, *457*, 706–710.

(116) Li, X.; Cai, W.; An, J.; Kim, S.; Nah, J.; Yang, D.; Piner, R.; Velamakanni, A.; Jung, I.; Tutuc, E. *et al.* Large-area Synthesis of High-quality and Uniform Graphene Films on Copper Foils. *Science* **2009**, *324*, 1312–1314.

(117) Bae, S.; Kim, H.; Lee, Y.; Xu, X.; Park, J.-S.; Zheng, Y.; Balakrishnan, J.; Lei, T.; Kim, H. R.; Song, Y. I. *et al.* Roll-to-roll Production of 30-inch Graphene Films for Transparent Electrodes. *Nat. Nanotechnol.* **2010**, *5*, 574–578.

(118) Gao, L.; Ren, W.; Xu, H.; Jin, L.; Wang, Z.; Ma, T.; Ma, L.-P.; Zhang, Z.; Fu, Q.; Peng, L.-M. *et al.* Repeated Growth and Bubbling Transfer of Graphene with Millimetre-size Single-crystal Grains Using Platinum. *Nat. Commun.* **2012**, *3*, 699.

(119) Raghavan, S.; Stolichnov, I.; Setter, N.; Heron, J.; Tosun, M.; Kis, A. Long-term Retention in Organic Ferroelectric-graphene Memories. *Appl. Phys. Lett.* **2012**, *100*, 023507.

(120) Baltazar, J.; Sojoudi, H.; Paniagua, S. A.; Kowalik, J.; Marder, S. R.; Tolbert, L. M.; Graham, S.; Henderson, C. L. Facile Formation of Graphene P–N Junctions Using Self-Assembled Monolayers. *J. Phys. Chem. C* **2012**, *116*, 19095–19103.

(121) Hwang, H.; Joo, P.; Kang, M.; Ahn, G.; Han, J.; Kim, B.-S.; Cho, H. H. Highly Tunable Charge Transport in Layer-by-Layer Assembled Graphene Transistors. *ACS Nano* **2012**, *6*, 2432–2440.

(122) Baeumer, C.; Rogers, S.; Xu, R.; Martin, L.; Shim, M. Tunable Carrier Type and Density in Graphene/PbZr0.2Ti0.8O3 Hybrid Structures Through Ferroelectric Switching. *Nano Lett.* **2013**, *13*, 1693–1698.

(123) Ni, G.; Zheng, Y.; Bae, S.; Tan, C.; Kahya, O.; Wu, J.; Hong, B. H.; Yao, K.; Ozyilmaz, B. Graphene–Ferroelectric Hybrid Structure for Flexible Transparent Electrodes. *ACS Nano* **2012**, *6*, 3935–3942.

(124) Bae, S.-H.; Kahya, O.; Sharma, B. K.; Kwon, J.; Cho, H. J.; Ozyilmaz, B.; Ahn, J.-H. Graphene-P(VDF-TrFE) Multilayer Film for Flexible Applications. *ACS Nano* **2013**, *7*, 3130–3138.

(125) Liu, Z.; Li, J.; Sun, Z.-H.; Tai, G.; Lau, S.-P.; Yan, F. The Application of Highly Doped Single-layer Graphene as the Top Electrodes of Semitransparent Organic Solar Cells. *ACS Nano* **2012**, *6*, 810–818.

(126) Kasry, A.; Kuroda, M. A.; Martyna, G. J.; Tulevski, G. S.; Bol, A. A. Chemical Doping of Large-area Stacked Graphene Films for Use as Transparent, Conducting Electrodes. *ACS Nano* **2010**, *4*, 3839–3844.

(127) Gu, F.; Shin, H.; Biswas, C.; Han, G. H.; Kim, E. S.; Chae, S. J. Layer-by-Layer Doping of Few-Layer Graphene Film. *ACS Nano* **2010**, *4*, 4595–4600.

(128) Yan, C.; Kim, K.-S.; Lee, S.-K.; Bae, S.-H.; Hong, B. H.; Kim, J.-H.; Lee, H.-J.; Ahn, J.-H. Mechanical and Environmental Stability of Polymer Thin-film-coated Graphene. *ACS Nano* **2012**, *6*, 2096–2103.

(129) Chandra, B.; Afzali, A.; Khare, N.; El-Ashry, M. M.; Tulevski, G. S. Stable Charge-Transfer Doping of Transparent Single-Walled Carbon Nanotube Films. *Chem. Mater.* **2010**, *22*, 5179–5183.

(130) Hsieh, C.-Y.; Chen, Y.-T.; Tan, W.-J.; Chen, Y.-F.; Shih, W. Y.; Shih, W.-H. Graphene-lead Zirconate Titanate Optothermal Field Effect Transistors. *Appl. Phys. Lett.* **2012**, *100*, 113507.

(131) Fu, X.-W.; Liao, Z.-M.; Zhou, J.-X.; Zhou, Y.-B.; Wu, H.-C.; Zhang, R.; Jing, G.; Xu, J.; Wu, X.; Guo, W. *et al.* Strain Dependent Resistance in Chemical Vapor Deposition Grown Graphene. *Appl. Phys. Lett.* **2011**, *99*, 213107.

(132) Frank, O.; Tsoukleri, G.; Parthenios, J.; Papagelis, K.; Riaz, I.; Jalil, R.; Novoselov, K. S.; Galiotis, C. Compression Behavior of Single-layer Graphenes. *ACS Nano* **2010**, *4*, 3131–3138.

(133) Ni, Z. H.; Yu, T.; Lu, Y. H.; Wang, Y. Y.; Feng, Y. P.; Shen, Z. X. Uniaxial Strain on Graphene : Raman Spectroscopy Study and Band-Gap Opening. *ACS Nano* **2008**, *2*, 2301–2305.

(134) Lee, Y.-H.; Kim, Y.-J. Electrical and Lattice Vibrational Behaviors of Graphene Devices on Flexible Substrate Under Small Mechanical Strain. *Appl. Phys. Lett.* **2012**, *101*, 083102.

(135) Zabel, J.; Nair, R. R.; Ott, A.; Georgiou, T.; Geim, A. K.; Novoselov, K. S.; Casiraghi, C. Raman Spectroscopy of Graphene and Bilayer Under Biaxial Strain: Bubbles and Balloons. *Nano Lett.* **2012**, *12*, 617–621.

(136) Lee, J.-U.; Yoon, D.; Cheong, H. Estimation of Young's Modulus of Graphene by Raman Spectroscopy. *Nano Lett.* **2012**, *12*, 4444–4448.

(137) Park, S.; Shrout, T. R. Ultrahigh Strain and Piezoelectric Behavior in Relaxor Based Ferroelectric Single Crystals. *J. Appl. Phys.* **1997**, *82*, 1804–1811.

(138) Kutnjak, Z.; Petzelt, J.; Blinc, R. The Giant Electromechanical Response in Ferroelectric Relaxors as a Critical Phenomenon. *Nature* **2006**, *441*, 956–959.

(139) Zhang, Y.; Gao, G.; Chan, H. L. W.; Dai, J.; Wang, Y.; Hao, J. Piezo-phototronic Effect-induced Dual-mode Light and Ultrasound Emissions from ZnS:Mn/PMN-PT Thin-film Structures. *Adv. Mater.* **2012**, *24*, 1729–1735.

(140) Hui, Y. Y.; Liu, X.; Jie, W.; Chan, N. Y.; Hao, J.; Hsu, Y.-T.; Li, L.-J.; Guo, W.; Lau, S. P. Exceptional Tunability of Band Energy in a Compressively Strained Trilayer MoS2 Sheet. *ACS Nano* **2013**, *7*, 7126–7131.

(141) Jie, W.; Hui, Y. Y.; Chan, N. Y.; Zhang, Y.; Lau, S. P.; Hao, J. Ferroelectric Polarization Effects on the Transport Properties Of. *J. Phys. Chem. C* **2013**, *117*, 13747–13752.

(142) Jie, W.; Hui, Y. Y.; Zhang, Y.; Lau, S. P.; Hao, J. Effects of Controllable Biaxial Strain on the Raman Spectra of Monolayer Graphene Prepared by Chemical Vapor Deposition. *Appl. Phys. Lett.* **2013**, *102*, 223112.

(143) Ferrari, A. C.; Meyer, J. C.; Scardaci, V.; Casiraghi, C.; Lazzeri, M.; Mauri, F.; Piscanec, S.; Jiang, D.; Novoselov, K. S.; Roth, S. *et al.* Raman Spectrum of Graphene and Graphene Layers. *Phys. Rev. Lett.* **2006**, *97*, 187401.

(144) Romero, H.; Shen, N.; Joshi, P. N-type Behavior of Graphene Supported on Si/SiO2 Substrates. *ACS Nano* **2008**, *2*, 2037–2044.

(145) Kim, W.; Javey, A.; Vermesh, O.; Wang, Q.; Li, Y.; Dai, H. Hysteresis Caused by Water Molecules in Carbon Nanotube Field-effect Transistors. *Nano lett.* **2003**, *3*, 193–198.

(146) Xu, H.; Chen, Y.; Zhang, J.; Zhang, H. Investigating the Mechanism of Hysteresis Effect in Graphene Electrical Field Device Fabricated on SiO_2 Substrates Using Raman Spectroscopy. *Small* **2012**, *8*, 2833–2840.

(147) Bolotin, K.; Sikes, K.; Hone, J.; Stormer, H.; Kim, P. Temperature-dependent Transport in Suspended Graphene. *Phys. Rev. Lett.* **2008**, *101*, 096802.

(148) Castro, E.; Ochoa, H.; Katsnelson, M. Limits on Charge Carrier Mobility in Suspended Graphene Due to Flexural Phonons. *Phys. Rev. Lett.* **2010**, *105*, 266601.

(149) Ni, G.-X.; Zheng, Y.; Bae, S.; Kim, H. R.; Pachoud, A.; Kim, Y. S.; Tan, C.-L.; Im, D.; Ahn, J.-H.; Hong, B. H. *et al.* Quasi-periodic Nanoripples in Graphene Grown by Chemical Vapor Deposition and Its Impact on Charge Transport. *ACS Nano* **2012**, *6*, 1158–1164.

(150) Chen, J.-H.; Jang, C.; Xiao, S.; Ishigami, M.; Fuhrer, M. S. Intrinsic and Extrinsic Performance Limits of Graphene Devices on SiO2. *Nat. Nanotechnol.* **2008**, *3*, 206–209.

(151) Xu, W.; Peeters, F.; Lu, T. Dependence of Resistivity on Electron Density and Temperature in Graphene. *Phys. Rev. B* **2009**, *79*, 073403.

(152) Schiefele, J.; Sols, F.; Guinea, F. Temperature Dependence of the Conductivity of Graphene on Boron Nitride. *Phys. Rev. B* **2012**, *85*, 195420.

(153) Fan, X.; Nouchi, R.; Tanigaki, K. Effect of Charge Puddles and Ripples on the Chemical Reactivity of Single Layer Graphene Supported by SiO2/Si Substrate. *J. Phys. Chem. C* **2011**, *115*, 12960–12964.

(154) Chen, J.-H.; Jang, C.; Adam, S.; Fuhrer, M. S.; Williams, E. D.; Ishigami, M. Charged-impurity Scattering in Graphene. *Nat. Phys.* **2008**, *34*, 377–381.

(155) Skákalová, V.; Kaiser, A.; Yoo, J.; Obergfell, D.; Roth, S. Correlation Between Resistance Fluctuations and Temperature Dependence of Conductivity in Graphene. *Phys. Rev. B* **2009**, *80*, 153404.

(156) Price, A. S.; Hornett, S. M.; Shytov, A. V.; Hendry, E.; Horsell, D. W. Nonlinear Resistivity and Heat Dissipation in Monolayer Graphene. *Phys. Rev. B* **2012**, *85*, 161411(R).

(157) Zheng, R.; Wang, Y.; Wang, J.; Wong, K.; Chan, H.; Choy, C.; Luo, H. Tuning the Electrical Properties of La0.75Ca0.25MnO3 Thin Films by Ferroelectric Polarization, Ferroelectric-field Effect, and Converse Piezoelectric Effect. *Phys. Rev. B* **2006**, *74*, 094427.

(158) E. J. Guo, J. Gao, H. B. L. Coaction of Strain and Polarization Effects on Tuning the Photoinduced Resistance Changes in La0.9Sr0.1MnO3 Films. *Europhys. Lett.* **2011**, *95*, 47006.

(159) Yang, Y.; Luo, Z. L.; Huang, H.; Gao, Y.; Bao, J.; Li, X. G.; Zhang, S.; Zhao, Y. G.; Chen, X.; Pan, G. *et al.* Electric-field-control of Resistance and Magnetization Switching in Multiferroic Zn0.4Fe2.6O4/0.7Pb(Mg2/3Nb1/3)O3–0.3PbTiO3 Epitaxial Heterostructures. *Appl. Phys. Lett.* **2011**, *98*, 153509.

(160) Lee, J. E.; Ahn, G.; Shim, J.; Lee, Y. S.; Ryu, S. Optical Separation of Mechanical Strain from Charge Doping in Graphene. *Nat. commun.* **2012**, *3*, 1024.

(161) Kotakoski, J.; Meyer, J. Mechanical Properties of Polycrystalline Graphene Based on a Realistic Atomistic Model. *Phys. Rev. B* **2012**, *85*, 195447.

(162) Hao, F.; Fang, D. Mechanical Deformation and Fracture Mode of Polycrystalline Graphene: Atomistic Simulations. *Phys. Lett. A* **2012**, *376*, 1942–1947.

(163) Malard, L. M.; Pimenta, M. a.; Dresselhaus, G.; Dresselhaus, M. S. Raman Spectroscopy in Graphene. *Phy. Rep.* **2009**, *473*, 51–87.

(164) Bissett, M. a; Izumida, W.; Saito, R.; Ago, H. Effect of Domain Boundaries on the Raman Spectra of Mechanically Strained Graphene. *ACS Nano* **2012**, *6*, 10229–10238.

(165) Lee, C.; Wei, X.; Kysar, J. W.; Hone, J. Measurement of the Elastic Properties and Intrinsic Strength of Monolayer Graphene. *Science* **2008**, *321*, 385–588.

(166) Yoon, D.; Son, Y.; Cheong, H. Negative Thermal Expansion Coefficient of Graphene Measured by Raman Spectroscopy. *Nano Lett.* **2011**, *11*, 3227–3231.

(167) Wang, Y.; Tong, S. W.; Xu, X. F.; Ozyilmaz, B.; Loh, K. P. Interface Engineering of Layer-by-layer Stacked Graphene Anodes for High-performance Organic Solar Cells. *Adv. Mater.* **2011**, *23*, 1514–1518.

(168) Gomez De Arco, L.; Zhang, Y.; Schlenker, C. W.; Ryu, K.; Thompson, M. E.; Zhou, C. Continuous, Highly Flexible, and Transparent Graphene Films by Chemical Vapor Deposition for Organic Photovoltaics. *ACS Nano* **2010**, *4*, 2865–2873.

(169) Song, J. C. W.; Rudner, M. S.; Marcus, C. M.; Levitov, L. S. Hot Carrier Transport and Photocurrent Response in Graphene. *Nano Lett.* **2011**, *11*, 4688–4692.

(170) Freitag, M.; Low, T.; Xia, F.; Avouris, P. Photoconductivity of Biased Graphene. *Nat. Photon.* **2012**, *7*, 53–59.

(171) Gabor, N. M.; Song, J. C. W.; Ma, Q.; Nair, N. L.; Taychatanapat, T.; Watanabe, K.; Taniguchi, T.; Levitov, L. S.; Jarillo-Herrero, P. Hot Carrier-assisted Intrinsic Photoresponse in Graphene. *Science* **2011**, *334*, 648–652.

(172) Guo, C. X.; Guai, G. H.; Li, C. M. Graphene Based Materials: Enhancing Solar Energy Harvesting. *Adv. Energy Mater.* **2011**, *1*, 448–452.

(173) Huang, X.; Zeng, Z.; Fan, Z.; Liu, J.; Zhang, H. Graphene-based Electrodes. *Adv. Mater.* **2012**, *24*, 5979–6004.

(174) Search, H.; Journals, C.; Contact, A.; Iopscience, M.; Address, I. P. On the Richardson Constant of Intimate metal-GaAs Schottky Barriers. *Semicond. Sci. Technol* **1992**, *7*, 218–221.

(175) Liu, Z.; Li, J.; Yan, F. Package-Free Flexible Organic Solar Cells with Graphene Top Electrodes. *Adv. Mater.* **2013**, 10.1002/adma.201205337.

(176) Li, X.; Lin, M.-W.; Puretzky, A. A.; Idrobo, J. C.; Ma, C.; Chi, M.; Yoon, M.; Rouleau, C. M.; Kravchenko, I. I.; Geohegan, D. B. *et al.* Controlled Vapor Phase Growth of Single Crystalline, Two-Dimensional GaSe Crystals with High Photoresponse. *Sci. Rep.* **2014**, *4*, 5497.

(177) Reeve, J. E.; Corbett, A. D.; Boczarow, I.; Kaluza, W.; Barford, W.; Bayley, H.; Wilson, T.; Anderson, H. L. Porphyrins for Probing Electrical Potential Across Lipid Bilayer Membranes by Second Harmonic Generation. *Angew. Chem. Int. Ed.* **2013**, *52*, 9044–9048.

(178) Li, Z.; Wu, W.; Li, Q.; Yu, G.; Xiao, L.; Liu, Y.; Ye, C.; Qin, J.; Li, Z. High-generation Second-order Nonlinear Optical (NLO) Dendrimers: Convenient Synthesis by Click Chemistry and the Increasing Trend of NLO Effects. *Angew. Chem. Int. Ed.* **2010**, *49*, 2763–2767.

(179) Yu, J.; Cui, Y.; Wu, C.; Yang, Y.; Wang, Z.; O'Keeffe, M.; Chen, B.; Qian, G. Second-order Nonlinear Optical Activity Induced by Ordered Dipolar Chromophores Confined in the Pores of an Anionic Metal-organic Framework. *Angew. Chem. Int. Ed.* **2012**, *51*, 10542–10545.

(180) Jie, W.; Chen, X.; Li, D.; Xie, L.; Hui, Y. Y.; Lau, S. P.; Cui, X.; Hao, J. Layer-dependent Nonlinear Optical Properties and Stability of Non-centrosymmetric Modification in Few-layer GaSe Sheets. *Angew. Chem. Int. Ed.* **2015**, *54*, 1185–1189.

(181) Heflin, J. R.; Figura, C.; Marciu, D.; Liu, Y.; Claus, R. O. Thickness Dependence of Second-harmonic Generation in Thin Films Fabricated from Ionically Self-assembled Monolayers. *Appl. Phys. Lett.* **1999**, *74*, 495.

(182) Heflin, J. R.; Guzy, M. T.; Neyman, P. J.; Gaskins, K. J.; Brands, C.; Wang, Z.; Gibson, H. W.; Davis, R. M.; Van Cott, K. E. Efficient, Thermally Stable, Second Order Nonlinear Optical Response in Organic Hybrid Covalent/ionic Self-assembled Films. *Langmuir* **2006**, *22*, 5723–5727.

(183) Amzallag, J.; Benisty, H.; Debrus, S.; May, M.; Eddrief, M.; Bourdon, A.; Chevy, A.; Piccioli, N. Second Harmonic Generation as a Probe of Antiphase Domains in Layered GaSe Thin Films on Si(111) Substrates. *Appl. Phys. Lett.* **1995**, *66*, 982–984.

(184) Bihari, B.; Kumar, J.; Stauf, G. T.; Van Buskirk, P. C.; Hwang, C. S. Investigation of Barium Titanate Thin Films on MgO Substrates by Second-harmonic Generation. *J. Appl. Phys.* **1994**, *76*, 1169.

(185) Singh, N.; Suhre, D.; Balakrishna, V. Far-infrared Conversion Materials: Gallium Selenide for Far-infrared Conversion Applications. *Prog. Cryst. Growth Charact. Mater.* **1998**, *8974*, 47–102.

(186) Segall, M.; Lindan, P.; Probert, M. J.; Pickard, C.; Hasnip, P.; Clark, S. J.; Payne, M. C. First-principles Simulation: Ideas, Illustrations and the CASTEP Code. *J. Phys.: Condens. Matter*. **2002**, *14*, 2717–2744.

(187) Auerhammer, J. M.; Eliel, E. R. Frequency Doubling of Mid-infrared Radiation in Gallium Selenide. *Opt. Lett.* **1996**, *21*, 773–775.

(188) Yin, X.; Ye, Z.; Chenet, D. A.; Ye, Y.; O'Brien, K.; Hone, J. C.; Zhang, X. Edge Nonlinear Optics on a MoS2 Atomic Monolayer. *Science* **2014**, *344*, 488–490.

(189) Zotova, I. B.; Ding, Y. J. Spectral Measurements of Two-photon Absorption Coefficients for CdSe and GaSe Crystals. *Appl. Opt.* **2001**, *40*, 6654–6658.

(190) Allakhverdiev, K. R.; Baykara, T.; Joosten, S.; Günay, E.; Kaya, A. A.; Kulibekov (Gulubayov), A.; Seilmeier, A.; Salaev, E. Y. Anisotropy of Two-photon Absorption in Gallium Selenide at 1064nm. *Opt. Commun.* **2006**, *261*, 60–64.

(191) Zheng, M.-L.; Fujita, K.; Chen, W.-Q.; Duan, X.-M.; Kawata, S. Two-Photon Excited Fluorescence and Second-Harmonic Generation of the DAST Organic Nanocrystals. *J. Phys. Chem. C* **2011**, *115*, 8988–8993.

(192) Butet, J.; Duboisset, J.; Bachelier, G.; Russier-Antoine, I.; Benichou, E.; Jonin, C.; Brevet, P.-F. Optical Second Harmonic Generation of Single Metallic Nanoparticles Embedded in a Homogeneous Medium. *Nano Lett.* **2010**, *10*, 1717–1721.

(193) Zoumi, A.; Yeh, A.; Tromberg, B. J. Imaging Cells and Extracellular Matrix in Vivo by Using Second-harmonic Generation and Two-photon Excited Fluorescence. *Proc. Nati. Acad. Sci. USA* **2002**, *99*, 11014–11019.

(194) Zhu, B.; Chen, X.; Cui, X. Exciton Binding Energy of Monolayer WS2. arXiv:1403.5108.

(195) Fan, Y.; Bauer, M.; Kador, L.; Allakhverdiev, K. R.; Salaev, E. Y. Photoluminescence Frequency Up-conversion in GaSe Single Crystals as Studied by Confocal Microscopy. *J. Appl. Phys.* **2002**, *91*, 1081–1086.

(196) Yu, W. J.; Liu, Y.; Zhou, H.; Yin, A.; Li, Z.; Huang, Y.; Duan, X. Highly Efficient Gate-tunable Photocurrent Generation in Vertical Heterostructures of Layered Materials. *Nat. Nanotechnol.* **2013**, *8*, 4–10.

(197) Britnell, L.; Ribeiro, R. M.; Eckmann, A.; Jalil, R.; Belle, B. D.; Mishchenko, A.; Kim, Y.-J.; Gorbachev, R. V.; Georgiou, T.; Morozov, S. V. *et al.* Strong Light-matter Interactions in Heterostructures of Atomically Thin Films. *Science* **2013**, *340*, 1311–1314.

(198) Georgiou, T.; Jalil, R.; Belle, B. D.; Britnell, L.; Gorbachev, R. V.; Morozov, S. V.; Kim, Y.-J.; Gholinia, A.; Haigh, S. J.; Makarovsky, O. *et al.* Vertical Field-effect Transistor Based on graphene-WS2 Heterostructures for Flexible and Transparent Electronics. *Nat. Nanotechnol.* **2013**, *8*, 100–103.

(199) Britnell, L.; Gorbachev, R. V.; Jalil, R.; Belle, B. D.; Schedin, F.; Mishchenko, A.; Georgiou, T.; Katsnelson, M. I.; Eaves, L.; Morozov, S. V. *et al.* Field-effect Tunneling Transistor Based on Vertical Graphene Heterostructures. *Science* **2012**, *335*, 947–950.

(200) Gorbachev, R. V.; Geim, A. K.; Katsnelson, M. I.; Novoselov, K. S.; Tudorovskiy, T.; Grigorieva, I. V.; MacDonald, A. H.; Morozov, S. V.; Watanabe, K.; Taniguchi, T. *et al.* Strong Coulomb Drag and Broken Symmetry in Double-layer Graphene. *Nat. Phys.* **2012**, *8*, 896–901.

(201) Bouchiat, V. Graphene: Charges Driving Under the Influence. *Nat. Phys.* **2012**, *8*, 862–863.

(202) Sun, H.; Xu, Z.; Gao, C. Multifunctional, Ultra-flyweight, Synergistically Assembled Carbon Aerogels. *Adv. Mater.* **2013**, *25*, 2554–2560.

(203) Ren, W.; Cheng, H. Materials Science: When Two Is Better Than One. *Nature* **2013**, *497*, 448–449.